PFC/RR-87-17

DOE/ET-51013-232
UC20,a,b,f

Electron Velocity-Space Diffusion in a Micro-Unstable ECRH Mirror Plasma

Samuel A. Hokin

September 1987

Plasma Fusion Center
Massachusetts Institute of Technology
Cambridge, Massachusetts 02139 USA

Supported by United States Department of Energy Contract DE-AC02-78ET51013.

Electron Velocity-Space Diffusion in a Micro-Unstable ECRH Mirror Plasma

by

Samuel Arthur Hokin

B.S. University of Wisconsin, 1982

Submitted to the Department of Physics
in partial fulfillment of the requirements for
the Degree of

Doctor of Philosophy

at the
Massachusetts Institute of Technology
September 22, 1987

Signature of Author _____

Department of Physics
September 22, 1987

Certified by _____

Richard S. Post
Thesis Supervisor

Accepted by _____

George F. Koster
Chairman, Departmental Graduate Committee

Electron Velocity-Space Diffusion

in a

Micro-Unstable ECRH Mirror Plasma

by

Samuel Arthur Hokin

Submitted to the Department of Physics on September 22, 1987
in partial fulfillment of the requirements for the degree of
Doctor of Philosophy

Abstract

An experimental study of the velocity-space diffusion of electrons in an electron cyclotron resonance heated (ECRH) mirror plasma, in the presence of micro-unstable whistler rf emission, is presented. It is found that the dominant loss mechanism for hot electrons, with temperatures $T_h \sim 400$ keV, is endloss produced by rf diffusion into the mirror loss cone. In a standard case with 4.5 kW of ECRH power, this loss limits the stored energy to 120 J with an energy confinement time of 40 ms. The energy confinement time associated with collisional scattering is 350 ms in this case. Whistler microinstability rf produces up to 25% of the rf-induced loss. The hot electron temperature is not limited by loss of adiabaticity, but by rf-induced loss of high energy electrons, and decreases with increasing rf power in strong diffusion regimes. Collisional loss is in agreement with standard scattering theory.

No super-adiabatic effects are clearly seen: there is no observed decrease in the heating rate as electrons are heated from 10 keV to 400 keV, no 'warm' electron component with $T_w \ll T_h$ and density comparable to the hot electron density is observed, and a simulation, using an rf Fokker-Planck code, of strong rf-induced endloss observed in micro-stable experiments requires the fully stochastic rf diffusion strength.

Experiments in which the vacuum chamber walls are lined with microwave absorber reveal that single pass absorption is limited to less than 60%, whereas experiments with reflecting walls exhibit up to 90% absorption. Stronger diffusion is seen in the latter, with a hot electron heating rate which is twice that of the absorber experiments. This increase in diffusion can be produced by two distinct aspects of wall-reflected rf: 1) the broader spatial rf profile, which enlarges the resonant region in velocity space, or 2) a reduction in super-adiabatic effects due to randomization of the electron gyrophase. Since no other aspects of super-adiabaticity are observed, the first mechanism appears more likely.

Thesis Supervisor: Richard S. Post

Acknowledgements

This dissertation is the result of four years of research in the Constance experimental group at the MIT Plasma Fusion Center, research which was aided at every step by the help of the other members. I am particularly grateful to my thesis advisors, Dick Post and Donna Smatlak, for encouragement, evaluation of my progress, and excellent suggestions made throughout the course of the work. I have benefited greatly from their experience. I am grateful to the other students in the group: Xing Chen, Rich Garner, Dan Goodman, and Craig Petty, and the technician, Ken Rettman, who have all been continually cheerful and supportive. I also thank Paul Stek for performing the calibration of the scintillator probe, and the members of the Tara tandem mirror staff for the help they have given, especially Don Smith for designing and maintaining the microwave transmitter.

Some of the computational work presented in this dissertation was performed using codes developed by Tom Rognlien and other members of the mirror theory group at Lawrence Livermore National Laboratory. I thank Tom for the help he has given by providing the codes and discussing the work with me.

I must also thank my undergraduate advisor at the University of Wisconsin, Jim Callen, who encouraged me to research a senior thesis on a plasma physics topic and greatly influenced my choice of plasma physics as a field of specialty.

Finally, and most importantly, I thank my wife Carla Shedivy for *bear*ing with me and giving me her full support throughout my years of graduate study.

Contents

List of Figures

Chapter 1

Introduction

This work presents a theoretical and experimental analysis of the velocity-space diffusion of electrons in an electron cyclotron resonance heated (ECRH) mirror plasma in which the whistler electron microinstability is present. The focus of the investigation is on the process of rf diffusion: whether it follows the behavior predicted by current theory, and what overall effect it has on the heating and confinement of electrons. In the experiment, Constance B, the electrons may be divided into two components: the cold electrons, which are electrostatically confined and have temperatures $T_c \sim 100$ eV, and the hot electrons, which are magnetically confined and have temperatures $T_h \sim 400$ keV. This work deals primarily with the hot electrons, because they are strongly governed by rf diffusion, absorb most of the rf power, comprise virtually all of the energy in the plasma, and are in a parameter regime which has not been studied extensively in experiments.

It is important to point out that the hot electrons are strongly rf diffused, even though the electric field strength is low ($\mathcal{E} < 100$ V/cm). This is because the low plasma density ($n_e \sim 4 \times 10^{11}$ cm^{-3}) and the high hot electron temperature make collisional diffusion very weak, with the result that velocity-space currents due to rf can be over an order of magnitude larger than collisional currents.

The issue of velocity-space diffusion, and that of ECRH heating in general, has been studied for many years. The most direct predecessor of this study is the work carried out by Mike Mauel (1982, 1984) on the Constance 2 experiment (an earlier device in the Constance program at MIT). He found that a pulsed ECRH mirror plasma, which

had much lower electron temperatures and much higher electric field strengths than Constance B, obeyed the quasilinear theory of ECRH (Bernstein and Baxter, 1981) and was therefore amenable to a Fokker-Planck description. The parameter regime of this experiment prevented him from addressing the important issues of super-adiabaticity (the phenomenon in which electrons become phase-locked with the rf waves and cease to undergo strong diffusion), relativistic effects, and the behavior of an ECH plasma in steady-state.

An experiment which had parameters more closely resembling Constance B was the STM device at TRW (Boehmer *et al.*, 1985). This was a symmetric tandem mirror which ran in steady-state, producing hot electrons at the second harmonic resonance with power levels of around 1 kW. The researchers made lifetime measurements of the hot electrons using modulated rf, and found that the electrons had a 'nonclassical' loss component due to the rf. This loss, which they inferred from indirect measurements, was directly measured by Mauel in his experiments. It is due to the rf-induced diffusion of electrons across the loss cone boundary in velocity space, and is a symptom of strong rf diffusion. It was first noted theoretically by Lichtenberg and Melin (1973).

The subject of strong rf diffusion is not limited to mirror devices. An important body of research was carried out in the EBT program at Oak Ridge National Laboratory (Batchelor *et al.*, 1987), where a bumpy torus with 12 toroidally-linked mirror cells produced hot electron rings using second harmonic resonance. This device doesn't have a loss cone like a mirror, but does have a region in velocity space where poor electron drifts lead to rapid radial loss. In fact, the rf diffusion of electrons into this 'direct' loss region has been identified as the dominant mechanism for particle loss in this device.

It is clear that rf diffusion of electrons in velocity space can have drastic consequences for confinement. As ECRH remains a very attractive heating scheme, and is being employed in an increasing number of tokamak facilities as well as mirrors and other devices, its understanding is of the utmost importance. This work presents a series of detailed measurements aimed at investigating the fundamental aspects of ECRH in the strong rf regime: the question of super-adiabaticity, the validity of the Fokker-Planck

description, the way in which rf diffusion determines the steady-state temperature and stored energy, and the role of microinstability, which is inherent to any strongly rf-driven distribution.

The work presented here differs from previous work in a number of respects. Most importantly, a much more extensive set of experiments has been performed, with a larger set of diagnostics. A quantitative direct measurement of hot electron endloss, made with a multi-channel scintillator probe, is presented for the first time. This allows the measurement of electron confinement in the steady-state phase, without having to resort to the indirect techniques, such as modulated rf, that have been used in previous studies. The midplane x-ray spectrum has been measured from 1 keV to 1.5 MeV with the aid of three different detectors, and the axial variation of the hard x-ray spectrum (0.1–1.5 MeV) has been measured, giving a full characterization of the hot electron distribution function. Experiments in which the vacuum chamber walls were lined with microwave absorber have been used to study the effect of reducing wall-reflected rf. The effect of microinstability rf emission, which is inherent to strongly rf-driven electron distributions and has been neglected in most previous research, has been investigated, and a series of experiments in which the microinstability rf was removed were conducted to investigate diffusion produced by the applied rf alone.

The focus of the work presented in this dissertation is the diffusion equation governing the hot electron distribution function in an ECRH mirror plasma,

$$\frac{\partial f}{\partial t} = \nabla \cdot \mathsf{D} \cdot \nabla f + S(\mathbf{p}), \tag{1.1}$$

where the diffusion tensor D represents the overall effect of collisions, applied rf, microinstability rf, and any other processes which affect the motion of an energetic electron, and $S(\mathbf{p})$ represents the source function.

This approach ignores hot electron transport across field lines, and is valid because the parallel hot electron confinement time, which is the same as the energy confinement time $\tau_E \sim 40$ ms, is much shorter than the perpendicular confinement time. This is evident in the experiment because the hot electron density has the same hollow radial profile as the

cold electron density which provides the source for the hot electrons. If hot electron radial transport were significant, the hot electron profile would differ from the source; namely, it would 'fill in' and become less hollow. Hot electron radial transport is not expected to be large: classical transport due to collisions occurs on the times scale of seconds, resonant transport (Cohen, 1979) is negligible because the bounce frequency $f_b \sim 100$ MHz is much greater than the drift frequency $f_d \sim 500$ kHz, significant displacement of guiding centers due to rf kicks is not expected, because the electrons undergo many (~ 10) cyclotron periods while passing through resonance, and neoclassical transport is small owing to the weak dependence of drift orbits on electron pitch angle. Furthermore, unstable MHD activity, which could lead to gross transport, is not present.

There is an aspect of Eq. 1.1 in which cross-field transport can play a role: the source function $S(\mathbf{p})$. The source for the hot electrons is the cold electron population, and the orbits of cold electrons are affected by the spatial structure of the ambipolar potential $\phi \sim 200$ V. This potential depends on both ion and cold electron confinement (particle balance, which determines the ambipolar potential, is dominated by cold electrons and ions, since they have confinement times over an order of magnitude smaller than hot electrons). However, once a cold electron is heated to energies much greater than ϕ, it becomes magnetically confined and is governed by parallel confinement.

In this dissertation I address two fundamental questions surrounding velocity-space diffusion:

- What are the important factors governing the diffusion tensor D and the source functon $S(\mathbf{p})$?
- Can the observed heating and confinement of hot electrons be explained with the theory of rf diffusion?

Theory indicates that the important factors for hot electron diffusion are the rf electric field strength, the velocity-space structure of diffusion characteristics, the spatial electric field profile, and super-adiabatic effects. The source is determined largely by the magnetic geometry and the gas fueling rate. The observed heating and confinement of hot electrons

can be understood in terms of these factors, with the additional result that no clear evidence of super-adiabatic effects has been seen.

In the study of hot electron heating and confinement, a number of important subsidiary questions has been investigated:

- What is the dominant loss mechanism?
- What determines the equilibrium stored energy?
- What determines the equilibrium hot electron temperature?
- Are collisional loss processes consistent with theory?
- How does the cavity rf field affect heating?
- What role does micro-instability rf play?
- What can be determined about cold electron heating and confinement, and the role that cold electrons play as the source for the hot electrons?

Endloss produced by rf diffusion is the dominant loss mechanism for hot electrons: in a standard case, the confinement time in the presence of rf is 40 ms, as compared to the measured 350 ms confinement time associated with collisional pitch-angle scattering. Rf-induced loss has an enormous impact on the stored energy that may be attained in the device. Since both heating and rf-induced endloss are manifestations of rf diffusion, they tend to follow one another — the stronger the heating, the stronger the loss. This results in a confinement limit in the device: above a certain power level (around 2 kW), increased rf power merely results in a more rapid attainment of equilibrium at a fixed stored energy.

The equilibrium stored energy is determined by the balance of the hot electron source and endloss. Both the hot electron source and confinement are maximized when the cold electron absorption is strongest: the former because the cold electrons are the source for

the hot electrons, and the latter because the rf-induced endloss of hot electrons is lowered with the lower rf electric field strength in the presence of strong cold absorption.

The equilibrium temperature is more directly determined by the rf electric field strength alone, and therefore is largest in regimes of poor cold electron absorption, when the applied rf field is strongest. However, for high electric field strengths the hot electron temperature becomes limited by rf-induced endloss, and actually *decreases* with increasing rf power at high levels. The experiment provides clear indication that the hot electron temperature is limited by the process of rf diffusion, and not diffusion in the electron magnetic moment produced by loss of adiabaticity as suggested by Uckan (1982).

Collisional loss processes are generally consistent with theory, with the observed collisional decay times being in good agreement with those calculated for pitch-angle scattering.

Experiments using walls lined with microwave absorber to reduce cavity rf levels have an estimated maximum absorbed power fraction of 60%; the corresponding case with reflective walls has an estimated 90% absorption. The increased absorption cannot be simply attributed to cavity rf power, however, because the measured cavity field strength cannot account for 30% of the total power. Rather, the stronger absorption observed in the 'cavity' experiments can be due to either of two possibilities: 1) the broader spatial profile of cavity fields, or 2) reduction of super-adiabatic effects due to cavity fields. Since super-adiabatic effects are not seen in other aspects of the data, it seems more likely that the former is responsible. Some computational modeling supports this assertion.

The micro-unstable whistler rf emission plays two key roles: 1) it can be a large power loss channel, producing rf emission of up to an estimated 20% of incident power, and 2) it can produce a significant portion (up to 25%) of rf-induced hot electron endloss. Furthermore, the microinstability is *inherent* to regimes of strong heating, because strong heating naturally produces an anisotropic rf-driven 'warm' tail on the cold electron distribution which is unstable.

Cold electron absorption exhibits the generic features of a simple slab model but differs in that the spatial deposition is strongly dependent on the mirror ratio at resonance, an effect which is absent in the slab model but is a natural result of cyclotron resonance in a mirror field.

Finally, it must be noted that the understanding of the experiment is qualitative in many cases, because quantitative modeling of the plasma is rendered difficult by the complexity introduced by the presence of micro-unstable rf emission, the quadrupole magnetic field, and the uncertainty in knowing the rf electric field inside the plasma.

The rest of this dissertation consists of four chapters and two appendices. Chapter 2 describes the basic systems in the experiment, the diagnostics, and the magnetic and heating geometry. Chapter 3 presents an overview of rf diffusion theory with special focus on the application to the experimental results. Chapter 4 contains the results of the experimental research, and is the core of the dissertation. Chapter 5 presents a summary of conclusions, remarks concerning the application to other devices, and outstanding questions for further research. Finally, the appendices present the details of the x-ray and hot electron endloss measurements.

Chapter 2

The Constance B Experiment

The Constance B experiment began operation in November, 1983, and produced over 20,000 plasma shots by September, 1987. The experiment is funded by the Applied Plasma Physics Division of the Office of Fusion Energy in the U.S. Department of Energy, with the goal of examining the basic physics issues of quadrupole mirror-confined plasmas. It is located at the MIT Plasma Fusion Center. The principle investigator is Dick Post. The Constance group presently consists of one full-time scientist (Donna Smatlak), one full-time technician (Ken Rettman), and four graduate students (Xing Chen, Dan Goodman, Craig Petty, and myself); Rich Garner completed the first Ph.D. dissertation from the Constance B group in 1986. Additional support has come from the staff of the Tara tandem mirror experiment.

In this chapter I will briefly describe the basic systems required by the experiment, the diagnostics, the data acquisition and analysis system, the means of parameter control, and the magnetic geometry. For a more extensive description of the Constance experiment and results, see the report by Smatlak *et al.* (1986).

2.1 Basic Systems

Constance B (Fig. 2.1) is an R=2 quadrupole mirror. The magnetic field is produced by a single baseball coil which lies outside of the aluminum vacuum chamber. Fig. 2.2 shows the field lines and $|B|$ contours in the $y = 0$ plane as generated by the computer code EFFI (Sackett, 1978) for a model magnet consisting of four circular arcs, as well as

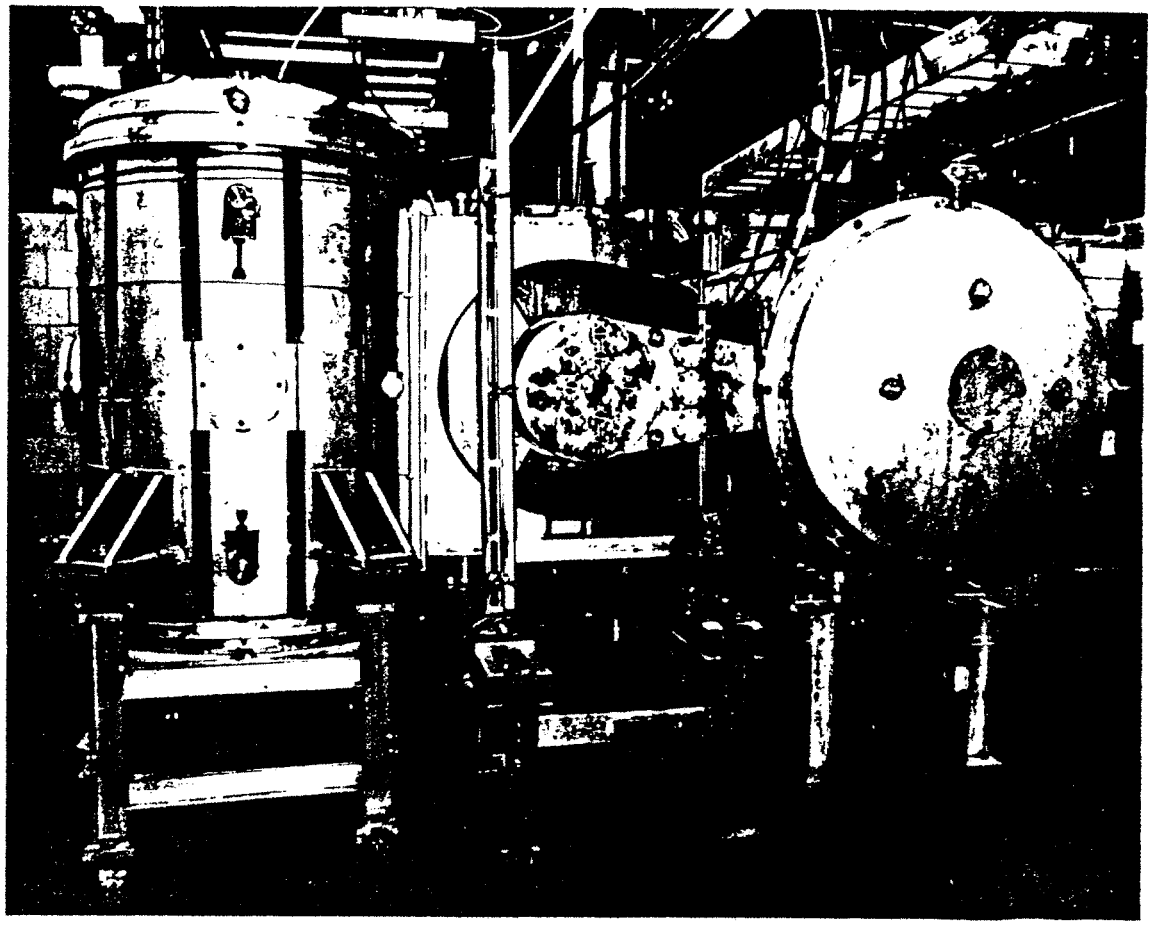

Figure 2.1: The Constance B mirror experiment.

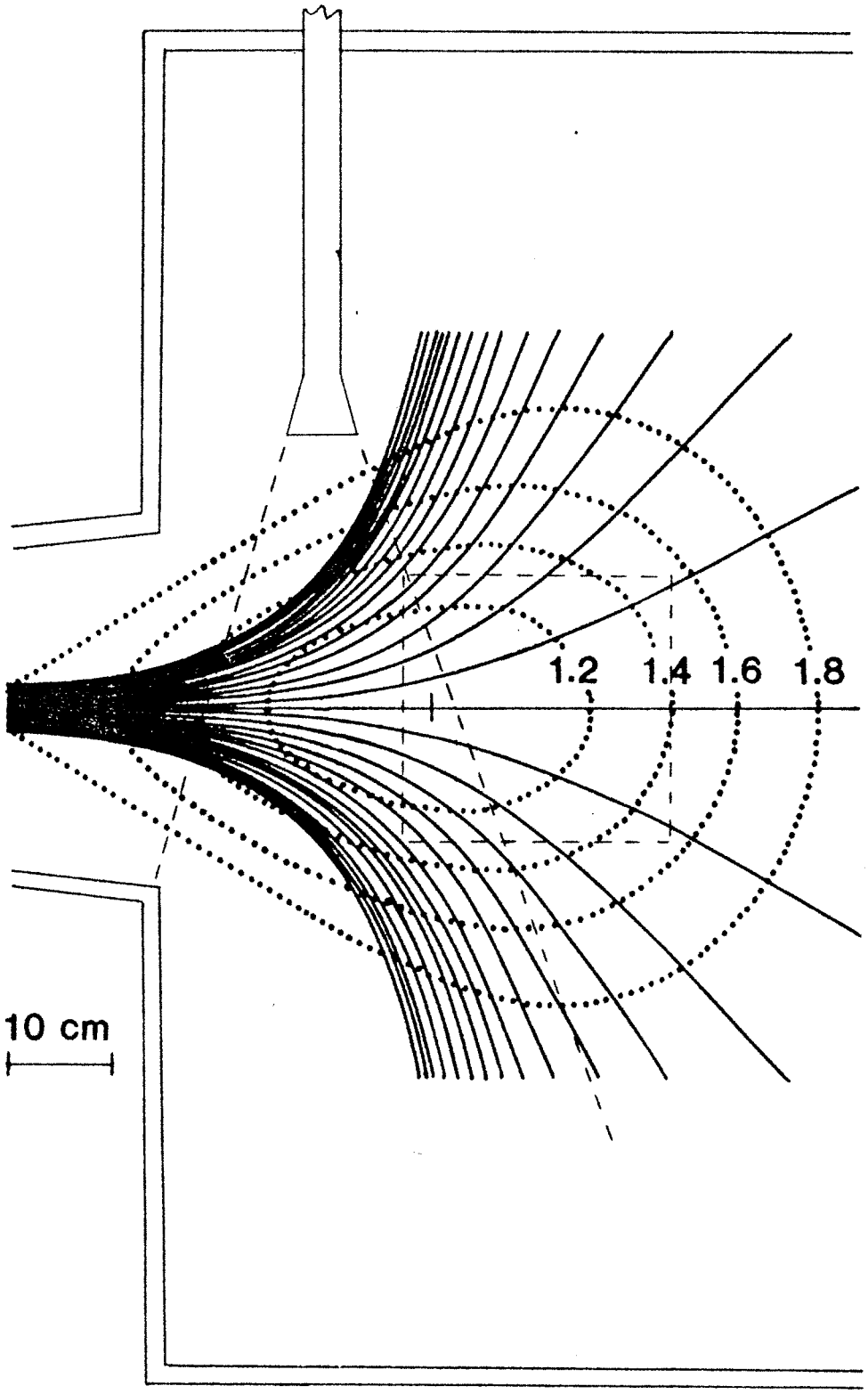

Figure 2.2: Field lines, contours of $|B|/B_0$, and microwave horn. The nonrelativistic resonance is on the egg-shaped surface ($|B|/B_0 = 1.25$) for the standard case $B_0 = 3.0$ kG. The dotted lines indicate the boundary of the first lobe of the rf field pattern; the dotted box is the corresponding 'footprint' at $y = 0$ as viewed from the horn.

the paths of the launched rf rays. The vacuum is maintained by a turbomolecular pump, titanium getters, and a cryogenic LHe pump, and has a base pressure of $1 - 4 \times 10^{-8}$ Torr. The plasma is created by puffing hydrogen gas into the vacuum chamber with a piezo-electric valve, and then breaking it down and heating it with ECRH microwaves produced by a klystron. An electronic process controller is used to control the shot sequence. Two CW klystrons have been available: one at 10.5 GHz with up to 5 kW power, and one at 11.0 GHz with up to 600 W power. All of the data presented in this thesis was obtained using the 10.5 GHz klystron. A shot is usually set to last for two seconds, although shots lasting up to eight seconds have been taken. In addition to the ECRH system, there is an ICRH system (built by Dan Goodman) which produces 50 ms ICRH pulses of up to 10 kW power.

A number of experiments were carried out with microwave absorber attached to the walls of the vacuum chamber in order to reduce the level of cavity rf fields, and are referred to as 'absorber' experiments (experiments without absorber are referred to as 'cavity' experiments). Eccosorb SF-10.5, manufactured by Emerson and Cuming, Inc., was the material used. The absorber was bonded to copper mesh with a compound (Eccosil) manufactured for this purpose and attached to the vacuum chamber by wires. All of the center chamber walls were covered, except for holes to allow diagnostic access. The chamber did still contain rf waveguides and the diamagnetic loop, which are reflective. Measurements indicate that the absorber reduced the cavity field power by approximately a factor of 8. It is worth noting that after a week of pumping, the base pressure in the machine was as good as in the absence of absorber.

Table 2.1 shows the typical plasma parameters of Constance. The accuracy and range of the methods used to determine these quantities is discussed in Sections 2.2 and 2.3. As noted in the table, there are two main electron components: a cold component which dominates particle balance in the plasma, and the hot component, which contains the stored energy and dominates energy balance. In addition, there is a low-density (below 8×10^{10} cm^{-3}) 'warm' component in the 1–2 keV range which is micro-unstable and produces whistler rf emission (Garner, 1986 and Garner *et al.*, 1987). This component

Midplane Magnetic Field (On Axis)	3.0	kG
Gas Pressure	5×10^{-7}	Torr
ECRH Power	2	kW
Peak $\beta = 8\pi nT/B^2$	30	%
Ambipolar Potential	150	V
Cold Electron Density	2×10^{11}	cm^{-3}
Cold Electron Temperature	100	eV
Hot Electron Density	4×10^{11}	cm^{-3}
Hot Electron Temperature	400	keV
Ion Temperature (without ICRH)	10	eV

Table 2.1: Typical Constance Plasma Parameters.

provides the connection between the cold electrons and the hot electrons, and can also govern an important energy loss channel.

2.2 Plasma Control

There are three 'knobs' available to the experimenter to vary plasma conditions: the ECRH power, gas pressure, and magnetic field. Most of the data presented in this work, therefore, is accumulated by way of scans where one of these parameters is varied while holding the other two constant.

The applied power is normally measured by a thermistor at the transmitter, and will be referred to as P_{rf}. This is not the power incident on the plasma at high power levels, because reflected power becomes significant. The incident power has been measured both by subtracting the reflected power measured at the transmitter and by the waveguide located opposite the launching horn in the machine, and the two measurements agree. The incident power will be called P_{inc}, and is plotted versus P_{rf} in Fig. 2.3. The rf power can be set to an accuracy of about 10%.

The magnetic field is controlled by the process controller, and is parameterized by the midplane on-axis field B_0. Shots taken with $B_0 = 3.75$ kG, with the resonance located at the center of the device, indicate that B_0 can be set within an accuracy of about 1%.

The gas pressure is controlled by a piezo-electric valve which allows a fixed flow of hydrogen gas into a tube which extends into the vacuum chamber. The valve is pulsed

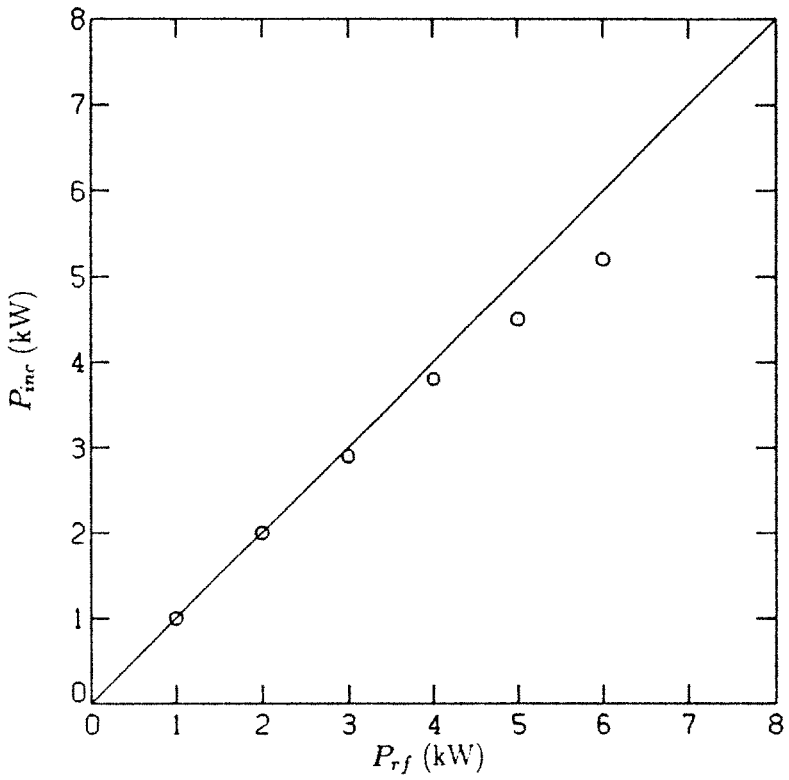

Figure 2.3: Rf power incident on the plasma vs. forward power measured at the transmitter.

on to a preset voltage before the shot and is usually turned off when the rf is turned off. This allows a consistent gas pressure level to be maintained from shot to shot without excessively loading the walls with hydrogen. The gas pressure is measured with a fast ion gauge located on a tube attached to the center chamber of the device and is representative of the pressure at the edge of the plasma. Although magnetically shielded, the reading does decrease by about a factor of two when the magnet is on with $B_0 = 3.0$ kG. For simplicity, and consistency with other work on Constance, I will quote the field-reduced reading. In addition, the presence of plasma reduces the pressure due to the pumping action of the plasma itself; I will quote the pressure reading during the plasma steady-state, and therefore my values for gas pressure will tend to be around 20% lower than values taken immediately before the plasma is formed.

The effect that the variation of magnetic field, rf power, and gas pressure has on the plasma will be discussed in Chapter 4.

2.3 Diagnostics

The Constance experiment has a wide variety of diagnostics; their placement on the device is shown in Fig. 2.4. This section briefly describes the ones used to gather data presented in this work, with mention of the person primarily responsible for its construction and maintenance if not myself. Since the x-ray and scintillator probe measurements are the key measurements presented in this thesis and require careful analysis, detailed discussions of them are given in Appendices A and B.

Microwave Interferometer

Donna Smatlak

A single 24 GHz interferometer scans a chord crossing the midplane at a 45° angle, and gives the electron line density nl across the chord. Since the hot electrons have increased relativistic masses, the plasma frequency for the hot electrons is reduced and the interferometer is less sensitive to the hot electrons by $\langle 1/\gamma \rangle$, a factor of 40% for $T = 500$ keV. For the standard $B_0 = 3.0$ kG case, the chord has a length of about 20 cm

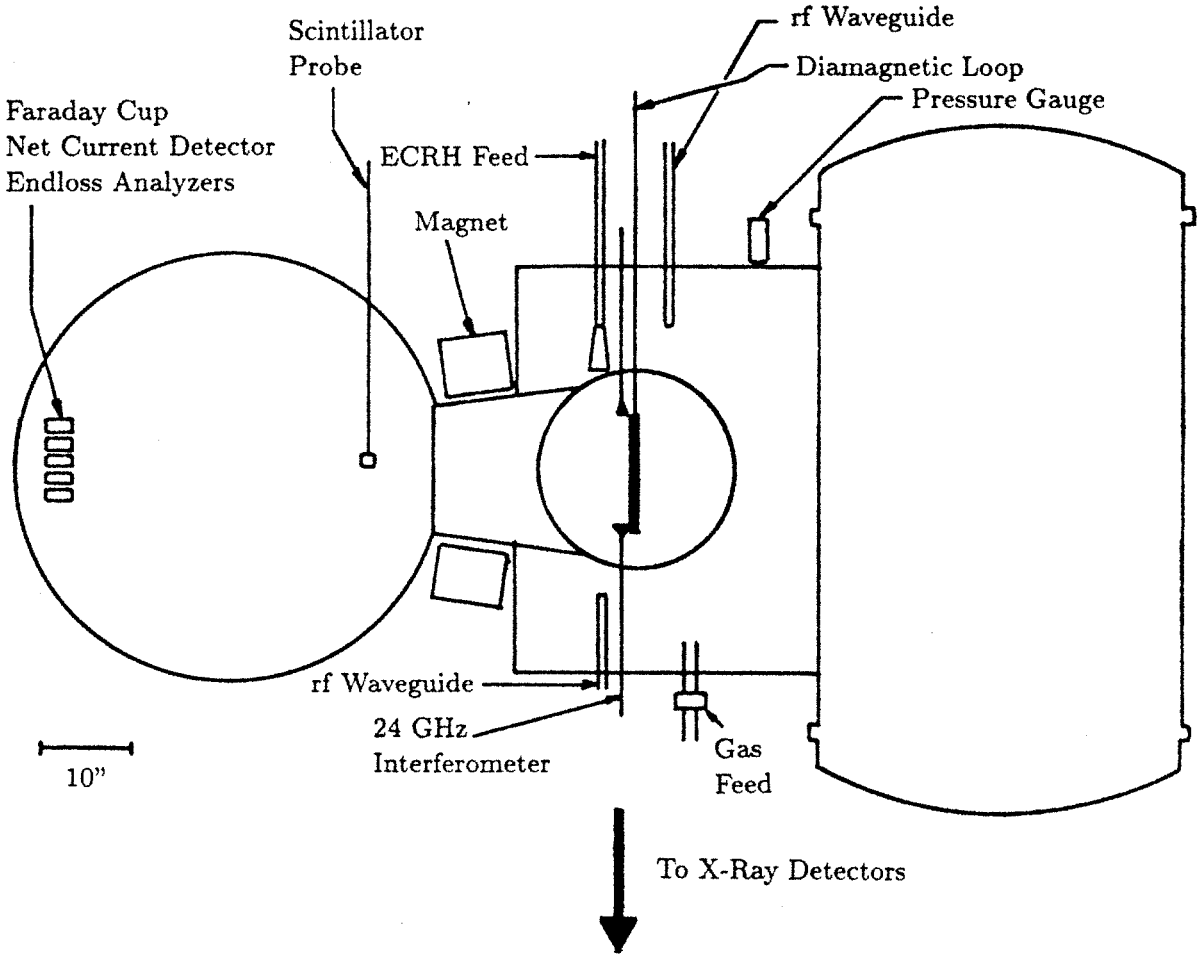

Figure 2.4: Diagnostics on Constance B.

across the plasma; when a density is quoted, it is the chord-averaged density given by dividing nl by this length. The plasma density profile has not been directly measured, but visible light images suggest that the peak density may be as much as twice the average value.

Diamagnetic Loops

Xing Chen

Four diamagnetic loops have been used in Constance: two circular loops located near the midplane, an elliptical loop located near the mirror peak, and a baseball seam-shaped loop. All of these loops surround the plasma and are made large enough to avoid limiting the plasma size. The voltage from a loop, which is proportional to $d\Phi/dt$, where Φ is the magnetic flux inside the loop, is integrated using a fast electronic integrator. The loop response is dependent on the plasma pressure profile; the thesis research presently being conducted by Xing Chen is devoted to the measurement of the pressure profile and the theoretical analysis of the equilibrium, and his results will be used here for estimating the plasma stored energy $W_\perp$ from the integrated loop voltage V_{loop}. He estimates that the conversion, given by $W_\perp$ (J) $= 2.4 V_{loop}$ (V), has an accuracy of 10%.

CCD and X-Ray Pinhole Cameras

Xing Chen, Donna Smatlak

Constance is equipped with a CCD camera which records visible light images on videotape with time resolution given by the scan rate of 30 scans/s. Two x-ray pinhole cameras have been used: one which produces a shot-integrated photograph on x-ray film, and one which uses a system composed of a CsI(Tl) scintillator, a coherent fiber optic bundle, an image intensifier, and the CCD camera to provide real time x-ray images which are recorded on videotape. These diagnostics were the first to reveal the baseball seam-shaped equilibrium of the Constance plasma (Smatlak *et al.*, 1987).

X-Ray Spectroscopy

X-ray spectra have been taken over a range of photon energies from 1 keV to 1.5 MeV using three detectors: a NaI(Tl) detector (0.03–1.5 MeV), a high-purity Ge detector (2-150 keV), and a Si(Li) detector (1–12 keV). The NaI(Tl) detector is the standard diagnostic used to determine the hot electron temperature, and the fitting method gives a chord-averaged temperature which is accurate to within 5%, or 20 keV. X-ray bremsstrahlung theory and detector response algorithms are described in Appendix B.

Endloss Arrays

Dan Goodman

Each endwall has an array of five gridded endloss analysers (ELAs), five Faraday cups, and five net current collectors. The ELAs have three grids followed by a current collector. The first (ion repeller) grid is biased to repel ions with energies below its potential; the second (electron repeller) grid is biased to repel electrons with energies below its potential; and the third grid is used to suppress the collection of secondary electrons which arise from the grids. The gridded ELAs are used to measure the endloss distribution of ions and electrons with energies below 5 keV (grid biases above 5 keV tend to produce arcing). The Faraday cups are biased to measure the ion or electron endloss current. The net current collectors are unbiased and measure the net endloss current.

Scintillator Probes

These probes consist of small (4 mm diameter) plastic scintillators coupled with fiber optic guides to photo-multiplier tubes. The scintillators have entrance windows which discriminate according to electron energy. They produce a signal which is proportional to endloss power density and have been used in arrays to measure the endloss distribution of hot electrons. The calibration and analysis of the scintillator probe signal is described in Appendix B.

Microwave Emission

Rich Garner

The centerpiece of the microinstability studies (Garner, 1986, Garner *et al.*, 1987) is the measurement of microwave emission. This has been done in two ways: measurement of total (ECRF-filtered) instability rf power using a stub waveguide with a diode, and spectral rf measurements using a spectrum analyser. In addition, the total (unfiltered) rf power (composed almost entirely of applied ECRF) is measured by a stub waveguide and diode. The unfiltered detector has also been used to determine the applied rf power — at high levels a sizable fraction (up to 25%) is reflected in the waveguide system leading from the transmitter to the experiment. The measured power levels are in agreement with the level obtained by subtracting the reflected power, which is measured at the transmitter, from the total power measured at the transmitter. The rf diodes were calibrated with a microwave source and a bolometer, and the power entering the waveguide may be determined to within 10% accuracy.

The time evolution of the signals from most of these diagnostics is shown in Fig. 2.5, which is from a shot with $P_{rf} = 5$ kW and $B_0 = 3.0$ kG. The stored energy is 120 J. The fluctuations seen on many of the diagnostics are due to whistler microinstability rf.

2.4 Data Acquisition and Analysis

The Constance experiment uses CAMAC-based data acquisition with a VAX 11/750 computer in conjunction with the VAX/VMS data acquisition software package MDS[1] (Fredian and Stillerman, 1985). Two types of digitizers have been used for the data presented here: slower ones (LeCroy 8212) which sample at 2 kHz throughout the shot, and faster ones (LeCroy 2264) which are used for rates up to 4 MHz. There are also PHA modules (LeCroy 3512/3587/3588) for obtaining time-resolved x-ray pulse-height spectra, and a phase digitizer (Jorway 1808) for the interferometer. All of these modules

[1] A different data system, written by Evelio Sevillano and Jim Sullivan of the Tara group, was used for the first 4000 shots.

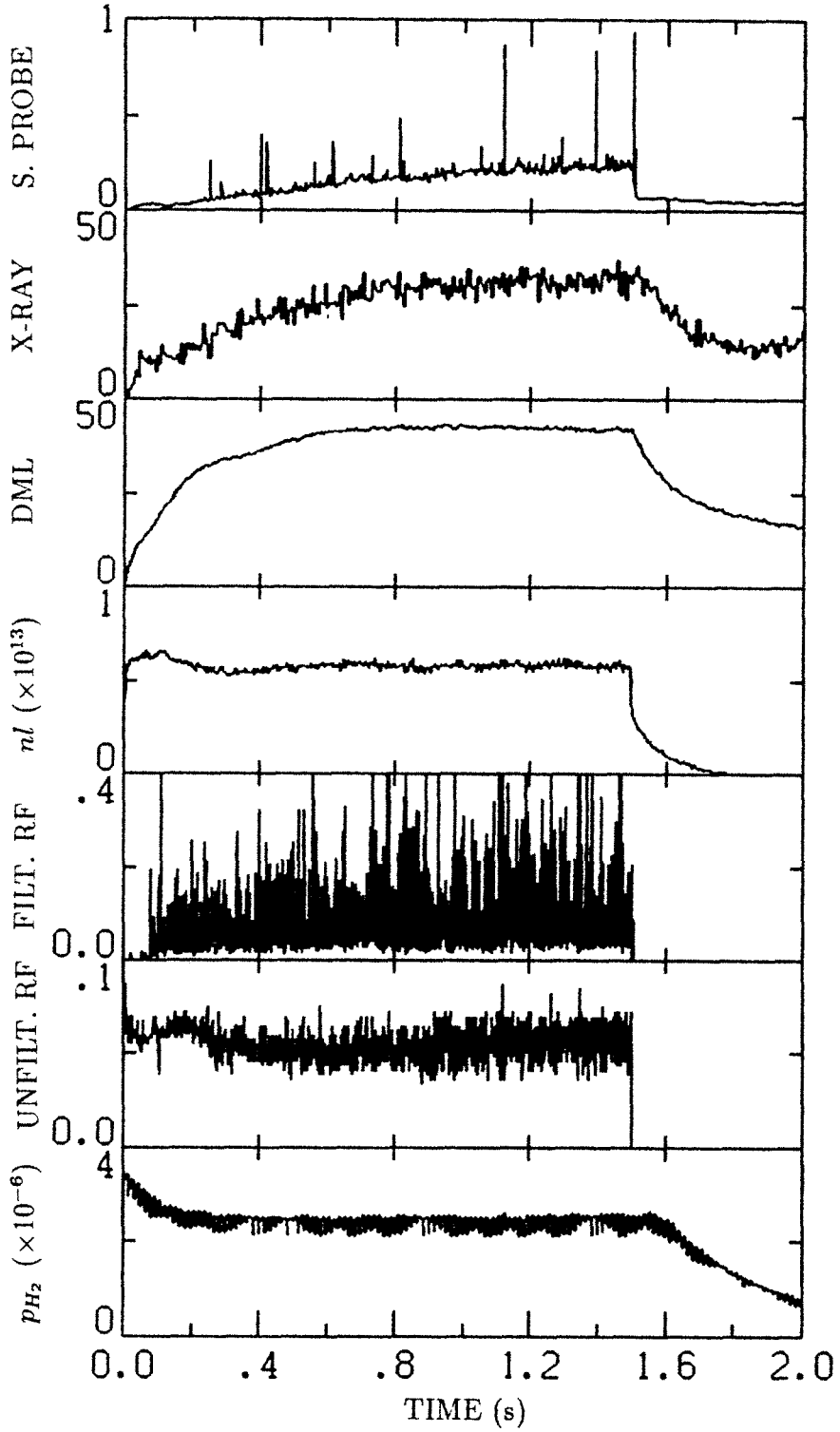

Figure 2.5: A shot in which the rf is applied for 1.5 s followed by a 0.5 s decay: a) p_{H_2} (Torr), b) unfiltered rf diode (V), c) filtered rf diode (V), d) nl (cm^{-3}), e) integrated DML signal (V), f) hard x-ray count rate (kHz), and g) scintillator probe signal (μA).

are triggered by a CAMAC timer module (Jorway 221/222); the timer is triggered at the start of the shot by the Gould 484 process controller after the magnetic field reaches a constant value. The klystrons and other systems are gated by the process controller.

The limiting factor in the shot cycle tends to be the time required for magnet cooling. The maximum shot rate at the standard field of $B_0 = 3.0$ kG is around 10 shots per hour. Constance has excellent shot-to-shot reproducibility; however, around 20 shots are required to accumulate sufficient x-ray statistics to observe the time evolution of the x-ray spectrum in the early portion of the shot. Because of this, the time evolution of the x-ray spectrum is available for only a limited subset of plasma conditions. Under most conditions, however, a single shot is sufficient to ascertain the steady-state x-ray spectrum by summing spectra over the final half second of the shot.

2.5 Magnetic Geometry

The magnetic geometry of Constance is quite complicated and very difficult to visualize. The surface of constant plasma parameters is a drift surface, which is the surface of field lines that share a common minimum field value (the drift surfaces have a weak dependence on particle pitch angle which I ignore here). Fig. 2.6 shows the strongly-heated surface whose minimum field touches the resonant $|B| = 3.75$ surface (the so-called 'tangent' surface) for the standard case of $B_0 = 3.0$ kG. Also indicated is the minimum field curve, which is resonant for this surface and reflects the shape of the magnet. It is this strong-heating curve that gives rise to the baseball seam shape of the plasma.

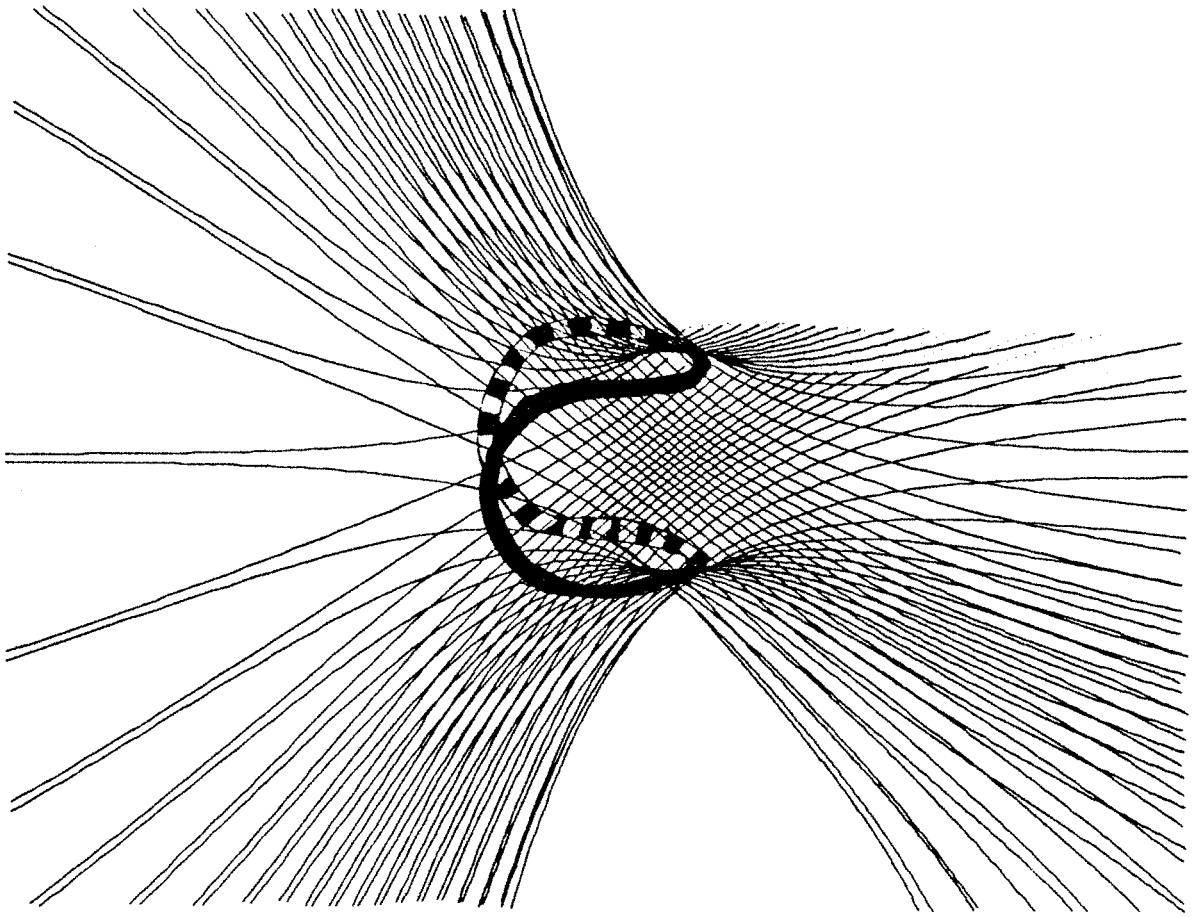

Figure 2.6: The 'tangent' drift surface for the case of $B_0 = 3.0$ kG. The curve of minimum field, which is the location of resonance for this surface, has the shape of a baseball seam. The view is from a position 10° above horizontal at the midplane.

Chapter 3

Theory of RF Diffusion

The experiments described in this work are aimed towards two goals: measuring the processes governing velocity-space diffusion of electrons in the Constance plasma, and determining the effect those processes have on heating and confinement. It is essential, therefore, to first be familiar with the current understanding of the subject. This chapter presents an overview of ECRH theory pertinent to the experiment and establishes the framework within which the experimental results will be analyzed. My approach is to use derivations which stay closest to the underlying physics of the problem; the formal quasilinear treatment of relativistic ECRH is given in the paper by Bernstein and Baxter (1980).

The first section in this chapter presents the formalism of velocity-space diffusion. In this description, all of the physics is contained in the diffusion tensor D. Losses due to unconfined particle drifts are small in the Constance plasma and will be ignored; these effects can be important in devices such as EBT (Batchelor *et al.*, 1987). Sections 3.2 and 3.3 describe the velocity-space diffusion tensor due to collisions and cyclotron-resonant rf. The issue of super-adiabaticity, the situation in which velocity-space motion becomes non-diffusive, will be addressed in section 3.4 where the mapping technique which leads to super-adiabatic effects is described. Stochasticity mechanisms which can remove the super-adiabatic barrier to rapid diffusion will be analyzed in section 3.5. Finally, in section 3.6, I will summarize what aspects of ECRH theory can and cannot be measured in an experiment such as Constance.

3.1 Velocity-Space Diffusion

This chapter deals primarily with the hot electrons, and the distribution function $f(\mathbf{p})$ will be used to denote the hot component (that is, 'h' subscripts will be suppressed). The distribution function of hot electrons in a device such as Constance is governed by the diffusion equation

$$\begin{aligned} \frac{\partial f}{\partial t} &= S(\mathbf{p}) + \nabla \cdot \mathsf{D} \cdot \nabla f \\ &= S(\mathbf{p}) - \nabla \cdot \mathbf{\Gamma}, \end{aligned} \tag{3.1}$$

where $\mathbf{\Gamma} = -\mathsf{D} \cdot \nabla f$ is the velocity-space current and $S(\mathbf{p})$ is the hot electron source due to the heating of cold electrons. The particle balance equation for the hot electrons is then given by

$$\begin{aligned} \frac{dn}{dt} &= \int d^3p S(\mathbf{p}) - \int d^3p \nabla \cdot \mathbf{\Gamma} \\ &= n_c \nu_{c\to h} + \int_{lc} \mathbf{dS} \cdot \mathbf{\Gamma} \\ &= n_c \nu_{c\to h} + \int_{lc} dp 2\pi p \sin\theta_l \Gamma_\theta \\ &= n_c \nu_{c\to h} + \int_{lc} dE \frac{\gamma}{mc^2} 2\pi \sin\theta_l \Gamma_\theta. \end{aligned} \tag{3.2}$$

The integrals are taken along the loss-cone (lc) and the momentum p is in units of mc; E, however, retains units and is the electron kinetic energy. The total energy, including the rest mass, will always be represented by γ. Eq. 3.2 shows the balance between the particle source $n_c \nu_{c\to h}$ and endloss, which is the integral along the loss cone $\theta = \theta_l$ of the endloss current distribution

$$\frac{dJ}{dE} = \frac{\gamma}{mc^2} 2\pi \sin\theta_l \Gamma_\theta(p, \theta_l). \tag{3.3}$$

The power balance equation is given by the energy moment of the diffusion equation,

$$\begin{aligned} \frac{dW}{dt} &= \int d^3p E S(\mathbf{p}) - \int d^3p E \nabla \cdot \mathbf{\Gamma} \\ &= -\int d^3p \nabla \cdot (E\mathbf{\Gamma}) + \int d^3p \mathbf{\Gamma} \cdot \nabla E \\ &= \int_{lc} dE \frac{\gamma}{mc^2} 2\pi \sin\theta_l E \Gamma_\theta + \int d^3p \frac{mc^2}{\gamma} p \Gamma_p. \end{aligned} \tag{3.4}$$

Here I have assumed that the source is at zero energy, that is $S(\mathbf{p}) = n_c \nu_{c \to h} \delta^3(p)$, and contributes no energy to the hot electron component. The first term represents the endloss power, which is the integral along the loss cone of the endloss *power* spectrum

$$dP/dE = EdJ/dE. \tag{3.5}$$

The second term is the heating term, and gives the power absorbed (or lost) due to the p-directed velocity-space current Γ_p.

The diffusion tensor D can, in general, be written in the form

$$\mathsf{D} = \langle \frac{\Delta \mathbf{p} \Delta \mathbf{p}}{2\Delta t} \rangle, \tag{3.6}$$

where Δt is the correlation time and the angle brackets represent averages over many particles and/or time. The following two sections present D for the two dominant diffusion mechanisms present in Constance: collisions and rf.

3.2 The Collisional Diffusion Tensor

The collisional diffusion tensor, $\mathsf{D}^{coll}(p, \theta)$, has been calculated by Cohen *et al.* (1983) for mirror geometry. The pitch-angle component is given by

$$D^{coll}_{\theta\theta} = p^2 \frac{\nu_e}{2} \frac{\sin\theta(1 - \sin\theta)}{\cos^2\theta}, \tag{3.7}$$

where the angle terms represent the average effect of off-midplane collisions on the midplane distribution function; this is the only effect of the mirror geometry. The drag component D^{coll}_{pp} is considerably smaller and will be ignored here (it doesn't contribute to endloss, anyway); p and θ kicks from collisions are uncorrelated, so the off-diagonal terms $D^{coll}_{p\theta}$ equal zero.

The velocity-space current associated with D is

$$\Gamma^{coll}_{\theta}(p, \theta) = -\frac{\nu_e}{2} \frac{\sin\theta(1 - \sin\theta)}{\cos^2\theta} p \frac{df}{d\theta} \tag{3.8}$$

$$\Gamma^{coll}_{p}(p, \theta) \simeq 0, \tag{3.9}$$

and the endloss power spectrum is given by Eqs. 3.3 and 3.5. One can see, then, that a measurement of dP/dE (made with the scintillator probe array in my experiments) gives a measure of $df/d\theta$ along the loss cone boundary, as long as the form for $D_{\theta\theta}^{coll}$ is correct.

3.3 The rf Diffusion Tensor

The rf diffusion tensor, D^{rf}, has four nonzero components; these are, however, related by the equation for the *diffusion paths* in velocity space: $\Delta\theta = a_l(p,\theta)\Delta p$. The diffusion paths are different for each harmonic number l. The task, then, is divided into two parts: that of calculating Δp, and that of determining $a_l(p,\theta)$. The former is performed in subsection 3.3.1 using the technique of unperturbed orbits; analytic results for low energy fundamental heating will be shown in 3.3.2. The diffusion paths will be then be derived in 3.3.3, and an example calculation of rf absorption using the D^{rf} valid for low energies will be given in 3.3.4. Finally, an approximate calculation of D^{rf} for arbitrary energies will be given in 3.3.5 and the result will be compared to a Monte Carlo calculation.

3.3.1 Orbit Integral

The unperturbed orbit integral approach solves for the kick in momentum

$$\Delta p = \int dt \frac{dp}{dt} \tag{3.10}$$

$$= \frac{-e}{mc}\int dt \frac{1}{p}\mathbf{p}\cdot\mathcal{E}, \tag{3.11}$$

using the unperturbed ($\mathcal{E} = 0$) orbits for the electron

$$\begin{aligned} x(t) &= \rho(t)\cos\phi(t) \\ y(t) &= \rho(t)\sin\phi(t) \\ z(t) &= \int_0^t v_{\|}(\tau)d\tau. \end{aligned} \tag{3.12}$$

where $\phi(t)$ is the phase angle of the electron's cyclotron motion,

$$\phi(t) = \int_0^t d\tau \omega_c(\tau) + \phi_0, \tag{3.13}$$

and $\mathcal{E}$ is the rf electric field. As before, p is normalized to mc.

A combined X-mode and O-mode electric field may be written

$$\mathcal{E}(\mathbf{r}, t) = (\hat{\mathbf{x}}\mathcal{E}_\perp + \hat{\mathbf{z}}\mathcal{E}_\parallel)\sin(\mathbf{k}\cdot\mathbf{r} - \omega t), \tag{3.14}$$

where $\mathbf{k} = k_\perp\hat{\mathbf{y}} + k_\parallel\hat{\mathbf{z}}$, and the magnetic field is aligned with $\hat{z}$. Using the Bessel function identity

$$\sin(a + x\sin\theta) = \sum_{l=-\infty}^{+\infty} J_l(x)\sin(a + l\theta),$$

the orbit integral may be written as

$$\Delta p = \frac{e}{mc}\sum_{l=-\infty}^{+\infty}\int dt(\mathcal{E}_\perp \sin\theta\sin\phi - \mathcal{E}_\parallel\cos\theta)J_l(k_\perp\rho)\sin(\chi_l), \tag{3.15}$$

where χ_l is the relative phase between the wave and the electron for the lth harmonic:

$$\chi_l(t) = \int_0^t d\tau(\omega - k_\parallel v_\parallel - l\omega_c) - l\phi_0. \tag{3.16}$$

To put Eq. 3.15 in a more useful form, one can use the identity

$$\begin{aligned}\sin\phi\sin\chi_l &= \frac{1}{2}[\cos(\chi_l - \phi) - \cos(\chi_l + \phi)] \\ &= \frac{1}{2}[\cos\chi_{l+1} - \cos\chi_{l-1}]\end{aligned}$$

in the $\mathcal{E}_\perp$ term and shift l by 1 in the sums to get

$$\Delta p = \frac{e}{mc^2}\sum_{l=-\infty}^{+\infty}\int dt\left[\frac{\mathcal{E}_\perp}{2}\sin\theta(J_{l-1} - J_{l+1})\cos\chi_l - \mathcal{E}_\parallel\cos\theta J_l\sin\chi_l\right]. \tag{3.17}$$

The electron is in resonance with the lth harmonic when χ_l is stationary, that is, when

$$\chi_l'(t) = \omega - k_\parallel v_\parallel - l\omega_c = 0. \tag{3.18}$$

The $\mathcal{E}_\perp$ term has a factor of 1/2 because only the right-hand circularly polarized component resonates with the electron.

The orbit integral Eq. 3.17 cannot be analytically evaluated exactly, even for a parabolic mirror field in which the orbit quantities have analytic forms. The next section uses a narrow resonance approximation to evaluate Eq. 3.17 for fundamental X-mode heating of low energy electrons, applicable to the cold electron component in Constance.

3.3.2 Evaluation of the Orbit Integral for Low Energies

In this section I will focus on $l = 1$ X-mode heating, since the approximations used to evaluate Eq. 3.17 are valid only for lower energy electrons for which $l = 1$ X-mode heating dominates; in addition, the equations will be written non-relativistically. I will suppress the l subscripts. The main difficulty in computing the orbit integral Eq. 3.17 is in the integration of $\cos\chi$, a function which oscillates rapidly except near resonance. The approximation methods utilize the Taylor expansion of $\chi(t)$ about some point in the orbit (defined here at t=0):

$$\chi(t) = \chi(0) + \chi'(0)t + \chi''(0)\frac{t^2}{2} + \chi'''(0)\frac{t^3}{6} + \cdots. \tag{3.19}$$

If $t = 0$ is taken at the point of exact resonance, then $\chi'(0) = 0$. The t^2 and t^3 coefficients are given, using $d/dt = v_\parallel d/ds$, by

$$\chi'' = k_\parallel \frac{\mu}{m}\frac{dB}{ds} - lv_\parallel \frac{d\omega_c}{ds}, \tag{3.20}$$

$$\chi''' = k_\parallel \frac{\mu}{m} v_\parallel \frac{d^2B}{ds^2} + l\frac{\mu}{m}\frac{dB}{ds}\frac{d\omega_c}{ds} - lv_\parallel^2 \frac{d^2\omega_c}{ds^2}, \tag{3.21}$$

where $\mu = mv_\perp^2/2B$ is the magnetic moment. There are three special cases: 1) the electron turns well beyond resonance, 2) the electron turns near resonance, and 3) the resonance is located at the mirror minimum or maximum where dB/ds=0.

In Case 1, one can set $t = 0$ to be at exact resonance and the t^2 term is the dominant term. Eq. 3.17 may then be integrated across the lth resonance to give the approximate kick in energy that the electron receives:

$$\begin{aligned}\Delta p &\simeq \frac{e\mathcal{E}_\perp}{2mc}\sin\theta\int_{-\infty}^{+\infty}dt\cos\left(\chi(0)+\chi''(0)\frac{t^2}{2}\right)\\ &\simeq \frac{e\mathcal{E}_\perp}{2mc}\sin\theta\cos\left(\chi(0)+\frac{\pi}{4}\right)\sqrt{\frac{2\pi}{|\chi''(0)|}},\end{aligned} \tag{3.22}$$

where all quantities are evaluated at resonance, and I have approximated $J_0(k_\perp\rho) = 1$ and $J_2(k_\perp\rho) = 0$. In this case, the electron spends an effective time in resonance

$$\tau_{eff} = \sqrt{\frac{2\pi}{|\chi''(0)|}}, \tag{3.23}$$

which, from Eq. 3.19, is the time required for χ to slip $\pi/2$ radians.

In Case 2, the electron turns near resonance and the t^3 term dominates. In this case, it is more convenient to set $t = 0$ at the turning point, so that $v_\parallel(0) = 0$ and the coefficients in Eq. 3.19 have simple forms. Retaining the linear and cubic terms, one gets

$$\begin{aligned}\Delta p &\simeq \frac{e\mathcal{E}_\perp}{2mc}\sin\theta\int_{-\infty}^{+\infty}dt\cos\left(\chi(0)+\chi'(0)t+\frac{\chi'''(0)}{6}t^3\right)\\ &\simeq \frac{e\mathcal{E}_\perp}{2mc}\sin\theta\,2\pi\left(\frac{\chi'''(0)}{2}\right)^{-1/3}\mathrm{Ai}\left[\left(\frac{\chi'''(0)}{2}\right)^{-1/3}\chi'(0)\right]\cos\chi(0),\end{aligned} \tag{3.24}$$

where all quantities are evaluated at the turning point, and $\mathrm{Ai}(x)$ is the Airy function. In this case, the electron spends an effective time in resonance

$$\tau_{eff} = 2\pi\left(\frac{\chi'''(0)}{2}\right)^{-1/3}\mathrm{Ai}\left[\left(\frac{\chi'''(0)}{2}\right)^{-1/3}\chi'(0)\right]. \tag{3.25}$$

When the turning point and resonance exactly coincide ($\chi'(0) = 0$), τ_{eff} is the time required for the relative phase to slip 1.2π radians.

In Case 3, there are two possibilities: 1) $v_\parallel \neq 0$ at resonance at the mirror minimum, in which case the result of Case 2 applies (except all quantities are evaluated at the

mirror minimum and $\chi'(0) = 0$), and 2) $v_{\|} = 0$ at resonance at the mirror minimum or maximum, in which case the electron stays in resonance indefinitely and the linear theory breaks down. The case of resonance at the mirror maximum is somewhat singular, since the particle lies on the loss-cone where the distribution function vanishes.

At this point, Δp from a resonance crossing has been determined for the case of low energies when the expansion 3.19 is valid, and D^{rf} can be computed once the equation for the diffusion paths is known; this is done in the next section.

3.3.3 Diffusion Paths

The equation for the diffusion paths, $\Delta\theta = a_l(p,\theta)\Delta p$, relates the kick in momentum that an electron receives at resonance to the kick in the *midplane* pitch angle. A complication results from the fact that for very energetic electrons the resonance can be spatially broad, and the exact resonance point is not well-defined. My assumption in writing the equation for $a_l(p,\theta)$ will be that, on the average, the effect of the resonance crossing is the same as would result from an impulsive kick at exact resonance. Analysis of velocity-space trajectories from a numerical particle-following code support this assumption.

The diffusion path is found by relating the kick in θ at resonance back to the midplane. This is done more easily by first determining the diffusion paths in (E,μ) space, since both E and μ are constants of motion outside of resonance. I will define $\mu = mc^2p_\perp^2/2B$, rather than using the correct relativistic form, which has a factor of $1/\gamma$ in it. The diffusion paths have a simpler form using this definition.

Since the resonance location depends on $k_{\|}$, one would assume *a priori* that the diffusion paths have a $k_{\|}$ dependence. In fact, this is not the case. The reason is subtle: if one includes the rf magnetic field in the calculation of the μ kick, where it makes a contribution, the effect of nonzero $k_{\|}$ is cancelled by the change in the location of the resonance (Rognlien, 1983a). This simplifies matters enormously, since only D_{pp}^{rf} need be calculated for a given $k_{\|}$ to determine the full tensor D.

A kick in $p_\perp$ at resonance translates into kicks in E and μ:

$$\gamma \Delta E = mc^2 p_\perp \Delta p_\perp \tag{3.26}$$

$$\Delta \mu = mc^2 p_\perp \Delta p_\perp / B. \tag{3.27}$$

For $k_\parallel = 0$, B at resonance is given by the resonance condition $\omega = l\omega_c$, or defining B_{rf} by $\omega = eB_{rf}/mc$, one can combine Eqs. 3.26 and 3.27 to get

$$\Delta E = \frac{B_{rf}}{l} \Delta \mu, \tag{3.28}$$

which says that the diffusion for a given l runs along paths given by

$$E - \mu \frac{B_{rf}}{l} = \text{constant}. \tag{3.29}$$

The calculation of $a_l(p, \theta)$ is reduced to converting Eq. 3.28 to (p, θ) coordinates; this leads to the result

$$a_l(p, \theta) = \frac{1}{\sin\theta \cos\theta} \left(\frac{lB_0}{\gamma B_{rf}} - \sin^2\theta \right), \tag{3.30}$$

where B_0 is the midplane magnetic field.

For a given value of D^{rf}_{pp}, then, the other elements of D^{rf} are:

$$D^{rf}_{p\theta} = a_l(p, \theta) D^{rf}_{pp} \tag{3.31}$$

$$D^{rf}_{\theta p} = a_l(p, \theta) D^{rf}_{pp}$$

$$D^{rf}_{\theta\theta} = a_l^2(p, \theta) D^{rf}_{pp}. \tag{3.32}$$

3.3.4 Diffusion of Low Energy Electrons

The results of 3.3.2 and 3.3.3 may now be combined to evaluate the velocity-space diffusion of low energy electrons due to $l = 1$ X-mode heating. Case 2 of section 3.3.2 is of particular interest, since the effect of rf diffusion is to push the electron turning points close to the resonance location.

The time between resonances in Case 2 is $\Delta t = \tau_b/2$, where τ_b is the round-trip bounce time. This is geometry-dependent, as is τ_{eff}, so I will use a parabolic mirror field

$B(z) = B_0[1 + (z/L)^2]$, for which the z motion is sinusoidal in time and $\tau_b = 2\pi L/v_\perp$, where $v_\perp$ is evaluated at the midplane. D_{pp} is then given by

$$\begin{aligned} D_{pp}^{rf} &= \langle \frac{\Delta p \Delta p}{2\Delta t} \rangle \\ &= (\frac{e\mathcal{E}_\perp}{2mc})^2 \frac{\tau_{eff}^2}{\tau_b} \sin^2\theta \langle \cos^2\chi(0) \rangle. \end{aligned} \tag{3.33}$$

If $\chi(0)$ is a random quantity on successive resonance crossings, then the diffusion is stochastic, and $\langle \cos^2\chi(0) \rangle = 1/2$. The situation where $\chi(0)$ becomes non-random will be discussed in section 3.4.

Using the formula for τ_{eff} given in Eq. 3.25 and the integral which gives the absorbed power P_{abs} in Eq. 3.4, one can now calculate the heating rate P_{abs}/n for a particular choice of distribution function. For simplicity, I will choose $f(p,\theta)$ to be an isotropic Maxwellian of temperature T, and multiply D by $\delta(\cos\theta - \cos\theta_h)$ so that only heating of turning-point resonant electrons is treated. Here $\cos\theta_h$ is the midplane pitch-angle for these electrons given by $\sin^2\theta_h = B_0/B_{rf}$. Leaving out the details, the resulting heating rate is

$$\frac{P_{abs}}{n} = \frac{(e\mathcal{E}_\perp)^2}{m} \frac{\sqrt{\pi}}{3} \mathrm{Ai}^2(0)\Gamma(4/3) \frac{c}{L} \left(\frac{L^2}{c^2\omega}\right)^{2/3} \frac{1}{R^{1/6}(R-1)^{2/3}} \left(\frac{mc^2}{2T}\right)^{1/6}. \tag{3.34}$$

For $\mathcal{E}_\perp = 100$ V/cm, $L = 30$ cm, $\omega/2\pi = 10.5$ GHz, and the heating resonance at $R = 1.25$ (corresponding to $B_0 = 3.0$ kG), this formula gives the enormous heating rate of 500 eV/μs, which is only 100 times lower than would be experienced by a 100 eV electron in a 100 V/cm dc electric field. On the other hand, a similar calculation for electrons which turn beyond resonance (Case 2 of section 3.3.2) gives a heating rate on the order of 10 eV/μs. One can see from this that the diffusion strength varies over an order of magnitude in the resonant region of velocity space between θ_h and θ_l, and results will therefore be very sensitive to the variation of the distribution function across that region. In the actual situation, of course, the first term in Eq. 3.4, which represents endloss power, limits the net amount of power that the electrons absorb, as well as the

fact that power can go into raising the density (dn/dt) as well as raising the temperature. Furthermore, the distribution function in the 1 keV range tends to be micro-unstable, and micro-instability rf-induced endloss and micro-unstable rf emission further limit the net power absorbed. Finally, the absorption itself reduces the electric field strength at resonance, so that the 100 V/cm vacuum field represents an upper bound.

3.3.5 Hot Electron Diffusion in a Parabolic Well

Analytic progress can be made with the fully relativistic multiple-l form for Δp (Eq. 3.17) if one chooses a parabolic B field as was done in the preceding calculation. In this case, the particle motion in z is sinusoidal, $z(t) = z_b \sin(\omega_b t)$, where z_b is the bounce point. This allows one to perform the integral in Eq. 3.16 for the wave/particle relative phase χ_l, with the result

$$\chi_l = \omega t - l\omega_c t + \frac{l\omega_{c0}}{4\omega_b} \sin 2\omega_b t - k_\parallel z_b \sin \omega_b t - l\phi_0, \tag{3.35}$$

where

$$\overline{\omega_c} = \omega_{c0}[1 + \frac{1}{2}(\frac{z_b}{L})^2]$$

is the average cyclotron frequency with $\omega_{c0} = eB_0/\gamma mc$. The $\cos \chi_l$ term then introduces two additional Bessel function expansions:

$$\cos \chi_l = \sum_{mn} J_m(\frac{l\omega_{c0}}{4\omega_b}) J_n(k_\parallel z_b) \cos(\omega t - l\overline{\omega_c} t + (2m - n)\omega_b t - l\phi_0). \tag{3.36}$$

Since $(J_{l-1} - J_{l+1}) \sin\theta$ varies little in the integral in Eq. 3.17, it can be replaced by average values and the integral over χ_l may be performed. giving the equation for the cumulative kick in p at time t for an X-mode field:

$$\Delta p = \frac{e\mathcal{E}_\perp}{2mc} \sin\theta \sum_{lmn} (J_{l-1} - J_{l+1}) J_m J_n \left(\cos l\phi_0 \frac{\sin \Omega_{lmn} t}{\Omega_{lmn}} + \sin l\phi_0 \frac{1 - \cos \Omega_{lmn} t}{\Omega_{lmn}} \right), \tag{3.37}$$

where

$$\Omega_{lmn} = \omega - l\overline{\omega_c} + (2m - n)\omega_b$$

is the frequency corresponding to the l,m,n *bounce resonance* which incorporates the effect of cumulative bounces on the wave/particle phase. One can see that τ_{eff} in this framework is a sum over three Bessel functions and terms which oscillate at Ω_{lmn}. The dominant contributions arise from l,m,n values for which Ω_{lmn} is small; these are the bounce resonances, where successive bounces interfere constructively.

The diffusion coefficient is found by computing $\langle(\Delta p)^2/2t\rangle$, where the angles signify an average over initial gyrophases ϕ_0, and setting t equal to the average time it takes for the wave and particle to de-correlate. The average over ϕ_0 gives

$$\begin{aligned}\langle \Delta p \Delta p \rangle &= (\frac{e\mathcal{E}_\perp}{2mc})^2 \sin^2\theta \frac{1}{2}\sum_l (J_{l-1}-J_{l+1})^2 \left[\left(\sum_{mn} J_m J_n \frac{\sin\Omega_{lmn}t}{\Omega_{lmn}}\right)^2 + \right. \\ &\left. + \left(\sum_{mn} J_m J_n \frac{1-\cos\Omega_{lmn}t}{\Omega_{lmn}}\right)^2\right]. \end{aligned} \tag{3.38}$$

In section 3.3.4 the correlation time was assumed to be less than the time between resonance crossings. However, in the present case the concept of a well-defined 'kick' loses meaning, since electrons may experience a number of resonances in the course of a bounce, and these resonances may be fairly broad. Fig. 3.1 shows a plot of Eq. 3.38 over a large number of bounce times; one can readily see that the diffusion strength depends strongly on the correlation time. By setting $t = \tau_b/4$, one recovers the single-resonance diffusion coefficient; this is plotted in Fig. 3.2. For comparison, D_{pp} calculated with the Monte Carlo code MCPAT (Rognlien, 1983b) with artificially imposed randomization of ϕ at each bounce is shown as well. Both the analytic and Monte Carlo D values have been averaged over a range of θ in order to wash out the detailed bounce resonance structure of Eq. 3.38. The Monte Carlo calculation uses electron guiding-center orbits in the actual Constance mirror field; it is apparent that the parabolic field approximation reproduces the single-resonance diffusion coefficient reasonably well.

The question at this point is: What determines the correlation time for the wave/particle phase? A number of *extrinsic* factors can play a role: collisions, rf noise, drifts, etc. But for lower energies, the wave/particle phase is *intrinsically* stochastic: the rf wave itself

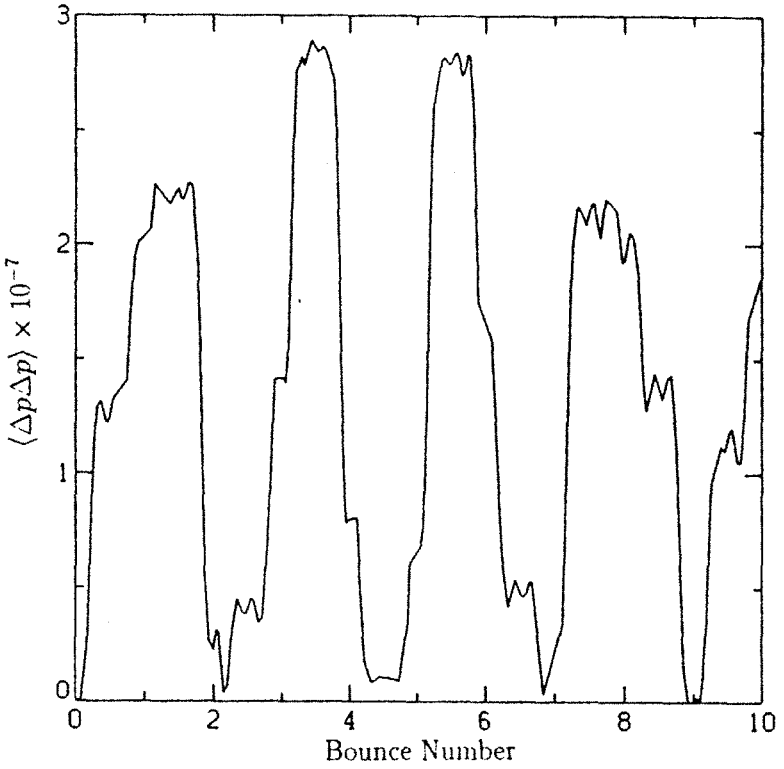

Figure 3.1: $\langle \Delta p \Delta p \rangle$ in the case of a parabolic mirror field and Constance parameters.

causes the phase to vary randomly from bounce to bounce. The maximum energy for which intrinsic stochasticity exists is found from the technique of iterative mapping theory, which is the subject of the next section. The section following that will discuss extrinsic stochasticity and the role it plays in the experiment.

3.4 Mapping Theory

For the range of electric fields present in the Constance experiment ($\mathcal{E} < 100$ V/cm), it will turn out that the maximum energy for intrinsically stochastic motion is fairly low. I will, therefore, once again restrict myself to the problem of fundamental X-mode heating of non-relativistic electrons.

The mapping approach (Lieberman and Lichtenberg, 1983) follows the orbit of a single particle over many bounces, retaining the relative phase χ explicitly. Nonrelativistic electrons receive kicks at a constant B value; thus, $v_{\parallel}$ at resonance is a constant and the

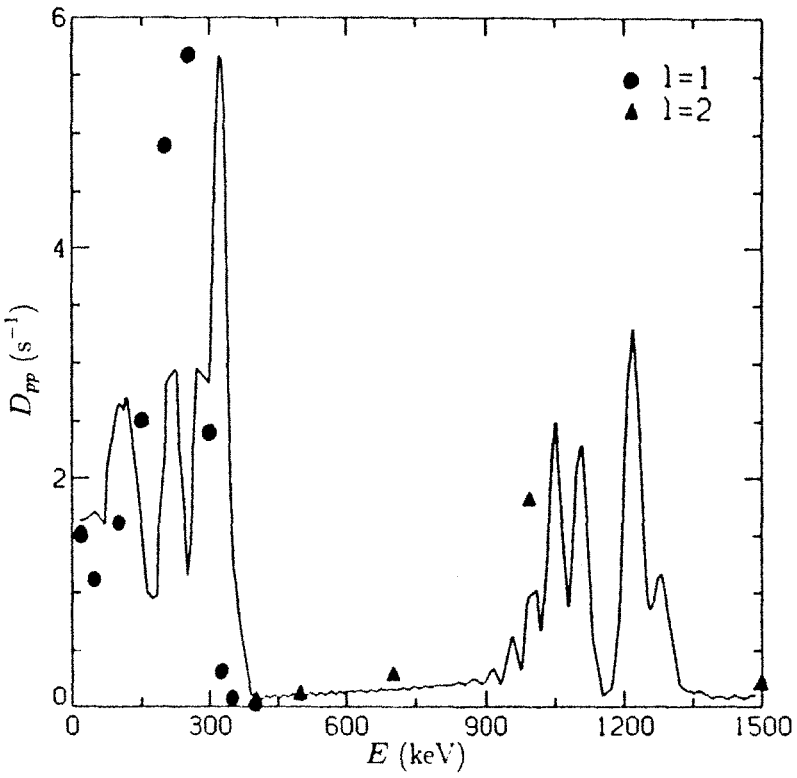

Figure 3.2: The single-resonance diffusion coefficient for X-mode heating and Constance parameters, calculated analytically and with the Monte-Carlo code MCPAT for an electric field of 10 V/cm.

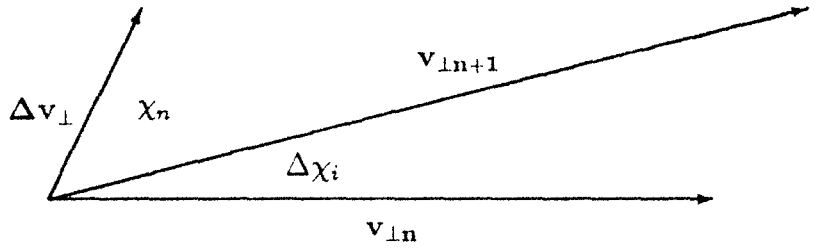

Figure 3.3: Momentum diagram for calculating the kicks in $v_\perp$ and χ in the impulse approximation.

trajectory is given by kicks in $v_\perp$ at resonance. The orbit integral gives the effective time that the electron spends in resonance, τ_{eff}, such that the kick that the electron receives is

$$\Delta v_\perp = \frac{e\mathcal{E}_\perp}{2m}\tau_{eff}\cos\chi. \tag{3.39}$$

One can go further and include the approximate nonlinear modification to the kick (Lieberman and Lichtenberg, 1973) by employing an *impulse approximation*: one uses the τ_{eff} which is calculated from the linear orbit integral to compute the *amplitude* $\Delta v_\perp = (e\mathcal{E}_\perp/2m)\tau_{eff}$, but assumes that the kick comes in an instantaneous impulse so that the actual kick may be computed from the momentum diagram in Fig. 3.3. One sees that the impulse produces a kick in $v_\perp$ such that the subsequent perpendicular velocity at resonance $v_{\perp n+1}$ is related to the previous one by

$$v_{\perp n+1} = \sqrt{v_{\perp n}^2 + \Delta v_\perp^2 + 2v_{\perp n}\Delta v_\perp\cos\chi_n}. \tag{3.40}$$

In the limit $\Delta v_\perp \ll v_\perp$ the linear kick (Eq. 3.39) is recovered. The chief advantage of using the nonlinear kick is computational: it prevents $v_\perp$ from attaining negative values ($\Delta v_\perp/v_\perp$ becomes large for small $v_\perp$); for large $v_\perp$ the nonlinear correction is small.

The kick in χ has two parts: an impulsive part which, from Fig. 3.3, is given by

$$\Delta\chi_i = \arcsin\left(\frac{\Delta v_\perp\sin\chi_n}{v_{\perp n+1}}\right), \tag{3.41}$$

and a part which is given by the advance in the relative phase between bounces,

$$\Delta\chi_b = \int_{t_n}^{t_{n+1}} dt(\omega - \omega_c(t) - k_\parallel v_\parallel(t)). \tag{3.42}$$

For a parabolic well with $k_{\|} = 0$ this is given by

$$\Delta\chi_b = \frac{1}{v_{\perp n+1}} \frac{\pi L\omega}{2} \frac{R-1}{\sqrt{R}} . \tag{3.43}$$

One then arrives at a mapping in $v_\perp$ and χ which relates the values at one resonance crossing to the values at the next resonance crossing given by Eq. 3.40 and

$$\chi_{n+1} = \chi_n + \Delta\chi_i + \Delta\chi_b. \tag{3.44}$$

Since nonrelativistic electrons receive kicks in $v_\perp$ at a constant B value, their turning points approach the resonant B location as they get heated. Because of this, it is appropriate to use the Airy function form for τ_{eff} (Case 2). Evaluating τ_{eff} for turning point-resonant electrons in a parabolic mirror, the velocity kick amplitude becomes

$$\Delta v_\perp = \frac{e\mathcal{E}_\perp}{m} \pi \mathrm{Ai}(0) v_\perp^{-2/3} \left(\frac{\omega}{L^2} \frac{R-1}{R^2} \right)^{-1/3} . \tag{3.45}$$

Fig. 3.4 shows the result of advancing this map for 100 electrons with $\mathcal{E}_\perp = 60$ V/cm which all start out with $mv_\perp^2/2 = 100$ eV and have starting χ values equally spaced between 0 and 360 degrees. One can denote two regions: 1) a low energy stochastic 'sea' where electrons cover all of phase space; 2) a higher energy region, beginning at $mv_\perp^2/2 = 12$ keV, where where electrons are trapped in small regions ('islands') of phase space, inaccessible regions arise, and diffusion is restricted. Diffusion may still take place between the islands on a fast time scale up to an energy of around 50 keV; above that energy, however, the islands cover almost 360 degrees in χ and the diffusion is severely restricted.

Chirikov (1979) developed a general method for determining the stochastic boundary of a two-parameter map such as this. Following Smith *et al.* (1980), the linear map may be written in the form

$$v_{\perp n+1} = v_{\perp n} + C(v_{\perp n}) \sin \chi_n \tag{3.46}$$

$$\chi_{n+1} = \chi_n + D(v_{\perp n+1}). \tag{3.47}$$

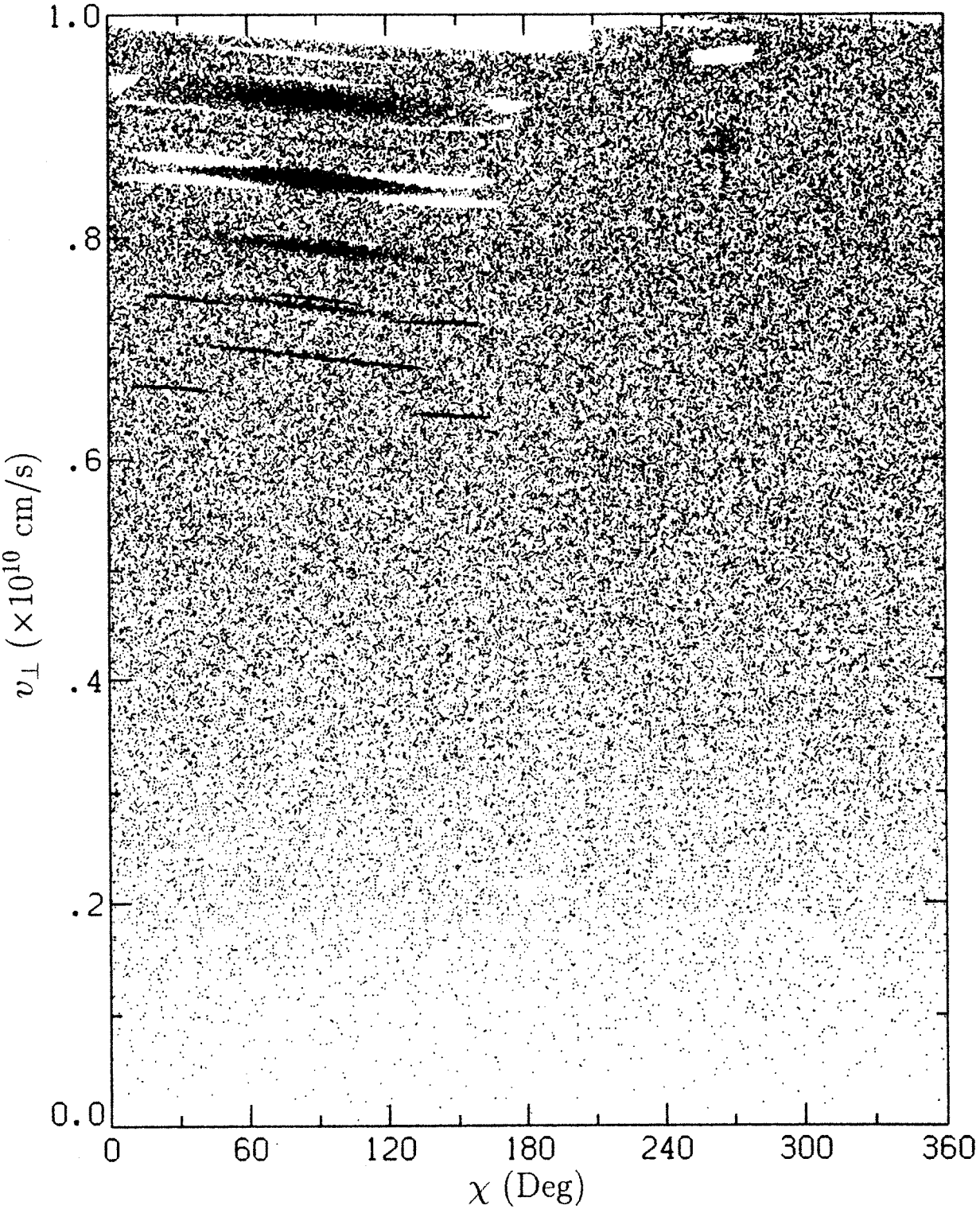

Figure 3.4: Orbits in $(v_\perp, \chi)$ coordinates for 32 electrons which start out with $mv_\perp^2/2 =$ 100 eV at resonance. Each orbit was run for 30,000 resonance crossings.

Linearizing about a velocity $v_{\perp *}$ by defining

$$\begin{aligned} I_n &\equiv (v_{\perp n} - v_{\perp *}) \frac{\partial D}{\partial v_{\perp *}} \\ K &\equiv C(v_{\perp *}) \frac{\partial D}{\partial v_{\perp *}}, \end{aligned} \tag{3.48}$$

the map can be rewritten in the 'standard' form:

$$\begin{aligned} I_{n+1} &= I_n + K \sin \chi_n \\ \chi_{n+1} &= \chi_n + I_{n+1}. \end{aligned} \tag{3.49}$$

Chirikov analyzed this map and found that motion in (I, χ) is *stable* if $|K| < 1$. For the case of turning point-resonant electrons,

$$|K| = \frac{e\mathcal{E}_\perp}{2m} \pi^2 \mathrm{Ai}(0) L^{5/3} \omega^{2/3} \frac{(R-1)^{2/3}}{R^{1/6}} v_{\perp *}^{-8/3}. \tag{3.50}$$

The stability condition $|K| < 1$ then leads to an upper limit on the perpendicular energy $mv_\perp^2/2$ at resonance for which heating is stochastic. For $L = 30$ cm, $R = 1.25$, and $\omega/2\pi = 10.5$ GHz, this energy is

$$E_{\perp s} = \mathcal{E}_\perp^{3/4} \text{ keV } (\mathcal{E}_\perp \text{ in V/cm}). \tag{3.51}$$

For a 60 V/cm electric field at resonance, this is an energy of 20 keV – much lower than the average electron energy in Constance.

At energies above $E_{\perp s}$ regions in $(v_\perp, \chi)$ space appear in which electrons begin to experience regular, small-amplitude oscillations in energy and the diffusion strength is diminished. The experiment, however, exhibits strong diffusion up to very high electron energies – clearly, something is missing in the mapping treatment outlined above. The final section of this chapter describes some of the mechanisms which allow electrons to be strongly diffused at 500 keV temperatures with the low electric field strengths present in the experiment.

3.5 Stochasticity Mechanisms

The question of stochasticity in ECRH has received a lot of attention in the last 20 years, mostly at the theoretical level (Lichtenberg and Lieberman, 1983, Rognlien, 1983b, Cohen *et al.*, 1983, Smith *et al.*, 1980, and many others), but also in connection with some experiments (Wyeth *et al.*, 1975, Turner *et al.*, 1977). In a nutshell, no experiment has clearly exhibited strong super-adiabatic effects such as a limiting of heating at energies above E_s, although weaker effects, such as the enhancement of heating with two frequencies, have been seen (Quon *et al.*, 1982).

A number of mechanisms are present in experiments that can effect the super-adiabatic boundary found in the previous section. Probably the most studied effect is that of gyrophase diffusion caused by collisions or non-conservation of μ; this will be treated in the first subsection below. Another effect is that of the electron drift motion, discussed in 3.5.2. Multiple resonances can raise the stochastic boundary somewhat, and this is discussed in 3.5.3. Finally, the rf field at resonance may have randomness associated with it, due to wall reflections, variations in ray trajectories due to density fluctuations, and, of course, micro-instability; this is discussed in 3.5.4.

3.5.1 Gyrophase Diffusion

The effect that pitch angle collisions have on ECRH arises from a two-fold process: an electron suffers a collision which changes its midplane pitch angle, which, in turn, changes its bounce period so that the change in χ between resonance crossings $\Delta\chi_b$ (Eq. 3.43) is altered. Cohen *et al.* (1983) found that there is an important cumulative effect over many bounces. This is simply because a collision at an early time changes τ_b for all subsequent times, and there is therefore a contribution to $\Delta\chi$ that is linear in time. In addition, additional collisions occur at a rate which is proportional to $t^{1/2}$. The total effect over many bounces then has a $t^{3/2}$ dependence. The result for a parabolic mirror field is

$$\langle(\Delta\phi)^2\rangle = \frac{1}{24}\left(\frac{1}{\sin\theta} - 1\right)\left(1 - \frac{3}{\sin^2\theta}\right)^2 \nu_e \omega_{c0}^2 t^3, \tag{3.52}$$

where ν_e is the collison rate. Choosing $\theta = 63°$ for resonant electrons in Constance with $B_0 = 3.0$ kG, Eq. 3.52 may be written in the 'handy-dandy' form

$$\langle(\Delta\phi)^2\rangle = 3.5\frac{n}{E^3}\left(\frac{t}{\tau_b}\right)^3, \tag{3.53}$$

where the density n is in cm^{-3} and E is in eV.

Rognlien (1983b) investigated the effects of gyrophase diffusion and found that it ensures stochastic rf diffusion if $\langle(\Delta\phi)^2\rangle > 1/l$ in a time $\tau_b/2$. This corresponds to an energy of 6 keV for $l = 1$ with $n = 5 \times 10^{11}\mathrm{cm}^{-3}$, an energy which is well inside the intrinsically stochastic range $E < E_s$ for electric fields typical of the experiment. This does not mean that collisions have no effect at higher energies; on the contrary, they insure that diffusion takes place, but on a slower time scale. For a 50 keV electron ϕ will be randomized according to the above criterion in 4 bounce periods. This means that D^{rf} will be reduced by roughly a factor of 8, since the correlation time Δt is about $8\tau_b/2$. One observable consequence of this would be a decrease in the heating rate as the electron temperature rises above E_s.

Another form of gyrophase diffusion arises from pitch angle changes due to non-conservation of μ. Ignoring geometrical factors of order unity, the change in θ in a bounce time (Chirikov, 1979, Cohen *et al.*, 1978a) is roughly

$$\Delta\theta \sim \frac{L}{\rho}e^{-L/\rho}. \tag{3.54}$$

For the case of Constance, this effect is comparable to collisions only when ρ/L becomes larger than 1/10, corresponding to an energy of around 2 MeV, well above the range of interest. For relevant energies, non-conservation of μ is small compared to collisions.

3.5.2 Drift Motion

Until now, I have assumed that each resonance crossing is at the same spatial position. The electron drift motion, however, causes the electron to be on a different field line at each resonance, and this produces an rf phase shift of

$$\Delta\chi_d = \mathbf{k} \cdot \mathbf{V} \Delta t, \tag{3.55}$$

where $\mathbf{V}$ is the guiding-center drift velocity. On first glance, this term seems to be important – $\Delta\chi_d$ can be an appreciable fraction of 2π on a bounce time. However, if one includes Eq. 3.55 in the mapping equations for the simple situation of an electron drifting in the direction of $\mathbf{k}$, one finds that the scale length of B must be on the order of a gyroradius to have an effect on E_s! The effect is small because the change in χ due to drifts is not random, but varies in an even less sensitive manner than the change due to the bounce motion. Smith *et al.* (1980) also found that the effect of drifts is negligibly small in the case of ion heating; in fact, the effect turns out to be independent of mass.

The Constance geometry is much more complicated than the simple slab model that was used to arrive at the result above. However, the effect is so small in the simple model that it seems doubtful that it is significant in the experiment.

3.5.3 Multiple Resonances

It was observed in the SM-1 experiment (Quon *et al.*, 1982) that two-frequency ECRH, with $\Delta\omega/\omega \sim 0.5\%$, produced three times higher hot electron diamagnetism than single-frequency ECRH at the same total power. Since the hot electron temperature was the same in both cases (370 keV), it seems that the enhancement was due to heating of the source electrons; in other words, ν_{c-h} was three times higher with two-frequency rf. This result has been analyzed on the theoretical side by a number of people (Rognlien, 1983b, Lichtenberg *et al.*, 1986), and they concluded that the stochastic barrier E_s can be raised by a factor of two or so if $\Delta\omega$ is on the order of the bounce frequency. The reason that such a frequency separation is desirable is that it spans neighboring bounce resonances and prevents the electron from becoming super-adiabatically trapped in a single bounce

resonance. The interpretation of the experimental result, then, is that the hot electron diffusion was unaffected, but that the source for the hot electrons was enhanced by stronger low energy heating due to the larger E_s value.

The experimental results presented here were obtained with single-frequency heating. This doesn't mean, however, that multiple-resonance effects are not present, because high energy electrons can experience resonance with more than one l value. In addition, spatially separate resonances can arise for a single l value with nonzero $k_{\|}$; the effect that this has on D has been studied by Rognlien (1983b). The bottom line, however, is that multiple resonances are not expected to have a large effect on the diffusion of hot electrons.

3.5.4 rf Incoherence

The mapping approach assumes that the rf wave phase at time t is equal to ωt; that is, that it is completely determined for all time from the moment the transmitter is turned on. This, of course, is unrealistic: any rf source has some bandwidth, and this will lead to phase incoherence over some time τ_c, which is fairly long (~ 1 μs) in the case of the Constance transmitter. Other mechanisms exist, however, which can add incoherence to the rf wave: wall reflections, which produce cavity fields, and density fluctuations are two examples that I will consider. In steady-state, of course, for many conditions, the plasma emits a broad spectrum of microinstability emission which can reach significant power levels. This emission is included in the measurement of cavity rf power.

Wall reflections produce incoherence because two waves that reach the same point along optical paths differing in length by Δx arrive with a phase difference $k\Delta x$. For $f = 10.5$ GHz, this says that waves following optical paths only 1/2 cm apart will have a phase difference of 1 radian. It is therefore clear that cavity fields, which are measured to have a strength of around 10 V/cm in the cavity experiments, are effectively incoherent and will produce stochastic heating. Power in these fields is not large enough to account for the heating seen in the experiments, but these fields can act as a randomizing agent to reduce super-adiabatic effects on the direct field diffusion.

An estimate of this effect can be made if one assumes that a kick in $v_\perp$ from a cavity field has a similar effect on ϕ as a collisional scattering event (the direct change in ϕ from a cavity field interaction is very small). The relative kick in a half bounce time from collisions is given by

$$\left(\frac{\Delta v_\perp}{v_\perp}\right)_{coll} \sim \frac{\pi}{4}\left(\frac{\tau_b}{2\tau_{90}}\right)^{1/2}, \tag{3.56}$$

and the relative kick from a cavity field of strength $\mathcal{E}_{cav}$ is given by

$$\left(\frac{\Delta v_\perp}{v_\perp}\right)_{cav} \sim \frac{e\mathcal{E}_{cav}}{m}\tau_{eff}. \tag{3.57}$$

For $mv_\perp^2/2 = 30$ keV and $\mathcal{E}_{cav} = 10$ V/cm these two effects have the same magnitude, and cavity fields are therefore expected to have a randomizing effect of the same strength as collisions. Furthermore, the ratio of the two scales very weakly with energy ($\sim E^{1/6}$).

Density fluctuations produce variations in the wave phase at a point in the plasma due to the fact that the index of refraction depends on the line integrated density along the path; this is the principle of the microwave interferometer. One can get an estimate of this effect by looking at the unmagnetized plasma index of refraction, for which the phase change due to the plasma is given by

$$\Delta\psi = \frac{3.18 \times 10^9}{2\omega c}\int ndl. \tag{3.58}$$

The interferometer signal indicates that a fluctuation level of $\Delta nl \sim 4 \times 10^{11}$ cm^{-2} exists in the plasma, for which the expected phase change is on the order of 0.3 radians — probably not enough to induce stochasticity even if the fluctuations are as fast as the electron bounce frequency ($\sim$ 100 MHz) (no fluctuation data has been taken with the required high frequency response).

None of the randomizing mechanisms mentioned in this section is clearly strong enough to fully randomize the wave/particle interaction up to 500 keV energies, but all are present in the experiment, and more careful analysis may reveal that one or more is sufficient. The results presented in the next chapter give no clear indication that super-adiabaticity reduces diffusion in the experiment.

3.6 Summary

Much more detail is available to the theorist than is available to the experimentalist — in an experiment, one can measure diffusion only by measuring a current and a gradient, and inferring the diffusion strength. In the Constance experiment there are five main measurements that can be made: 1) rf detectors can give an indication of the electric field E in the plasma, 2) endloss detectors measure the endloss current distribution dJ/dE, 3) x-ray spectra are a measure of the pitch-angle averaged distribution function, and give a characteristic temperature T_h, 4) interferometer and diamagnetic measurements determine the line density and stored energy in the plasma, and 5) imaging diagnostics such as the CCD camera reveal the spatial structure of electron production. One cannot directly measure the absorbed power P_{abs} or the hot electron source rate $\nu_{c\to h}$ and loss rates ν_p and ν_h. These must be inferred from the other measurements. Nevertheless, the experiment offers a rich variety of behavior, and it will be apparent from the measurements what roles collisons, applied rf, and micro-instability rf play in the velocity-space diffusion of electrons in Constance.

Chapter 4

Experimental Results

The experiments reported in this work are aimed at determining the factors that play a role in the velocity-space diffusion equation,

$$\frac{\partial f}{\partial t} = \nabla \cdot \mathsf{D} \cdot \nabla f + S(\mathbf{p}), \tag{4.1}$$

and evaluating their overall effect on hot electron heating and confinement. However, in this, as in any experiment, one cannot directly measure the source function $S(\mathbf{p})$, the diffusion tensor D, or even the distribution function $f(\mathbf{p})$. Instead, one can only measure a variety of moments of $f(\mathbf{p})$, some of which also incorporate a spatial integral. The main diagnostics which have been used are described in Chapter 2; however, it is worthwhile noting exactly how each diagnostic relates to Eq. 4.1. This discussion is given in Section 4.1. Section 4.2 describes how the plasma may be controlled. Section 4.3 discusses the particle and power balance equations, and identifies the terms which can be measured and how they relate to the diffusion equation. The source term is discussed in Section 4.4, where cold electron heating is analyzed.

Finally, the main results of this work are presented in Sections 4.5 and 4.6. The former contains the results which bear on the diffusion tensor D, and the latter uses these and other results to understand the heating and confinement of hot electrons in Constance.

4.1 Diagnostics

The most important diagnostics in this thesis are hard x-ray spectroscopy, scintillator probes, the microwave interferometer, diamagnetic loop, and rf detectors. With the exception of rf detectors, all of these diagnostics can be related to the distribution function f.

The moment of f which gives the x-ray spectra is quite complicated due to the complexity of the relativistic x-ray cross-section; it is shown in Appendix A. However, to a fair degree of accuracy, the x-ray *intensity* spectrum reflects the pitch-angle integrated distribution function in energy, although greatly smoothed-out by the x-ray integral. Thus, x-ray spectra are sensitive only to the average energy dependence of f and not to detail. I generally use the hard x-ray spectra to measure the hot electron temperature, and sometimes to determine the deviation of f from a Maxwellian. When considering x-ray spectra one must also remember that the spectrum is a sum of all of the emission across the viewing chord; for this reason, the derived temperature may suddenly change if the x-ray target profile suddenly changes across the chord. This often occurs when the applied rf is turned off: the cold electrons and the ions which match their density suddenly leave, the impurity profile may change, and generally the derived temperature rises. Fig. 4.1 displays an experimental x-ray spectrum and the theoretical fit using the detector response algorithm described in Appendix A. The data is best fit to a spectrum for a 'mirror' distribution $f(E) = p^s \exp(-E/T)$. The best-fit Maxwellian has a temperature of 450 keV. I use the temperature derived from a Maxwellian fit throughout this dissertation, both because it is a more familiar parameterization of the distribution function, and because a single-parameter fit considerably speeds up the analysis.

The moment of f that gives the hot electron endloss, which is measured with a scintillator probe, is derived in Chapter 2, and is basically the integral along the loss-cone boundary of the velocity space flux

$$\Gamma = -\mathsf{D} \cdot \nabla f. \tag{4.2}$$

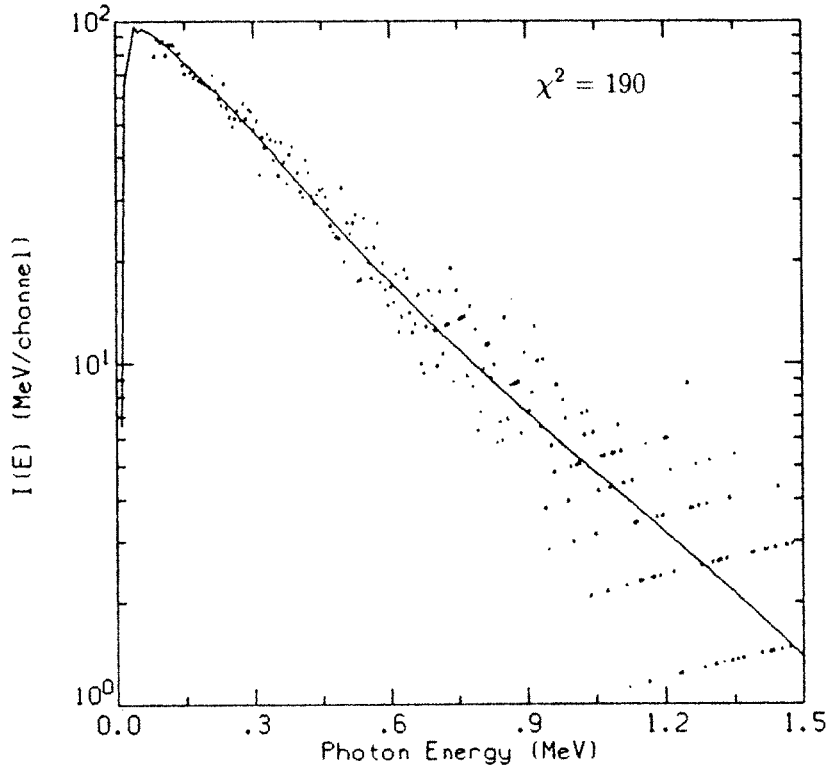

Figure 4.1: An x-ray spectrum taken in the first 50 ms following the rf turnoff. The curve is the calculated spectrum for a mirror distribution with $s = 2$ and $T = 290$ keV.

Endloss is therefore sensitive to both the diffusion tensor D and the gradient of f at the loss-cone boundary; it is insensitive to the bulk properties of f. The x-ray measurements and the hot electron endloss measurements, therefore, play complementary roles. In fact, endloss is the closest one can get to directly measuring a velocity-space current. Furthermore, the scintillator probe has a very small opening and intersects a very small flux tube; it very closely approximates a measurement of endloss on a single field line, a feature which adds simplicity to the analysis since the diffusion paths in velocity-space are field line-dependent.

The microwave interferometer measures a line-integrated density, given by the zeroth moment of f. It has a dependence on T_h, however, due to the fact that hot electrons have a larger effective mass which reduces their contribution to the plasma frequency by an amount $\langle 1/\gamma \rangle$. The microwave interferometer is used to measure the cold electron line density $n_c l$ and, by using the T_h value derived from the x-ray spectra to evaluate the relativistic correction, the hot electron line density $n_h l$. The method is shown in Fig. 4.2: the decay of the total nl after the rf is turned off is extrapolated back to the rf turnoff time; this uncorrected nl value is then corrected using T_h to give $n_h l$, and the difference between the extrapolated nl value and the value before rf turnoff is $n_c l$.

The diamagnetic loop measures the integrated magnetic flux which passes through it due to diamagnetic currents resulting from pressure balance perpendicular to the magnetic field. It is complicated due to the fact that the mutual inductance between plasma currents and the loop has a strong geometric dependence. The plasma pressure profile and loop response is the subject of Xing Chen's thesis work, and I will use his results to determine the perpendicular stored energy $W_\perp$ in the plasma from the integrated loop voltage. The standard case with $B_0 = 3.0$ kG has a conversion of $W_\perp = 2.4 V_{loop}$, where $W_\perp$ is in Joules and V_{loop} is in Volts.

The rf detectors are quite simple: the rf power entering a waveguide is measured by a diode. The maximum level of microinstability rf (MRF) seen in the experiment is 200 mW in the waveguide.

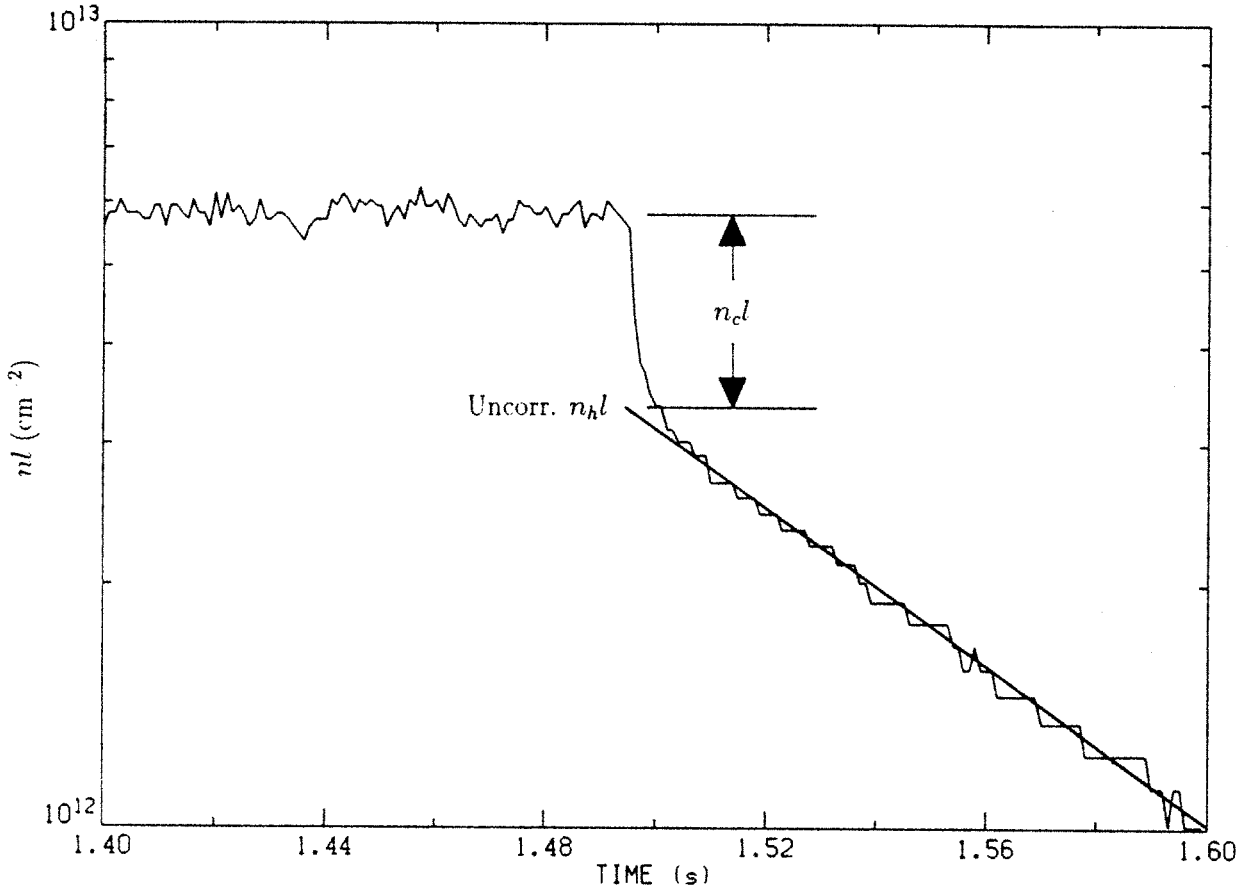

Figure 4.2: The technique used to measure $n_c l$ and $n_h l$. In this case, $n_c l = 2.6 \times 10^{12}$ cm^{-2} and $n_h l = 6.3 \times 10^{12}$ cm^{-2} with $T_h = 310$ keV.

4.2 Control of Plasma Parameters

The experimentalist has very few 'knobs' to vary in controlling the plasma in a simple experiment like Constance. There are three main ones: applied rf power, magnetic field strength, and neutral gas pressure. The mirror ratio is inherent in the fixed baseball magnet and cannot be varied.

The applied rf power is launched in either X- or O-mode orientation. For the cavity measurements, O-mode launch was used (for historical reasons), but there is a significant level of unpolarized cavity fields present (around 8 V/cm as compared to direct fields of around 60 V/cm for $P_{rf} = 2$ kW). In the absorber experiments the cavity fields are reduced (to around 3 V/cm for $P_{rf} = 2$ kW), and both X- and O-mode launches were used, although X-mode was used more extensively since it produces much better heating in most parameter regimes. Both cavity and absorber configurations have MRF present in the appropriate regimes. The rf power is generally varied from 1 to 5 kW, although higher powers have been used on a limited basis (waveguide arcs begin to be a problem above 5 kW).

The midplane magnetic field may be varied from 1.9 kG, when the fundamental nonrelativistic resonance is at the mirror peak on the central field line, to 3.75 kG, when it is at the midplane on the central field line. The absorber experiments are restricted to fields at and above 3.0 kG, which is the standard field for the bulk of the data; lower fields produced a large amount of outgassing from the absorber due to plasma striking it inside the center chamber of the machine. The cavity experiments have run the full range of fields. For the standard case of 3.0 kG the plasma has a diameter of about 20 cm and a length of about 30 cm.

The hydrogen gas pressure is measured by an ionization gauge on a tube connected to the center chamber, and can be varied from around 2×10^{-7} Torr, where the gas barely breaks down, to the 10^{-4} Torr range where the gas is weakly ionized and no hot electrons are produced. The experiments presented here are limited to pressures below 5×10^{-5} Torr, and mostly lie in the 5×10^{-7}–2×10^{-6} Torr range. The effect that varying gas

pressure has on the plasma is not obvious, but extremely important. In fact, gas pressure is generally the *most sensitive* 'knob' on the experiment. The next section will describe the effect that gas pressure (or neutral density) has in a very simple model.

4.3 Particle and Power Balance Equations

In the course of describing the experimental results, I will often refer to the cold and hot electron power balance equations. The division of the electrons into cold and hot components is natural, because the two components have different confinement mechanisms: electrostatic confinement due to the ambipolar potential for cold electrons (Pastukhov, 1974, Cohen *et al.*, 1978b), and magnetic confinement for the hot electrons. The connection region in energy is the warm electron region, a low-density, strongly rf-driven portion of the distribution that is whistler unstable (Garner 1986, Garner *et al.*, 1987) in strong heating regimes. Since the warm electrons do not comprise appreciable density, as I will show later, I will not separate them into a third component, but, will consider them to be an anisotropic rf-driven tail on the cold population. Fig. 4.3 represents a model distribution function consisting of a 100 eV cold Maxwellian component with a 1 keV warm tail, and a 400 keV hot electron component.

Given the two-component breakdown of the electrons, the particle balance equations may be written:

$$\frac{dn_c}{dt} = n_0 n_e \langle \sigma v \rangle - n_c \nu_{pc} - n_c \nu_{c \to h} \tag{4.3}$$

$$\frac{dn_h}{dt} = n_c \nu_{c \to h} - n_h \nu_{ph}, \tag{4.4}$$

where $\langle \sigma v \rangle$ is the average ionization rate for cold and hot electron impact ionization of molecular hydrogen with density n_0,

$$\langle \sigma v \rangle = \frac{n_c}{n_e} \langle \sigma v_c \rangle + \frac{n_h}{n_e} \langle \sigma v_h \rangle. \tag{4.5}$$

The hot electron source rate $\nu_{c \to h}$ represents the diffusion of cold electrons up to high energies and is a loss term for the colds; however, $\nu_{c \to h} \ll \nu_{pc}$ and this loss is negligible

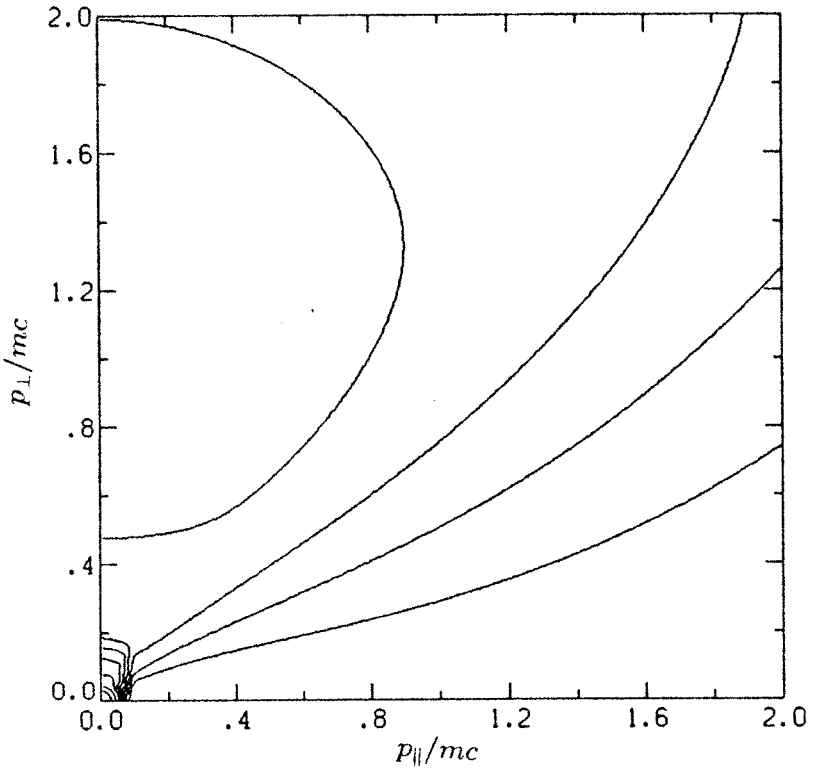

Figure 4.3: Contours of a model electron distribution function for Constance.

compared to endloss. This does *not* mean that the cold electrons are not strongly rf-diffused, it only means that a small fraction of them make it up to the 100 keV energies characteristic of the hot population. In fact, in strong heating regimes the cold electrons are strongly diffused, but they are rapidly cooled along rf characteristics and diffused into the loss cone in the warm tail region due to the microinstability. Since the cold electrons are at essentially zero energy compared to the hots, the source term $S(\mathbf{p})$ in Eq. 4.1 may be written

$$S(\mathbf{p}) = n_c \nu_{c\to h} \delta^3(p). \tag{4.6}$$

This is a simple formulation which insures that the particle and power balance equations for the hots are recovered by taking moments of Eq. 4.1.

The power balance equations for the two components are:

$$\frac{d}{dt}\frac{3}{2} n_c T_c = \mathcal{P}^c_{abs} + Q_{hc} - n_0 n_c \langle \sigma v_c \rangle 25.9 \text{ eV} - \frac{3}{2} n_c T_c \nu_{Ec} - \mathcal{P}_\mu \tag{4.7}$$

$$\frac{dW}{dt} = \mathcal{P}^h_{abs} - Q_{hc} - n_0 n_h \langle \sigma v_h \rangle 25.9 \text{ eV} - W \nu_{Eh}. \tag{4.8}$$

The drag heating Q_{hc} and ionization loss terms can be significant for the colds, since in weak heating regimes they absorb little rf power ($\mathcal{P}^c_{abs} \ll \mathcal{P}^h_{abs}$); both are negligible for the hots and will be ignored from now on. The power loss due to MRF is represented by $\mathcal{P}_\mu$ and is associated with the cold electron power balance according to my practice of lumping the cold population and the warm tail together; the MRF-induced endloss is included in the endloss rates.

In the absence of microinstability, the cold electron endloss rates are given by the Pastukhov formulae for loss of Maxwellian electrons in a mirror with a confining potential ϕ:

$$\nu_{pc} = \nu_0 \frac{2}{\sqrt{\pi}} \frac{2R}{(2R+1)\ln(4R+2)} \exp(-\phi/T) \frac{T}{\phi} \int_0^\infty e^{-\xi} \sqrt{1+\frac{T\xi}{\phi}} d\xi \qquad (4.9)$$

$$\nu_{Ec} = \nu_0 \frac{2}{\sqrt{\pi}} \frac{2R}{(2R+1)\ln(4R+2)} \exp(-\phi/T) \left[\frac{2}{3} + \frac{T}{\phi} \int_0^\infty e^{-\xi} \sqrt{1+\frac{T\xi}{\phi}} d\xi\right], \qquad (4.10)$$

where ν_0 is the collisional scattering rate, given for cold-cold collisions by

$$\nu_0 = 3.9 \times 10^{-6} n_c T_c^{3/2} \lambda_{cc}. \qquad (4.11)$$

Here n_c is in cm^{-3} and T_c is in eV. In the future, I will abbreviate Eqs. 4.9 and 4.10 with the notation

$$\nu_{pc} = \nu_0 \Pi_p(\phi/T_c)$$
$$\nu_{Ec} = \nu_0 \Pi_E(\phi/T_c).$$

The microinstability, of course, results in loss at keV energies which is not describable by the Pastukhov formulae; however, a large fraction (over 50%) of the particle loss occurs at low energies ($E < 200$ eV) for which electrostatic confinement applies.

It is very difficult to write expressions for the cold and hot endloss rates, as well as the hot electron source rate $\nu_{c\to h}$, due to the complexity of the microinstability and rf diffusion and the non-Maxwellian character of the electron distribution function. However, an investigation of an idealized situation, that of a strictly cold electron plasma confined by

the electrostatic potential, gives insight into the variation of the cold component with applied power, gas pressure, and magnetic field. This description is pursued in the next section, in which the role of the cold electrons as the source function for the hots is discussed.

4.4 Cold Electron Heating

The dependence of cold electron density and temperature on applied power and gas pressure can be roughly determined by retaining the dominant terms in the particle and power balance equations. Antonsen and Manheimer (1978) derived expressions for the absorption of a Maxwellian plasma with perpendicular rf launch. The transmission coefficient for X-mode launch, in the limit of low parallel wavenumber ($N_\parallel \ll 1$) and low density ($\omega_p \ll \omega_c$) is

$$\Gamma_X = 1.8 \times 10^{-6} L_\perp f T N_\parallel^2 \frac{\omega_c^2}{\omega_p^2}, \tag{4.12}$$

where the perpendicular magnetic scale length $L_\perp$ is in cm, f is in GHz, and T is in eV. The absorption is then given by

$$\mathcal{P}_{abs}^c = \mathcal{P}_{rf}\left(1 - e^{-\Gamma_X}\right). \tag{4.13}$$

Since $\Gamma_X \ll 1$ for cold electrons, due to the low T_c, $\mathcal{P}_{abs}^c$ is given simply by $\mathcal{P}_{rf}\Gamma_X$. Using this for $\mathcal{P}_{abs}^c$, and retaining only ionization source and endloss, Eqs. 4.3 and 4.7 become

$$n_c^2 T_c^{-3/2} \Pi_p(\phi/T_c) \;\propto\; n_c n_0 \langle \sigma v_c \rangle \tag{4.14}$$

$$n_c^2 T_c^{-1/2} \Pi_E(\phi/T_c) \;\propto\; \mathcal{P}_{rf} \frac{T_c}{n_c}. \tag{4.15}$$

The dependence of n_c and T_c on $\mathcal{P}_{rf}$ and n_0 may be found by combining the two equations, giving the expected scalings

$$n_c \;\propto\; \sqrt{\frac{\mathcal{P}_{rf}}{n_0 \langle \sigma v_c \rangle}} \tag{4.16}$$

$$T_c \;\propto\; \left(\frac{\mathcal{P}_{rf}}{\Pi_E}\right)^{1/3} \frac{\Pi_p}{n_0 \langle \sigma v_c \rangle}. \tag{4.17}$$

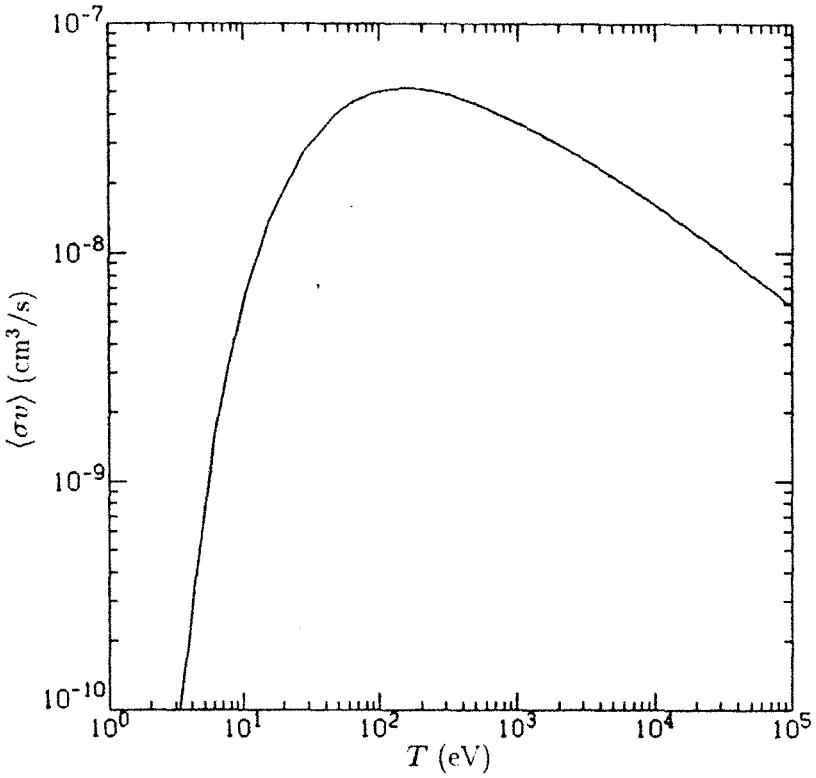

Figure 4.4: The rate for electron impact ionization of molecular hydrogen, averaged over a Maxwellian distribution of temperature T. From Janev RK, Langer WD, Evans K Jr., and Post DE, Princeton Plasma Physics Lab report PPPL-TM-368 (1985).

There is still an implicit T_c-dependence in $\langle\sigma v_c\rangle$; however, $\langle\sigma v_c\rangle$ (shown in Fig. 4.4) is fairly flat around 100 eV, which is the estimated[1] value of T_c at low gas pressure. Furthermore, T_c has a weak dependence on $\mathcal{P}_{rf}$. If the ratio ϕ/T_c does not vary much in a power scan at low pressure, one would expect a density scaling $n_c l \propto \sqrt{\mathcal{P}_{rf}}$. Fig. 4.5 indicates that this is indeed the case in the experiment.

The dependences on gas pressure are somewhat more complicated. Eq. 4.17 indicates that $T_c\langle\sigma v_c\rangle$ has an inverse dependence on n_0, for fixed $\mathcal{P}_{rf}$ and ϕ/T_c. Since $\langle\sigma v_c\rangle$ falls rapidly with decreasing T_e for $T_c < 100$ eV, the density dependence is not clear. In fact, the data shown in Fig. 4.6 indicates that the variation of T_c and ϕ/T_c overpower the factor of $n_0^{-1/2}$ in Eq. 4.16, and cold electron density *increases* with pressure for X-mode launch. This, combined with the fact that ϕ is observed to decrease with gas pressure,

[1]There is no diagnostic on Constance which determines T_c in the confining region, although it may be measured with Langmuir probes on the outside or inferred from ELA measurements.

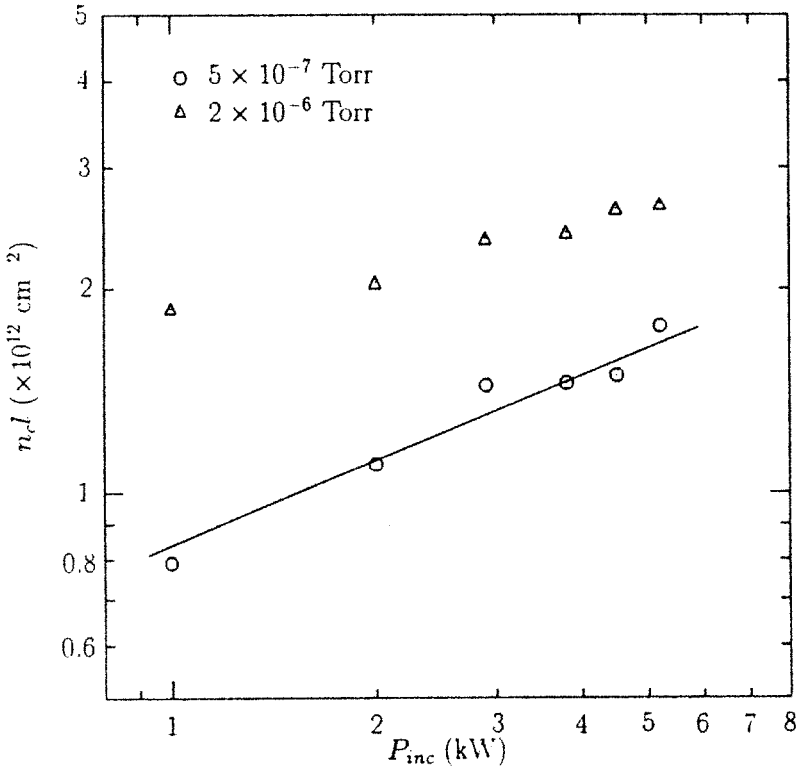

Figure 4.5: Cold electron line density vs. applied power in scans with X-mode launch and absorber. $B_0 = 3.0$ kG.

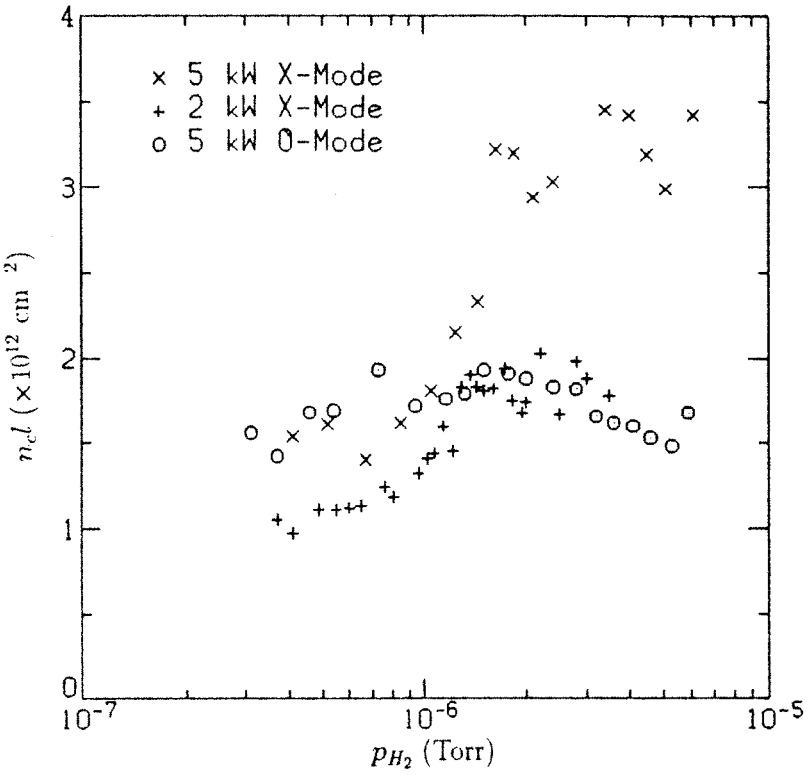

Figure 4.6: Cold electron line density vs. gas pressure in scans with microwave absorber. $B_0 = 3.0$ kG.

implies that T_c *strongly decreases* with increasing gas pressure, a result that has very important ramifications for the microinstability and hot electron fueling.

The X-mode absorption rate for a distribution of turning-point resonant electrons, which is an idealized model for the strongly-driven warm tail, was calculated in Chapter 3 (Eq. 3.34). One of the main features of that result is the fact that the absorption exhibits a dependence on the mirror ratio R at resonance: $\mathcal{P}^c_{abs} \propto (R-1)^{-2/3}$. This occurs simply because a turning-point resonant electron spends more time in resonance (τ_{eff} increases) as the resonance moves towards the mirror minimum. It is exactly this effect that results in strong heating along the 'baseball seam' traced out by the intersection of the resonant B surface and the outermost nonrelativistically resonant drift surface shown in Fig. 2.6 in Chapter 2. The slab model which was used to obtain Eq. 4.12 ignores the effects of the variation of B along a field line that result in the R-dependence noted above, and only takes into account the variation of B perpendicular to a field line to account for the time that the rf wave spends in the resonance zone as it transverses the plasma along an oblique ray path. This type of treatment is inadequate for an understanding of the spatial dependence of absorbed power in the Constance geometry: the perpendicular scale length of B varies little on the resonant B surface, and the slab model therefore would predict fairly uniform absorption on the egg-shaped resonant B surface. In fact, this errant outlook was prevalent in the Constance group for years, and wasn't changed until video camera pictures revealed the baseball-seam shape of the plasma. This is a striking example of a situation where rf diffusion has radical consequences which are outside the scope of commonly-used heating models.

The above considerations give insight into the B_0-dependence of cold electron heating: as B_0 is increased, the baseball-seam plasma shrinks and finally vanishes at $B_0 = 3.75$ kG. Fig. 4.7 shows that the line density actually increases with B_0 for X-mode launch up to very high fields. Since the power density $\mathcal{P}_{rf}$ scales as $1/r^3$ for a characteristic radius of the plasma r, and line density is expected to follow the scaling $n_e l \propto r\sqrt{\mathcal{P}_{rf}}$, one would expect $n_e l$ to scale as $r^{-1/2}$ in a magnetic field scan, a factor of 2 increase from $B_0 = 3.0$ kG to $B_0 = 3.6$ kG. The data is in reasonable agreement with this rough estimate.

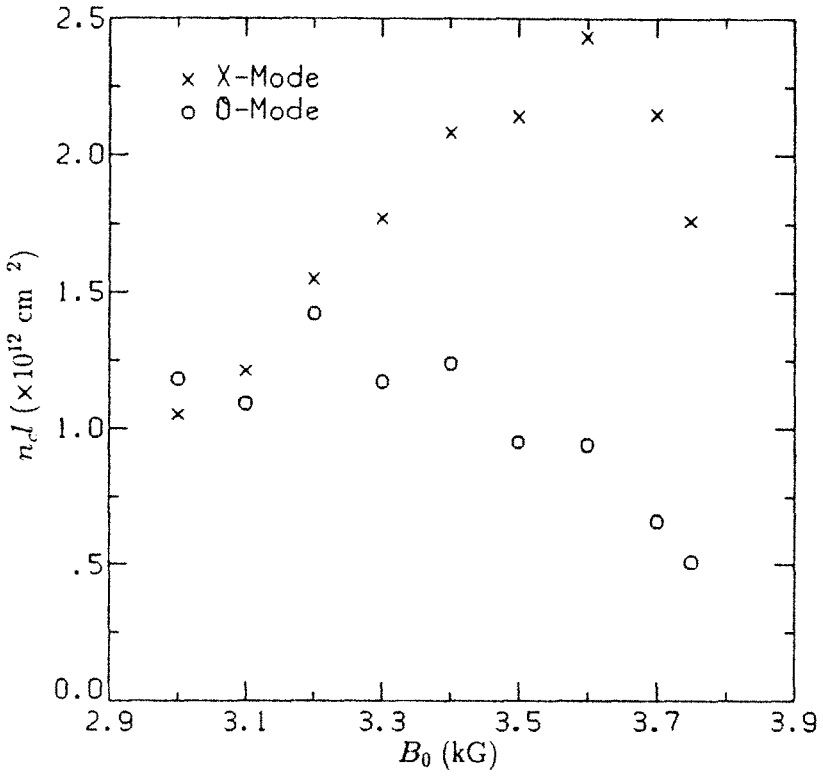

Figure 4.7: Line density vs. magnetic field in a scan in which applied power and gas pressure are held constant ($P_{rf} = 2$ kW, $p_{H_2} = 5 \times 10^{-7}$ Torr).

Up to this point, I have restricted the discussion to plasmas heated by X-mode launch. O-mode absorption is much lower for cold electrons, due to the low value of $J_1(k_\perp \rho)$ at these energies. The slab model formula (Antonsen and Manheimer, 1978) for O-mode transmission is, in the low-density, low-$N_\parallel$ limit,

$$\Gamma_O = 6.4 \times 10^{-7} L_\perp f T \frac{\omega_p^2}{\omega_c^2}. \tag{4.18}$$

For typical Constance cold electron parameters, O-mode absorption is less than one-tenth of X-mode absorption. This means that if 10% of the power is in the X-mode polarization at resonance, it will heat more than the remaining 90% O-mode component. An examination of the field-line plot and rf ray trajectories (Fig. 2.2 in Chapter 2) indicates that up to 20% of the power reaches resonance in the X-mode polarization for $B_0 = 3.0$ kG due to the bending of field lines. This should be contrasted with the $B_0 = 3.6$ kG case, in which less than 4% is in X-mode component. One then expects that the heating will decrease in a magnetic field scan with O-mode launch if residual X-mode provides the main heating. The data shown in Fig. 4.7 bears this out, where $n_c l$ is seen to fall as B_0 increases above 3.2 kG for O-mode launch. The $n_c l$ values in a pressure scan with O-mode launch (Fig. 4.6) are similar to values obtained in an X-mode scan at lower power, lending further support to the conclusion that O-mode launch heats cold electrons primarily by means of partial X-mode polarization at resonance.

In conclusion, the experimental results for cold electron heating are in reasonable agreement with the standard X-mode heating model as regards the scaling of cold electron density with rf power, gas pressure, and magnetic field, with the exception that the spatial deposition exhibits a more detailed structure resulting from the effect of mirror geometry on the rf diffusion strength.

The cold electron heating results summarized in this section are important for hot electron heating in three ways: 1) the cold electron density affects ray propagation and absorption due to its contribution to ω_p^2, 2) the strength of cold electron heating determines the strength of MRF, and, most importantly, 3) the strength of cold electron

heating determines the source rate $\nu_{c\to h}$ for the hot electrons. Many of the results for hot electron heating and confinement, presented in the rest of this chapter, will therefore be intimately connected with the results presented in this section.

4.5 The Diffusion Tensor

It is now time to see what can be determined from the experiment concerning the factors that enter into the velocity-space diffusion tensor. I have chosen to break these factors into six categories: collisions (4.5.1), electric field strength and frequency (4.5.3), loss of adiabaticity (4.5.2), super-adiabaticity (4.5.4), diffusion paths(4.5.5), and the effect of the cavity electric fields (4.5.6). The results presented on these topics are the main results of this work, as they concern the general properties of ECH velocity-space diffusion. The results on heating and confinement presented in the final section of this chapter should be looked upon as the manifestation in Constance of the results presented in this section, which are of much more general importance. The ramifications for other devices will be discussed in Chapter 5.

4.5.1 Collisions

Before presenting results concerning the more complicated problem of rf diffusion, it is worthwhile to first examine whether the collisional processes in the experiment are well-described by the standard model presented in Section 3.2. This is useful for two reasons: 1) it tests a theory which is commonly accepted yet still not well-studied in experiments, and 2) it establishes and tests the methods used in the study of the rf diffusion problem.

The bulk measure of collisionality is the decay of the diamagnetic loop, x-ray, and interferometer signals in the afterglow after the rf is shut off, combined with the local measure of endloss power with the scintillator probe. These signals are shown in Fig. 4.8. The hot endloss *spectrum* gives more detailed information which can be used to help interpret the bulk measurements.

The first thing to notice is that the interferometer signal decays much more quickly than the diamagnetic loop. This is to be expected: lower energy electrons scatter more

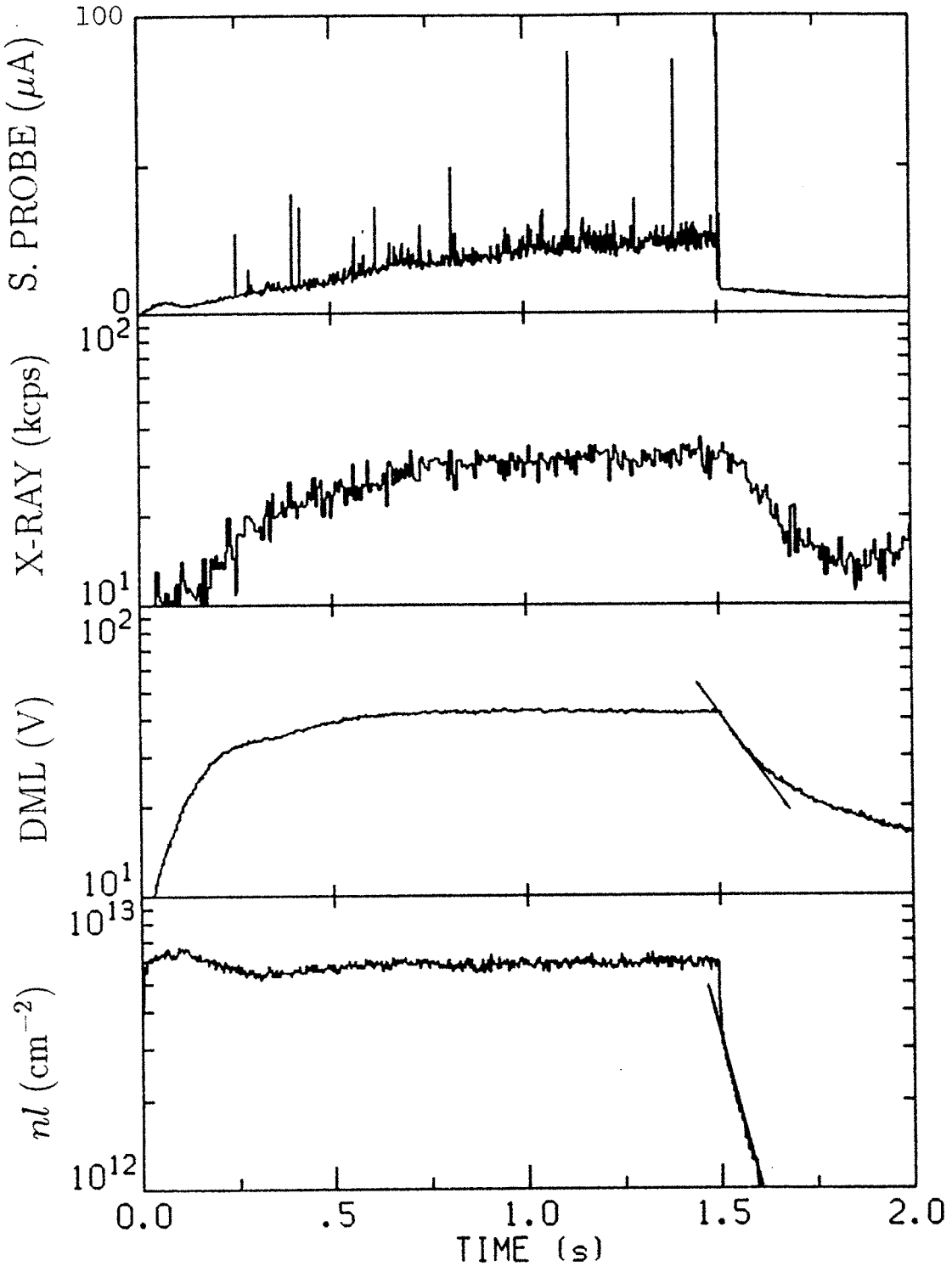

Figure 4.8: Interferometer, diamagnetic loop, x-ray, and scintillator probe signals for a shot in which the rf is turned off at $t = 1.5$ s. The measured decay times are 88 ms for the interferometer and 220 ms for the diamagnetic loop.

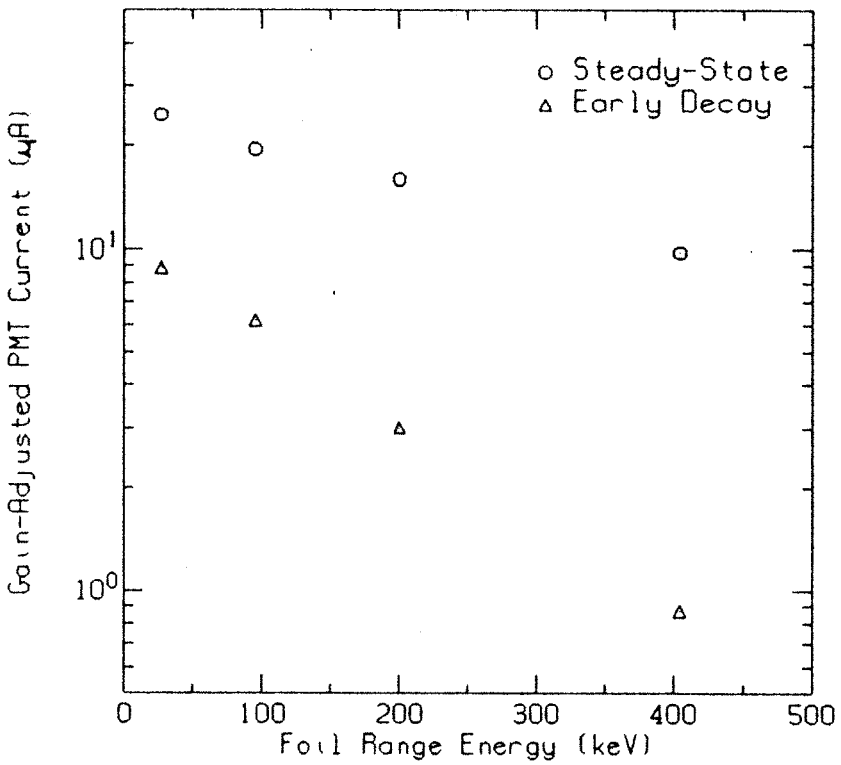

Figure 4.9: The endloss power spectrum during the steady-state and collisonal decay as measured by the scintillator probe. The inverse slope of the steady-state spectrum has a value of 420 keV, as opposed to 160 keV for the decay spectrum.

quickly than higher energy electrons, and contribute less to $W_\perp$ but *more* to ω_p^2 due to their lower relativistic mass. This implies that the endloss spectrum should exhibit a large amount of lower energies, and this is indeed seen to be the case in Fig. 4.9.

In fact, the experiment generally reproduces the expected dependence of the decay time on plasma parameters. Fig. 4.10 displays the measured diamagnetic loop decay time versus the calculated from $\tau_{coll} = 1/\nu_{coll}$ with ν_{coll} given by

$$\nu_{coll} = 7.7 \times 10^{-6} T_h^{-3/2} (\log R)^{-1} (2 n_h \lambda_h + 2 n_{H_2} \lambda_0). \tag{4.19}$$

The data was taken in a gas pressure scan. The electron-electron and electron-ion Coulomb logarithms are the same for hot electrons ($\lambda_h \sim 24$), and the electron-neutral Coulomb logarithm λ_0 is 5.5; it is considerably smaller because the maximum impact parameter for electron-neutral collisions is on the order of the Bohr radius rather than the Debye length. The factor of 2 in front of n_h is to account for ions as well as electrons,

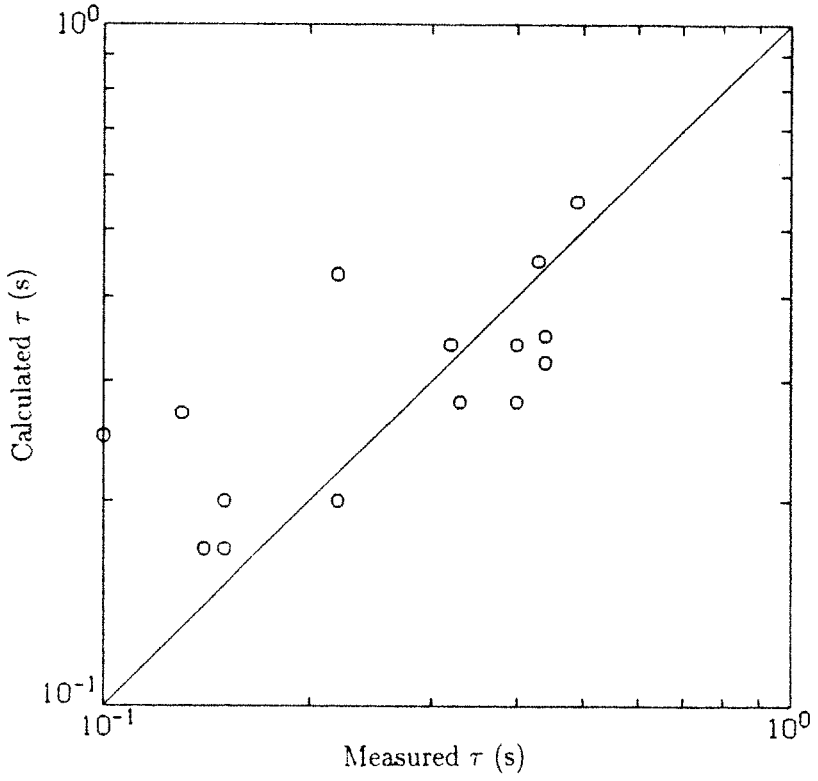

Figure 4.10: Measured and calculated values for the diamagnetic loop decay time in a pressure scan.

and the factor of 2 in front of n_{H_2} is to account for the fact that molecular hydrogen has roughly twice the scattering cross-section of atomic hydrogen. It is not necessary to have a great deal of accuracy in the neutral scattering term, because it is generally small. One can see from Fig. 4.10 that this formula, which is the standard formula for collisional loss in a mirror, models the measured decay rates reasonably well. The variation of T_h produces the dominant effect on τ_{coll} in a pressure scan such as this. The fact that Eq. 4.19 reproduces the diamagnetic loop decay rate, and not the interferometer decay rate, indicates that the interferometer is too insensitive to high energy electrons to be a good indicator of overall density with the collisionally-hardened distributions present in the afterglow. The fact that the x-ray count rate decays like the diamagnetic loop supports this assertion.

One can measure the total endloss power using the scintillator probe, and check that it agrees with the diamagnetic loop decay. In practice, it is an extremely time-consuming task to obtain full endloss profiles by radially scanning the scintillator probe, and they are only available for a selected set of parameters. Nevertheless, as Fig. 4.11 shows, there is some correlation between the decay power and the scintillator probe signal on the central field line in a pressure scan; as both the endloss and density profiles vary in a pressure scan, close correlation cannot be expected.

Another result of the stronger scattering of lower energy electrons is the fact that the average electron energy increases with time in the decay. This can be seen in Fig. 4.12, where the evolution of $\langle E \rangle$ derived from the x-ray spectra is compared to a Fokker-Planck calculation using the SMOKE code (Matsuda and Stewart, 1986). The effect is weaker in the simulation, and this, combined with the fact that the collisional endloss spectrum (Fig. 4.9) has a characteristic energy which is much lower than the hot electron temperature, indicates that $\partial f / \partial \theta$ is larger than expected at lower energies; the cause for this discrepancy has not been resolved, although it probably lies in the detailed structure of f that is produced by rf diffusion during the heating phase.

Although rf diffusion tends to play a dominant role in resonant regions in velocity-space, collisions still play a very important role in filling in the non-resonant regions. A

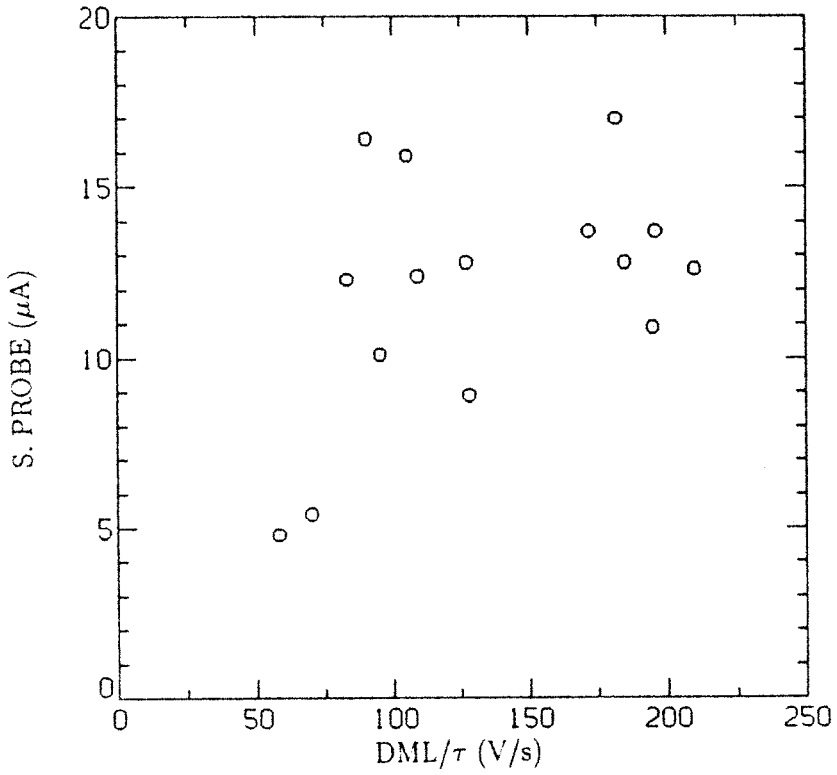

Figure 4.11: Scintillator probe signal on the central field line vs. decay power as measured by the diamagnetic loop in a pressure scan. $P_{rf} = 5$ kW, $B_0 = 3.0$ kG.

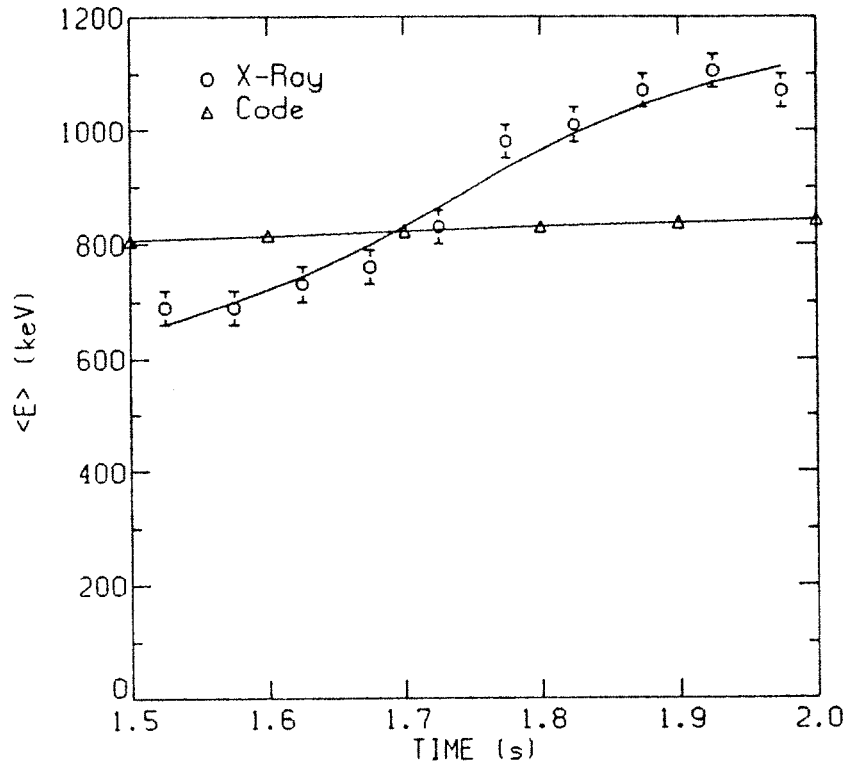

Figure 4.12: The average electron energy during the decay as measured with x-ray spectra and calculated with a Fokker-Planck code.

cold electron, for instance, experiences no resonance if it reflects inside of the resonant mirror ratio, and can scatter to larger pitch angles. This also means that even in strong rf diffusion regimes, the distribution function requires a significant fraction of a scattering time to reach equilibrium, because the equilibrium is determined only by collisions in large portions of velocity space. This is generally true in the experiment, where the onset of steady-state occurs at least tenths of a second after the rf is turned on.

In conclusion, collisional processes as measured in the experiment are consistent with the standard theory, and play an important role as the diffusion mechanism for non-resonant electrons.

4.5.2 Loss of Adiabaticity

Before going on to discuss the experimental investigation of rf diffusion, I want to briefly discuss one other diffusion mechanism, that of μ-diffusion due to loss of adiabaticity. A paper by Uckan (1982) states that the maximum temperature obtained in a number of ECH mirror devices tends to satisfy the criterion $\rho/L \sim 0.06$, and she attributes this to degraded confinement at high energies due to loss of adiabaticity. On the other hand, the theory developed by Chirikov (1979) and Cohen *et al.* (1978a) indicates that this value of ρ/L is too low to have a strong effect. In fact, as was pointed out in Chapter 3, collisonal diffusion is expected to be stronger. More importantly, the steady-state temperature achieved in a power scan in Constance varies from 300 to 450 keV *at constant scale length* L. One can rule out the possibility that there is a variation in the scale length due to plasma diamagnetism, because β is constant in such a power scan. Since there is no correlation between the steady-state temperature achieved and ρ/L, one can conclude that μ-diffusion does not play a major role in the confinement of electrons in the experiment. In fact, as Section 4.6.3 will show, the hot electron temperature is limited by the endloss induced by rf diffusion.

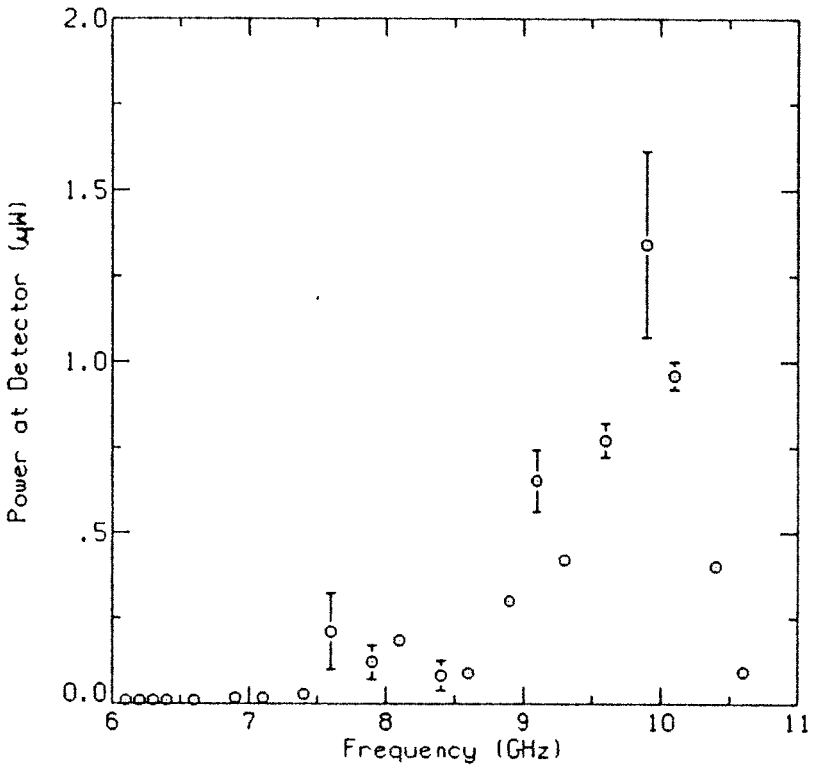

Figure 4.13: A typical frequency spectrum of whistler MRF. Data from R.C. Garner, Ph.D. dissertation, MIT, 1986, reprinted as MIT Plasma Fusion Center Report PFC/RR-86-23.

4.5.3 Electric Field Strength and Frequency

There are two forms of GHz frequency rf in Constance: the applied rf, and microinstability rf (MRF). The applied rf has a bandwidth of 1 MHz about the 10.5 GHz frequency, and can be considered monochromatic. The MRF, however, is quite broad-band and covers the frequency range 7–11 GHz, as indicated in Fig. 4.13.

The rf fields present in the experiment are measured by waveguides with attenuator/filter/diode combinations as described in Chapter 2. If applied rf waves experienced no refraction as they transversed the plasma, the 10.5 GHz power measured at the waveguide opposite the launching horn would give a measurement of rf absorption. An absorptive plasma, however, is a refractive plasma, and this measurement can only be expected to give a qualitative measure of the fields inside the plasma, being more accurate in low-absorption cases. The microinstability, on the other hand, produces emission which

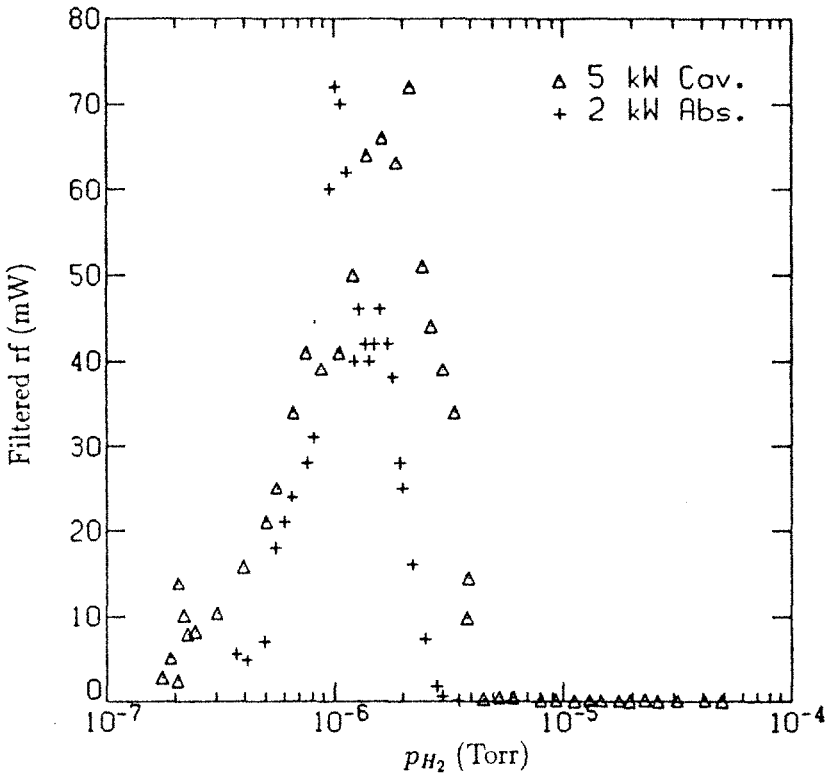

Figure 4.14: Whistler MRF vs. gas pressure.

is isotropic (Garner, 1986), probably due more to the field line geometry than any intrinsic property of the instability. In addition, the 10.5 GHz cavity fields have large-scale spatial uniformity, although they exhibit small-scale nodal structure across distances on the order of a wavelength (3 cm). I will therefore consider the measurements of time-averaged cavity and MRF fields to be representative of the corresponding average field levels inside the plasma, but will treat the measurements of 'unabsorbed' rf power using the waveguide opposite the launching horn with some caution.

The whistler microinstability results from the anisotropy of the warm tail in velocity space when strong rf diffusion pulls the distribution function along rf characteristics (Garner, 1986). For this reason, the instability is sensitive to variations in cold electron heating, which, in turn, is particularly sensitive to gas pressure. The result is a very strong dependence of MRF on gas pressure, as shown in Fig. 4.14. The most notable aspect is a sharp threshold pressure around 2×10^{-6} Torr, where the instability emission rapidly drops to zero. Apparently there is some critical change in the cold electron

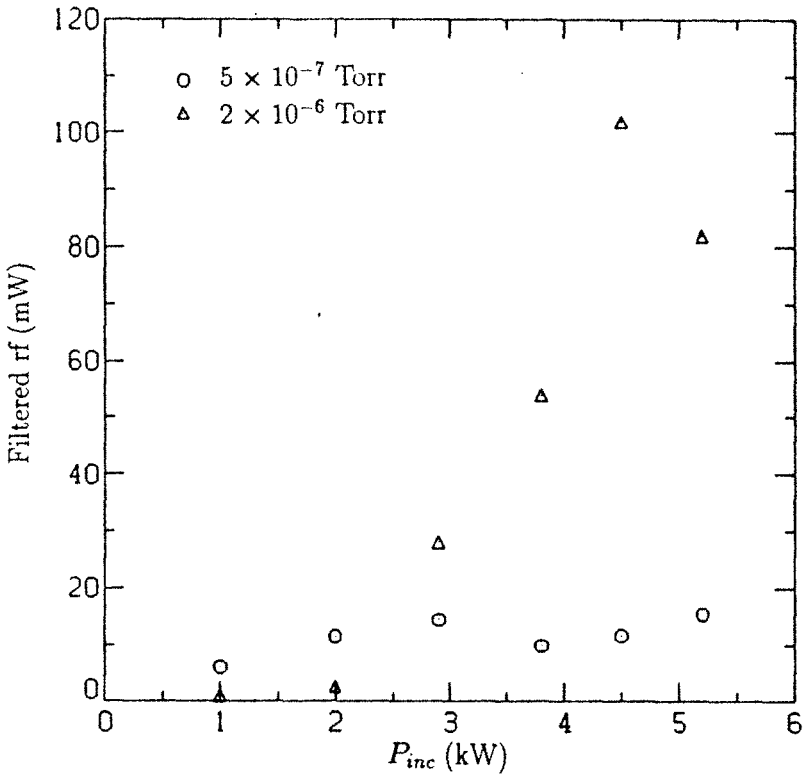

Figure 4.15: MRF vs. applied power, for two values of gas pressure.

population at this pressure, but why it occurs so suddenly remains a mystery. The threshold is slightly power-dependent, so that the emission is strongly power-dependent if the pressure is held constant in the threshold range (Fig. 4.15). On the other hand, the emission is not sensitive to power at low gas pressure (5×10^{-7} Torr).

Given that the microinstability is an indicator of cold electron heating, one might suppose that the cold plasma absorption would peak where the MRF peaks in a pressure scan. The 10.5 GHz power measured by the waveguide opposite the launching horn is shown in Fig. 4.16 for the same scan as Fig. 4.14. Although one should take these 'unabsorbed' rf numbers with a large grain of salt for the reasons mentioned above, they lend support to the claim that MRF is a symptom of strong cold electron absorption, and that cold electron absorption, in turn, has a large effect on the field strength.

There are two ways to have applied rf without MRF in the experiment: one is simply to run at gas pressures above 2×10^{-6} Torr, and the other is to employ the technique of 'second pulse' experiments. The latter scheme is shown in Fig. 4.17: both the rf and

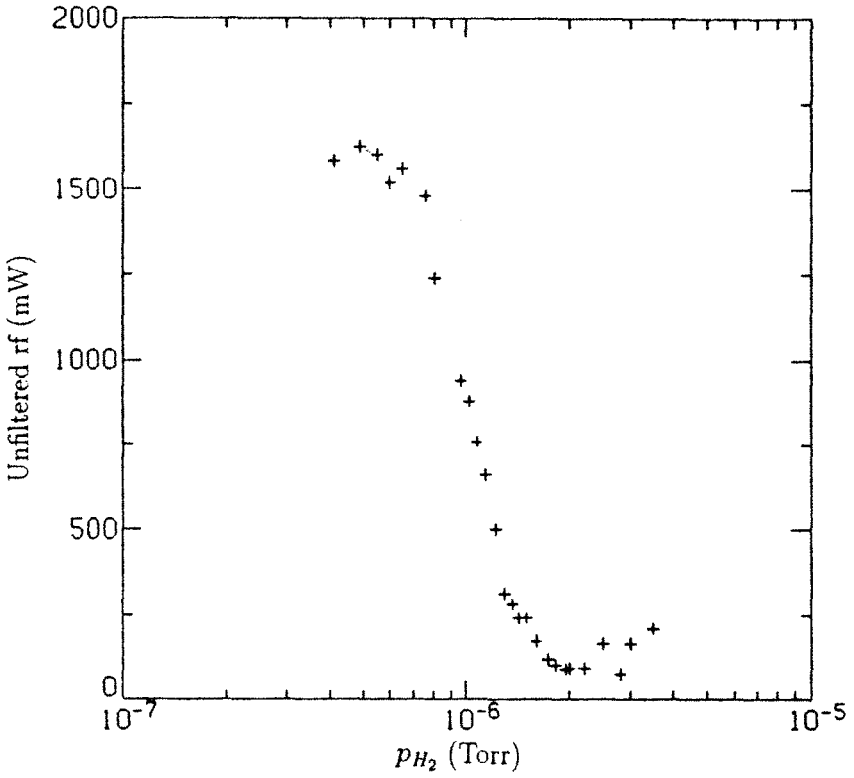

Figure 4.16: Unfiltered rf power (almost entirely composed of applied rf) vs. gas pressure at the waveguide located directly opposite the rf launching horn. The vacuum level is 4800 mW.

gas feed are turned off after steady-state has been reached, and the plasma is allowed to decay while the gas is pumped away; when the gas reaches a sufficiently low level such that cold plasma cannot be produced, the rf is re-applied, and the resulting diffusion on the hot electron component may be observed. With the cold electrons absent, the second pulse rf levels are similar to the vacuum level. These are the cleanest experiments for observing rf diffusion of the hot electrons, and will be discussed in detail. A big disadvantage of the second pulse experiments is that they require the gas pumping time to be less than the hot electron decay time; this, unfortunately, is not the case in the absorber experiments, where the loading of gas on the absorber prevents the gas level from reaching a sufficiently low level in a short enough time. All of the second pulse experiments have been conducted with cavity heating.

The second pulse experiments remove the microinstability because they remove the cold electrons; with cold electrons present, MRF is *always present* at pressures below 2×10^{-6} Torr, where the strongest heating is observed. It plays an important role in velocity-space diffusion, and its effect on heating and confinement will be discussed in later sections.

4.5.4 Super-Adiabaticity

Before going on to discuss some of the experimental aspects of rf diffusion, a very important question must first be addressed: does the phenomenon of super-adiabaticity exist in a real device? At worst, super-adiabaticity would invalidate the diffusion description; at best, it would slow diffusion down to a time scale corresponding to the dominant randomizing mechanism in the system (e.g. collisions). To answer this problem, I have investigated three aspects of super-adiabaticity that are predicted to be present: 1) a decrease in the heating rate as T_h exceeds the barrier energy E_s, 2) a large 'warm' component with $T_w \sim E_s$, and 3) reduced diffusion of hot electrons with $E \gg E_s$.

Heating rate. The hard x-ray spectra can be used to measure T_h only when there are a statistically significant number of counts in the energy range 100–1500 keV. This occurs for $T_h > 50$ keV, which is already above the barrier energy $E_s \sim 30$ keV. A high

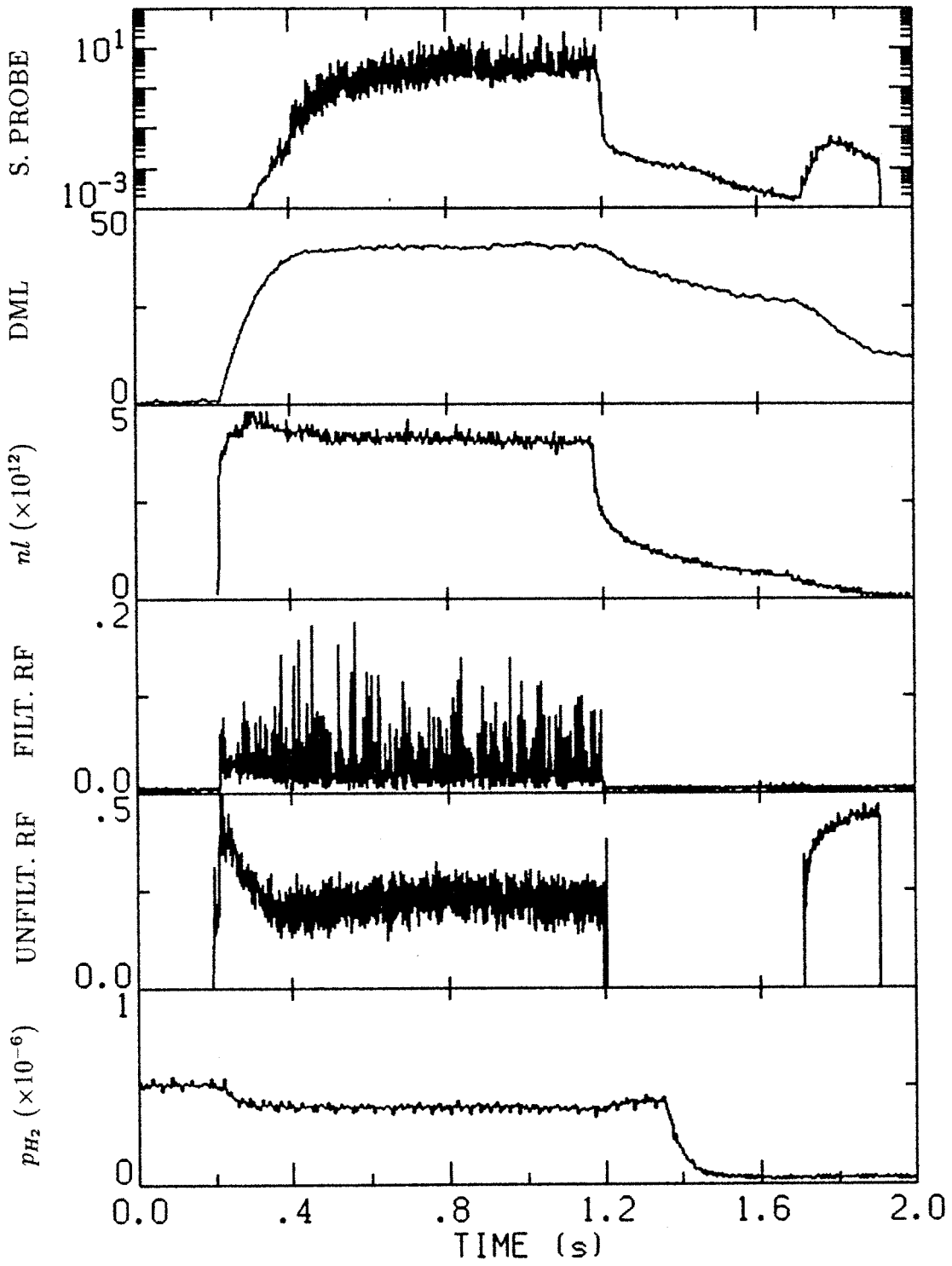

Figure 4.17: A 'second pulse' shot.

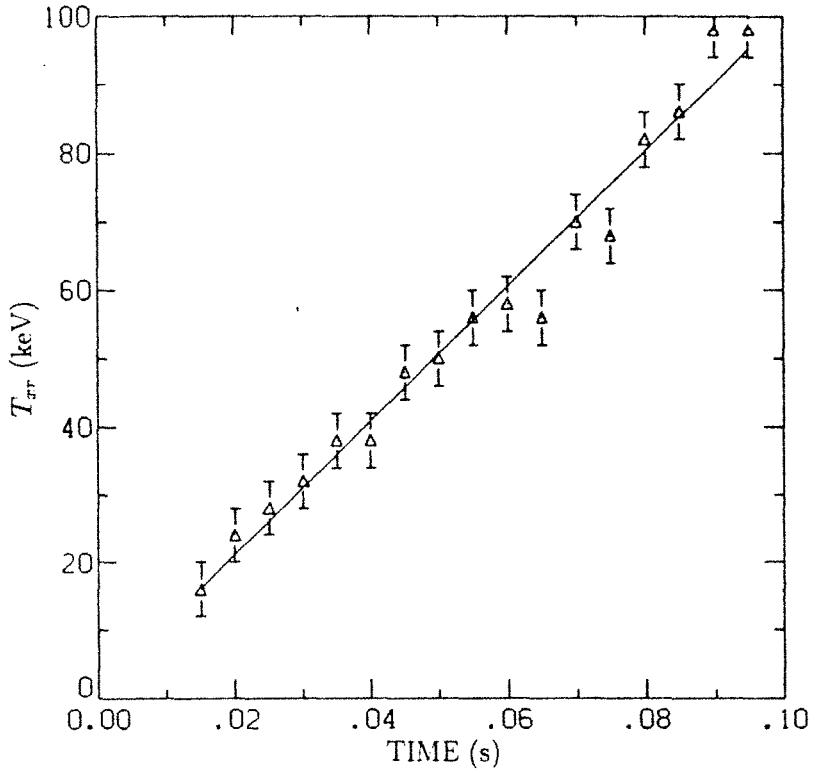

Figure 4.18: T_h as a function of time in the early portion of the discharge, as measured with the HPGe x-ray detector. $P_{rf} = 2$ kW, $B_0 = 3.2$ kG, $p_{H_2} = 5 \times 10^{-7}$ Torr.

purity germanium (HPGe) x-ray detector (see Appendix A) was therefore used to measure the heating rate dT_h/dt at the very beginning of the discharge. This data is shown in Fig. 4.18. The heating follows a constant value of $dT_h/dt = 1000$ keV/s throughout the early phase of the discharge, with no significant decrease observed; furthermore, the same rate is observed with hard x-ray measurements to continue up to temperatures in excess of 300 keV near the onset of steady-state.

Warm component. The spectra obtained with the HPGe detector do not reveal any significant component other than the hot electron component. The possibility still remains that a very low energy warm component of significant density may exist; this, however, has been ruled out by measurements with a Si(Li) soft x-ray detector. A composite spectrum produced by joining spectra from all three detectors for identical plasma conditions is shown in Fig. 4.19. The spectra are from an early time in the shot, when the relative contribution from warm electrons would be higher than in steady-state.

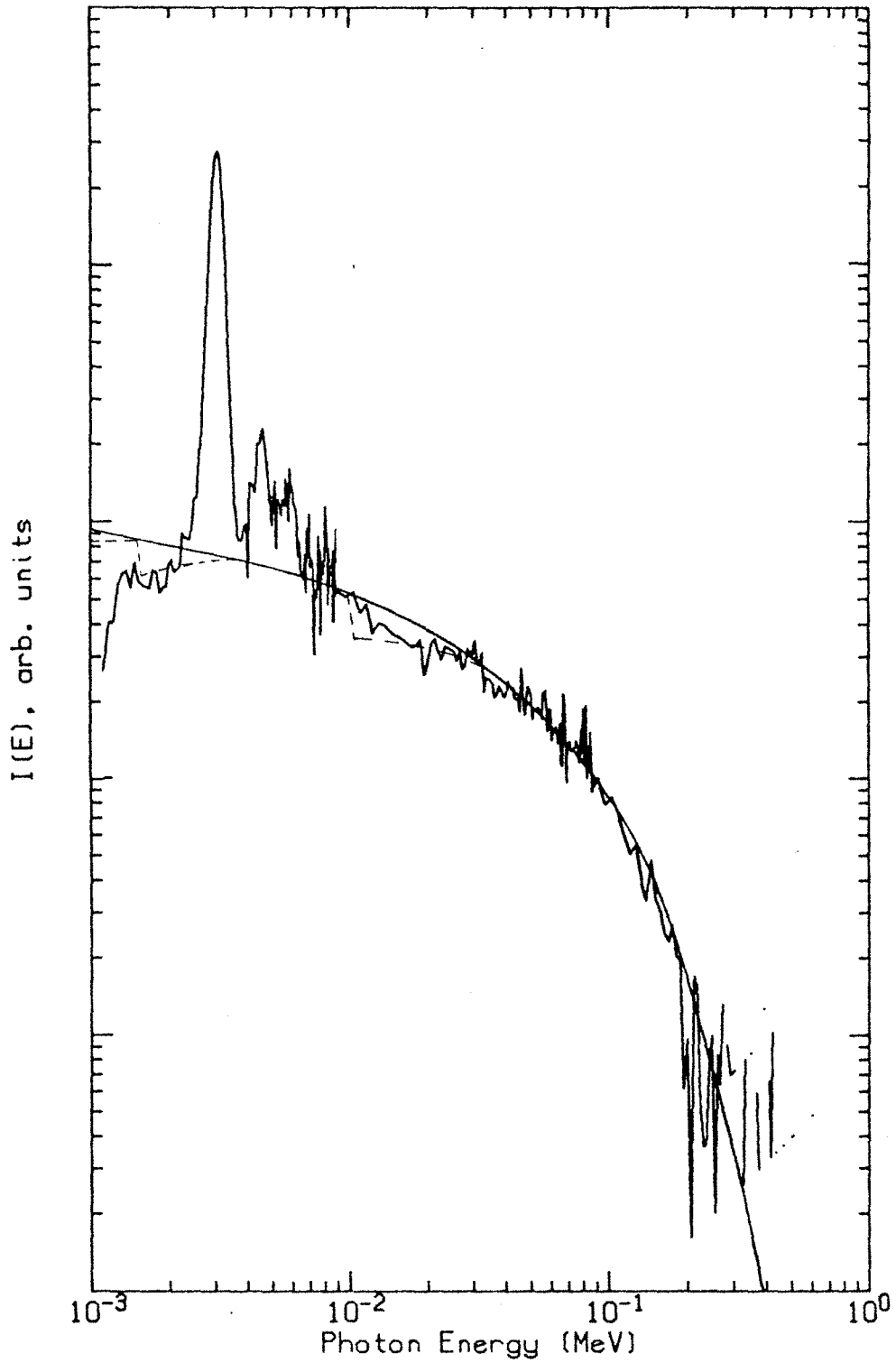

Figure 4.19: Composite spectrum taken with the Si(Li), HPGe, and NaI(Tl) detectors at a time early in the shot. The solid smooth line is the spectrum for a single mirror distribution component with $s = 1$ and $T = 60$ keV, and the dotted line is the calculated detector response.

The spectrum extends down to 1 keV in energy and exhibits two large K_α lines due to argon and titanium impurities, and is consistent with a calculated x-ray spectrum due to hot electrons alone. Because hot electrons produce a large amount of x-rays at low energies, these data cannot rule out the existence of a warm electron component at low density $n_w < 0.2n_h$. This, in fact, is presumed to exist and is referred to as the warm 'tail' on the cold distribution. However, a large density component due to sharply reduced heating at $T \sim E_s$ is not seen in the experiment.

High energy diffusion. The best means for examining the diffusion of high energy electrons is in the second pulse experiments, because only the applied rf is present and the situation approaches the model used in the rf Fokker-Planck code SMOKE. Fig. 4.17 indicates that the loss of hot electrons is strongly enhanced during the second pulse, as seen both in the increased decay rate of the diamagnetic loop signal, and the increased endloss seen with the scintillator probe. Figs. 4.20 and 4.21 display the results of the simulation for two cases: one in which the rf field strength is set to be equal to the cavity field level (15 V/cm) and has a uniform profile, and one in which the full applied field (100 V/cm) is used with a narrow profile. Both cases use the fully stochastic rf diffusion tensor. If super-adiabaticity were playing its expected role in the experiment, the diffusion due to the coherent direct field would be sharply reduced, and the incoherent cavity fields would provide most of the diffusion. One can see, however, that the strong second pulse decay is not present in the cavity field simulation and that, in fact, the full direct field is required to produce a decay similar to the experiment. Further evidence of full diffusion is shown in Fig. 4.22, where the decay rate and endloss signal are plotted as a function of second pulse power in a scan where the first (heating) pulse was kept at a fixed power. The fact that both quantities scale linearly with second pulse power gives additional support to the conclusion that the diffusion is fully stochastic.

Given that no effects of super-adiabaticity are seen in the experiment, it remains to be determined whether it is an altogether errant notion, or whether there are randomizing mechanisms in the experiment that negate its effect. Three randomizing mechanisms are leading candidates: MRF, cavity fields, and collisions.

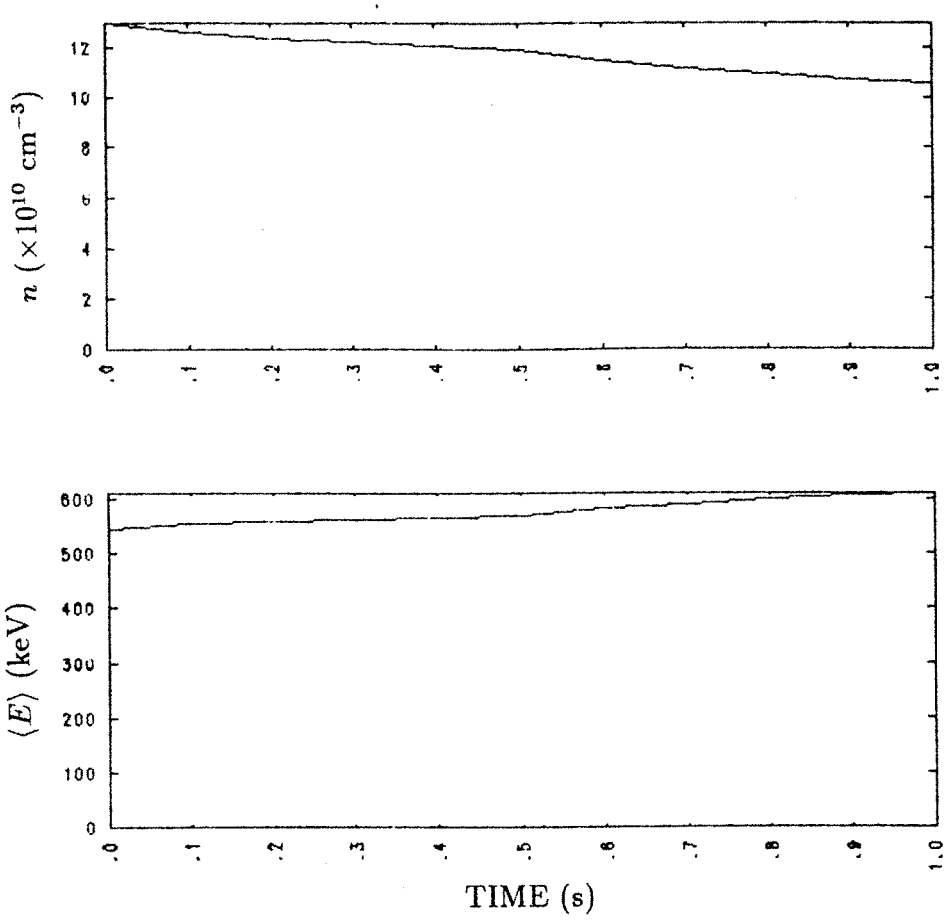

Figure 4.20: Time evolution of midplane density and average energy from a simulation of a second pulse experiment using the SMOKE code. In this case a narrow rf profile with $\mathcal{E} = 100$ V/cm was used.

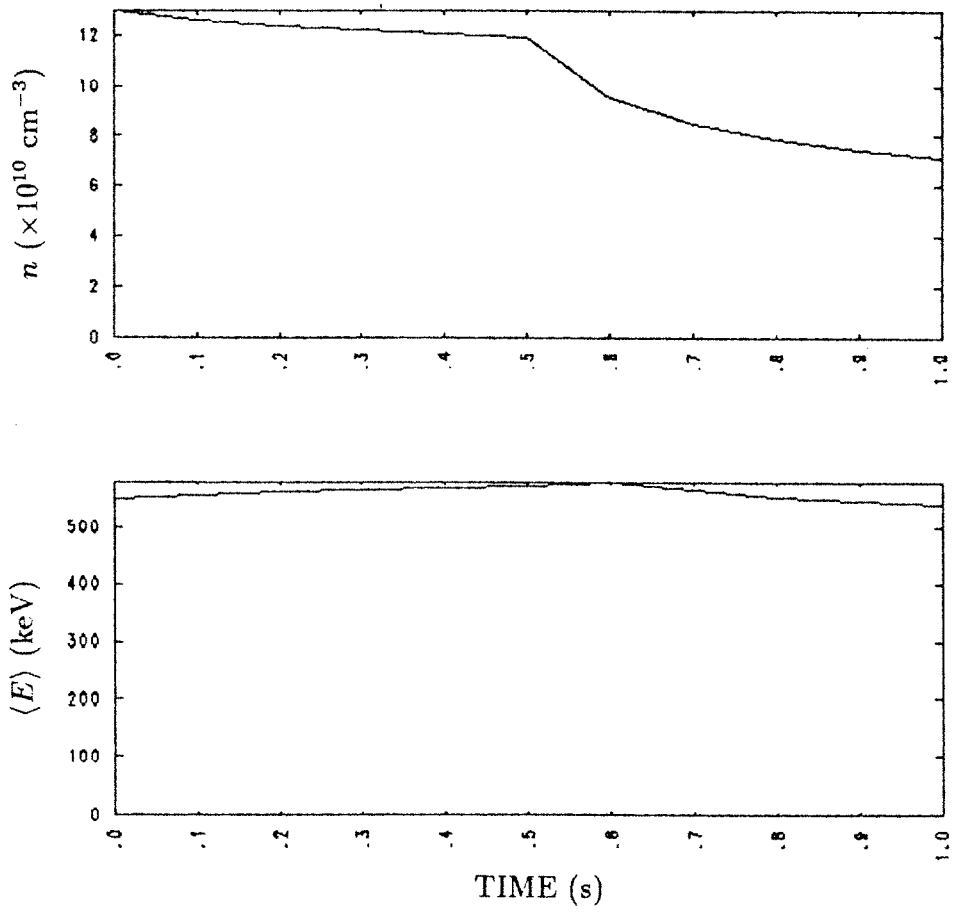

Figure 4.21: SMOKE simulation of a second pulse experiment with a uniform electric field profile with $\mathcal{E} = 15$ V/cm.

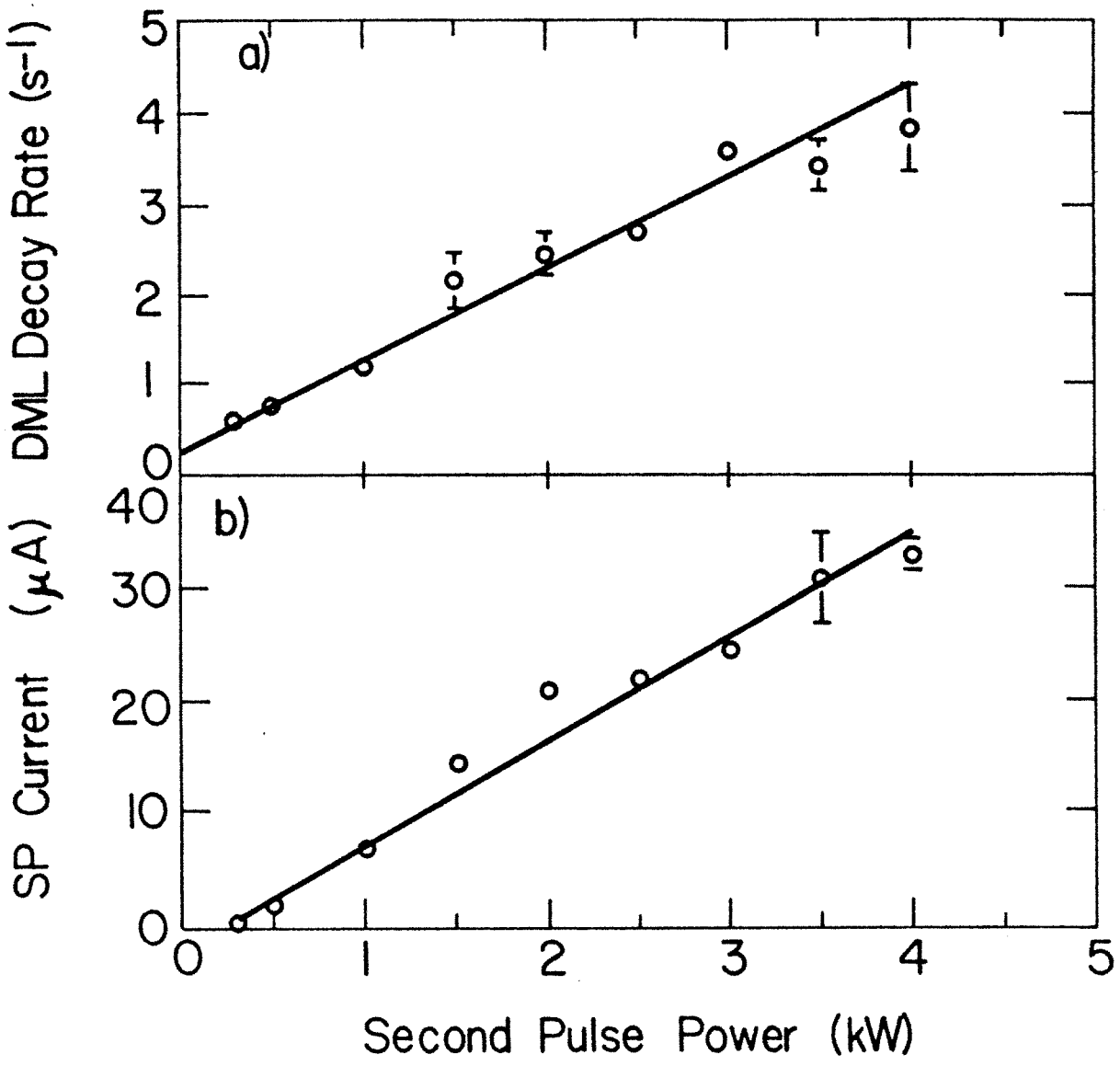

Figure 4.22: Diamagnetic loop decay rate and endloss signal vs. second pulse power in a scan where the heating pulse is fixed at $P_{rf} = 2$ kW.

Microinstability rf. When present, MRF may be expected to play a strong randomizing role, since the field strengths are significant ($\sim$ 1 V/cm) and the emission is incoherent. However, as was shown in Section 4.5.3, the microinstability is absent in the presence of high gas pressure (above 2×10^{-6} Torr). If MRF were the dominant phase randomizing mechanism, the steady-state hot electron temperature would be expected to be lower in its absence; this is not the case in the experiment, where 500 keV temperatures have been attained in micro-stable regimes.

Cavity fields. Because wall-reflected rf is incoherent, it can be expected to produce stochastic diffusion and possibly randomize the particle phase sufficiently to result in stochastic diffusion by the coherent applied rf, as discussed in Section 3.5.4 of Chapter 3. This has been experimentally tested in the absorber experiments — the microwave absorber reduces the cavity field level to less than 3 V/cm, as compared to 8 V/cm in the corresponding cavity situation ($P_{rf} = 2$ kW). As Fig. 4.23 shows, lower temperatures as well as lower heating rates are obtained in the absorber experiments. It will be argued in Section 4.5.6 that the higher diffusion levels in the cavity heating case are due to the broad spatial rf profile associated with cavity fields, although the experimental data do not rule out the possibility that cavity fields play a role in reducing super-adiabatic effects.

Collisions. It is difficult to directly determine whether collisions play a randomizing role in the experiment because they cannot be removed. Experiments have been performed in high Z gases, such as argon, with no significant increase in T_h, although the higher collisionality is evident in the x-ray spectrum (there is a deficit of lower energy photons due to the collisional 'hole' in the distribution).

4.5.5 Diffusion Paths

Given that the electrons experience strong rf diffusion, it is interesting to ask what effect the diffusion path structure has on the distribution function. Fig. 4.24 shows the diffusion paths in momentum space for the central field line at the standard magnetic field. The paths cover the region extending from the loss cone boundary at $\theta = 45°$ to $\theta \sim 60°$. In

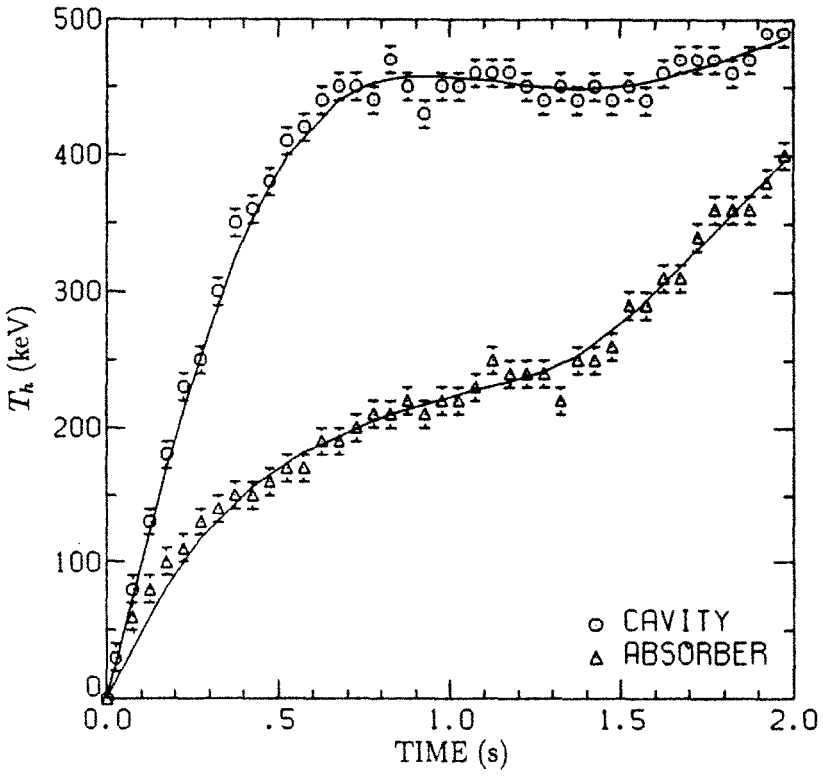

Figure 4.23: Time evolution of hot electron temperature for the cases of cavity heating and heating in the presence of microwave absorber. $P_{rf} = 2.0$ kW, $B_0 = 3.0$ kG, $p_{H_2} = 5 \times 10^{-7}$ Torr. The rf is turned off at $t = 1.5$ s.

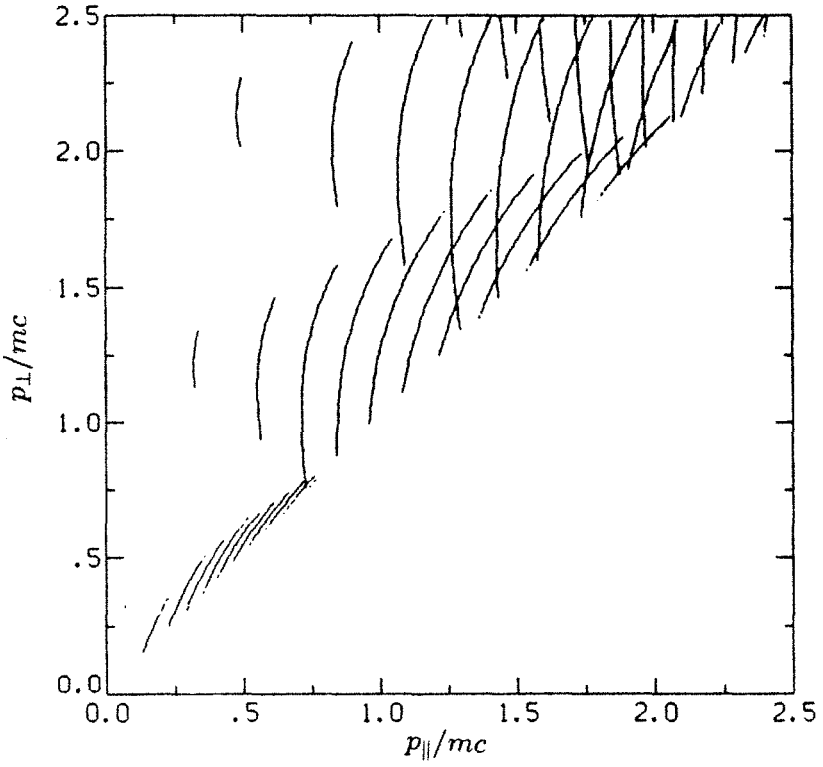

Figure 4.24: RF diffusion paths in momentum space, for a field line with $B_0 = 3.0$ kG and harmonics up to $l = 4$, with $k_\parallel = 0.5$ cm^{-1}. The paths are shown only in regions where the electrons are resonant.

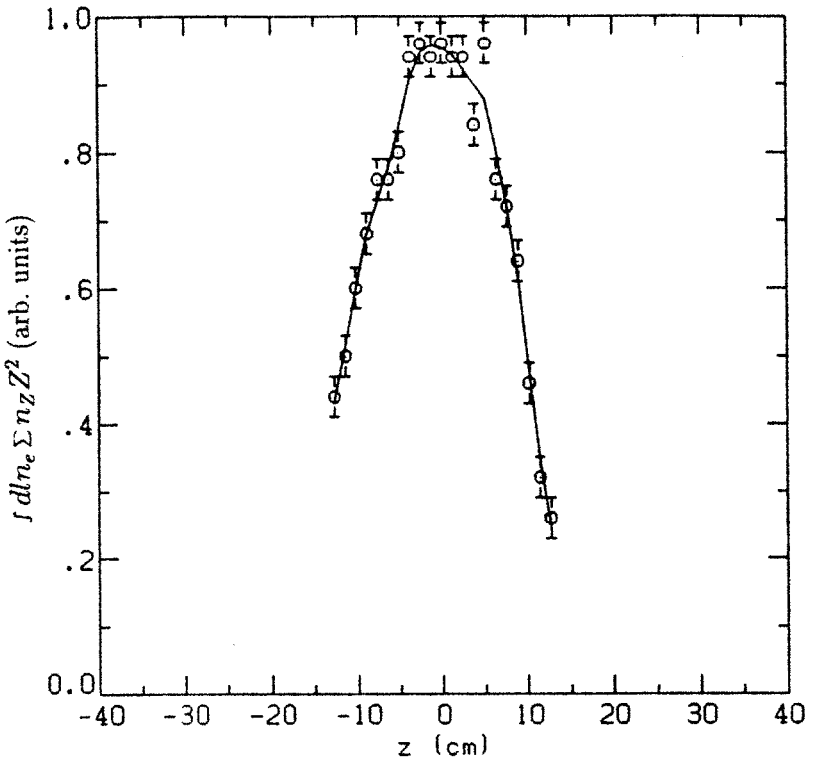

Figure 4.25: The density product profile obtained with hard x-ray measurements. $P_{rf} = 1$ kW, $B_0 = 3.2$ kG, $p_{H_2} = 1 \times 10^{-6}$ Torr.

the presence of strong rf diffusion, therefore, one expects poor confinement of electrons with pitch angles in this region since it is strongly connected to the loss cone along the diffusion paths. In the non-relativistic case, the upper boundary is at the turning point resonance given by $\sin^2\theta = 1/R_h$; this leads to the 'effective loss cone' boundary along the turning point resonance which has been quoted by many authors (e.g. Bernstein and Baxter, 1981). It is interesting that in the relativistic case, the resonant region spans a similar range of pitch angles.

The poor confinement in the resonant region results in a density (or plasma pressure) axial profile which falls to zero well inside the mirror peak. This has been seen in the experiment in a number of ways: Fig. 4.25 shows the axial profile of the chord-integrated electron-target density product

$$\int dl \left(n_e \sum n_Z Z^2 \right)$$

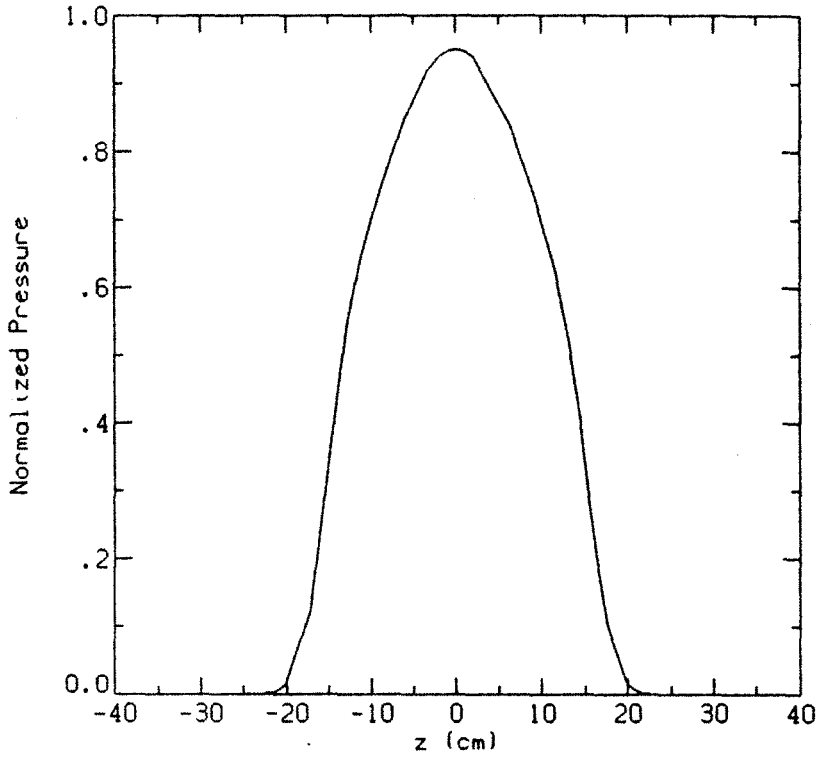

Figure 4.26: The axial pressure profile determined by Xing Chen using magnetic measurements.

obtained by scanning a hard x-ray detector axially in the $y = 0$ plane. Fig. 4.26 displays the axial pressure profile on the central field line determined by Xing Chen using magnetic measurements. Both profiles reveal that the electrons are confined within $z = 20$ cm, well inside the mirror peak at $z = 40$ cm. This result was mystifying for a long time, because there seemed to be no reason why the hot electrons, which have relativistic resonances at all magnetic fields, would be confined inside the position traditionally associated with the non-relativistic resonance. The relativistic diffusion paths shown in Fig. 4.24 provide the answer.

More quantitative support can be found in rf Fokker-Planck simulations. Fig. 4.27 shows an initially Maxwellian electron distribution function after it has been diffused by $l = 1$–4 harmonic resonances, and the corresponding axial pressure profile. It is clear that the poor confinement in the resonant region results in an axial pressure profile which is quite similar to the experimentally measured one. Furthermore, *it is essential*

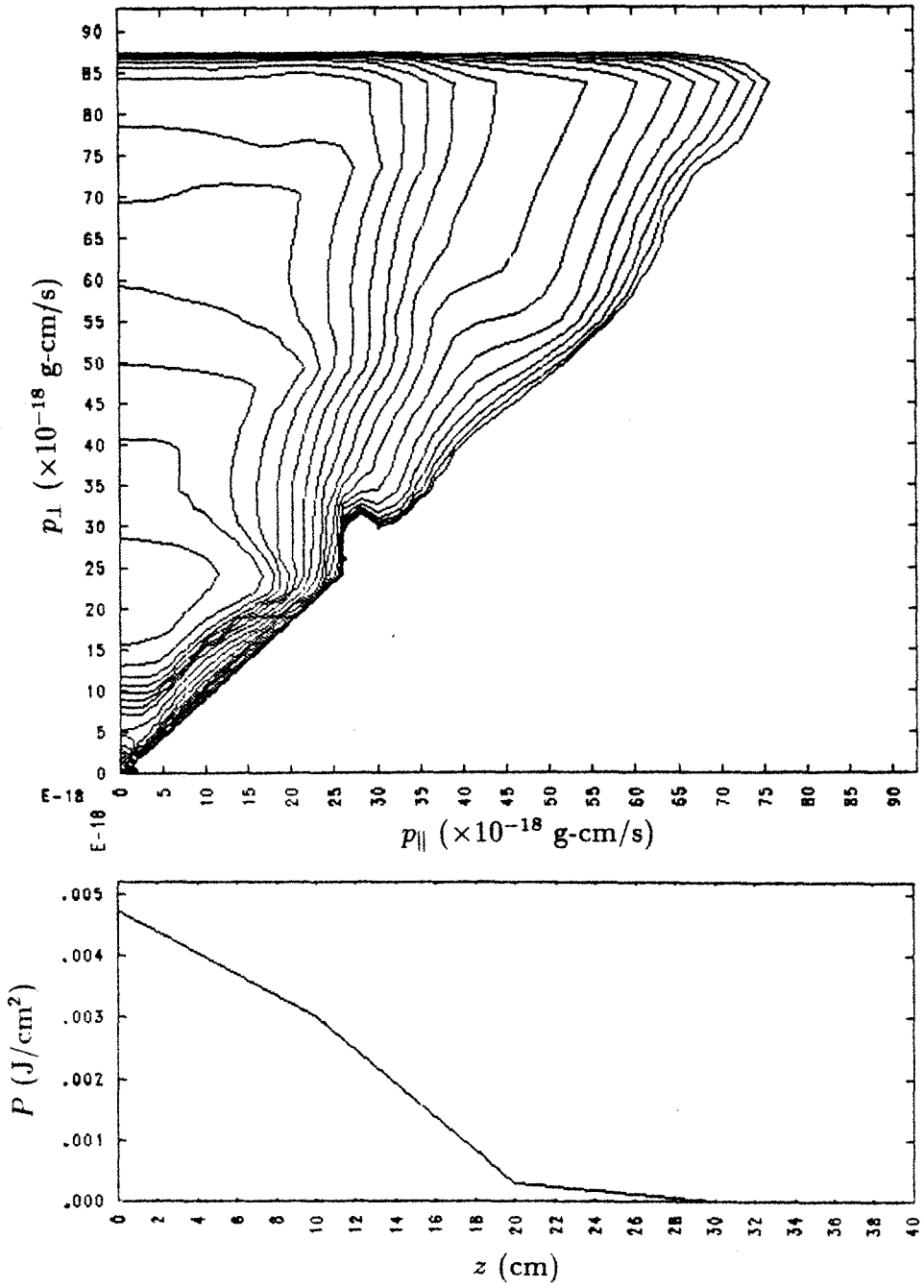

Figure 4.27: Contours of the electron distribution function and the associated axial pressure profile calculated by the SMOKE code in the presence of $l = 1, 2, 3, 4$ rf diffusion.

that the higher harmonics be included. Fig. 4.28 shows a similar simulation with only the fundamental resonance included — in this case, only a small chunk is removed from the distribution at low energies near the loss cone. Of course, a 500 keV distribution cannot be formed in the presence of only the $l = 1$ resonance in the first place, but this result serves as a reminder of the importance of high harmonic diffusion.

The structure of the rf diffusion paths at the higher harmonics plays another important role — the strong diffusion into the loss cone at high energies limits the hot electron temperature that can be attained. I will defer the discussion of the experimental and simulation results on this topic to Section 4.6.3, where the various effects governing T_h will be presented in a single discussion.

Another aspect of rf diffusion paths is their dependence on magnetic field. As the field is lowered, the ECH resonance moves closer to the mirror peak, and the diffusion paths therefore move closer to the loss cone in velocity space. It is reasonable to think, therefore, that rf-induced endloss will be enhanced relative to collisional endloss as B_0 is decreased. This is, in fact, seen to be the case in the second pulse data[2] shown in Fig. 4.29. It is difficult to model this effect, because all plasma parameters change when the magnetic field is varied, and it is difficult to determine the relative contributions of the change in the diffusion paths and the change in the distribution function.

It is clear that the structure of rf diffusion in velocity space has basic observable consequences in an experiment. In fact, one of the great advantages of a mirror device is the linkage between spatial and velocity space coordinates, and the ability to directly measure velocity-space currents, that allows for the observation of such effects. Other devices such as bumpy tori and stellarators have related effects on confinement due to rf diffusion; these will be discussed in Chapter 5.

[2]The scintillator probe used here is of a different design than the one used for the rest of the data in this thesis, and has not been calibrated, although it is known to detect only electrons with energies above at least 200 keV.

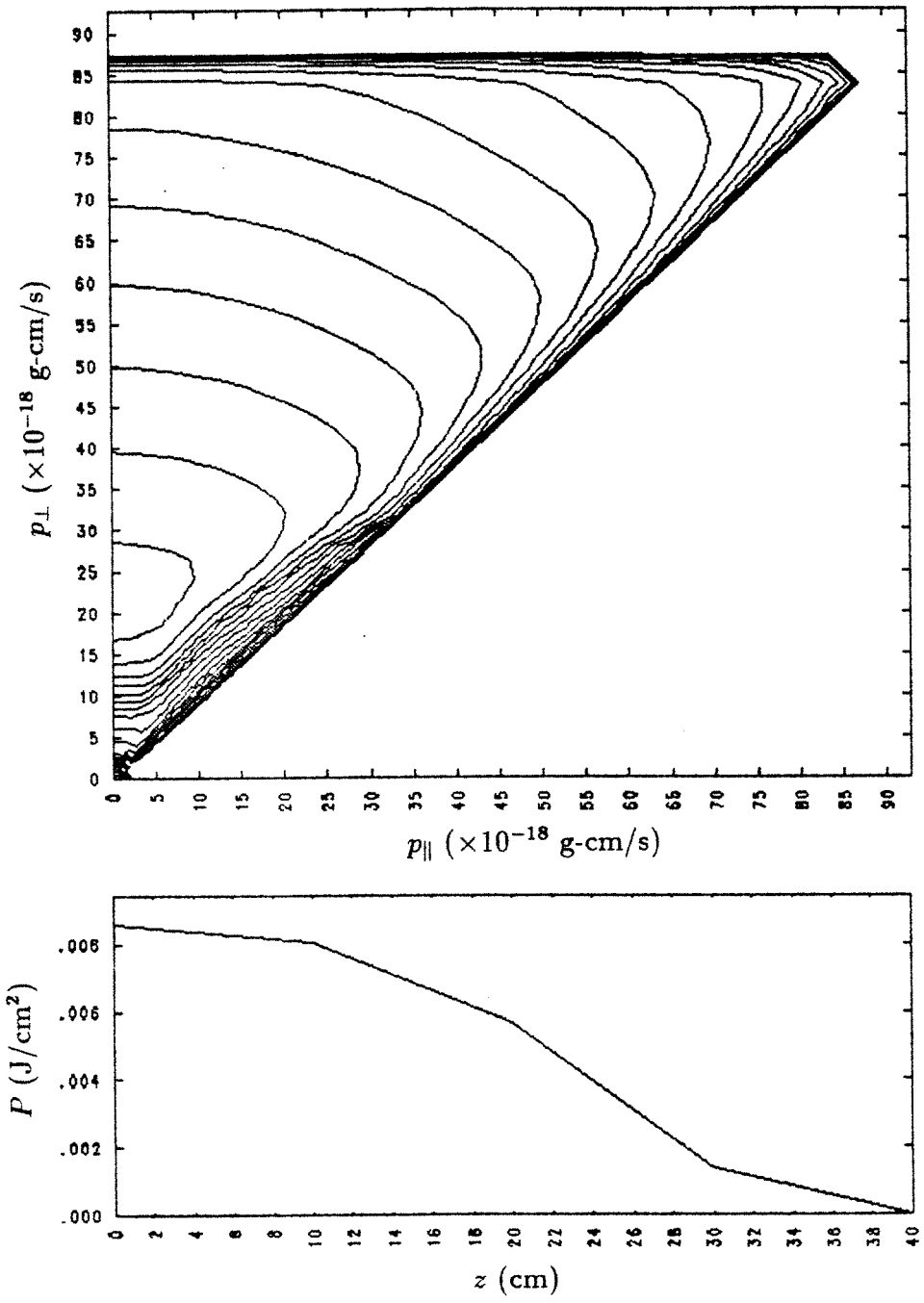

Figure 4.28: The results of a SMOKE simulation with only the $l = 1$ resonance included.

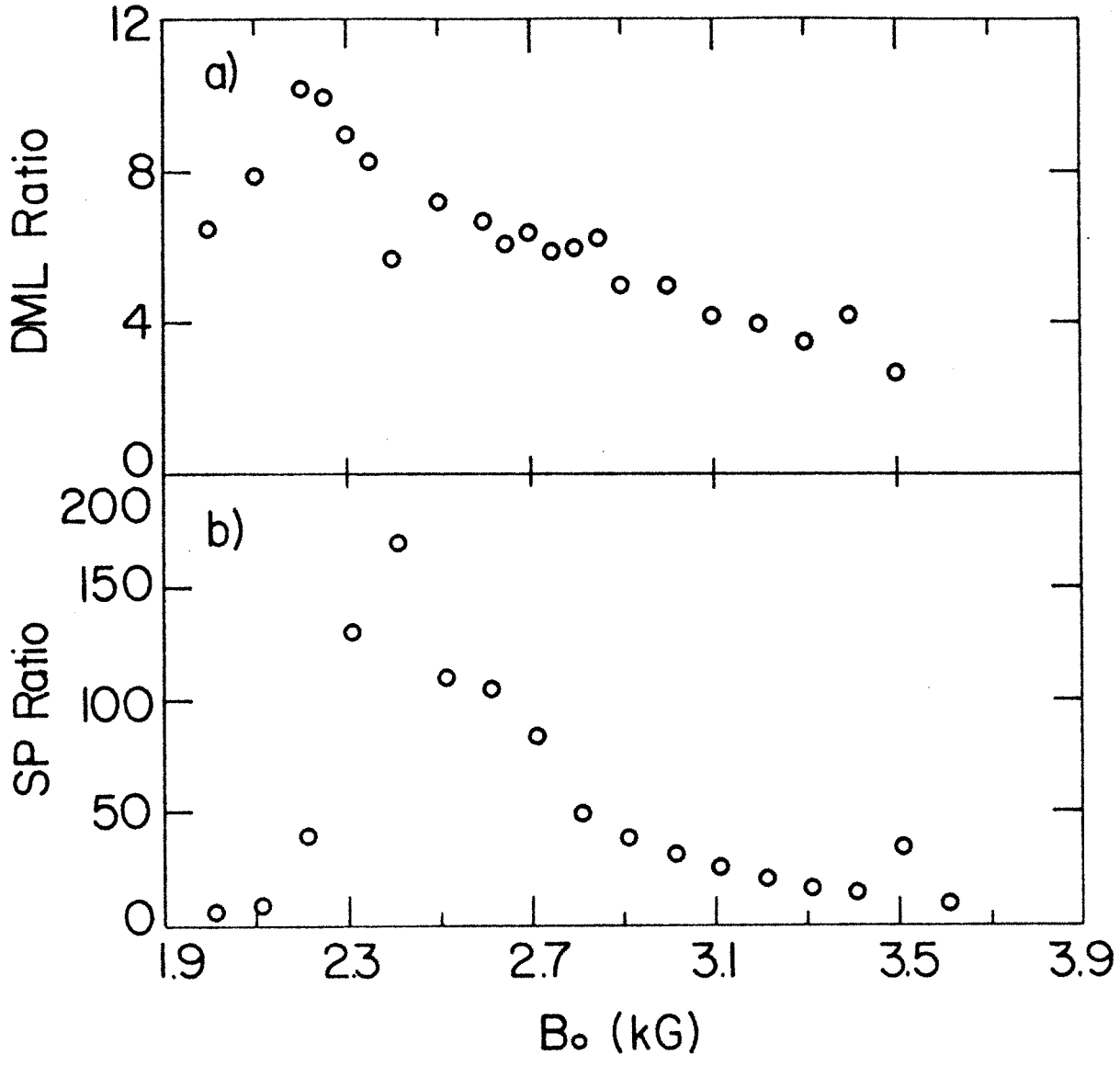

Figure 4.29: Second pulse results for a magnetic field scan: a) ratio of second-pulse to collisional endloss measured with a scintillator probe, b) ratio of second-pulse to collisional DML decay rate.

4.5.6 Cavity Fields

Another important factor in velocity-space diffusion is the electric field spatial profile, since it determines which portions of velocity space have resonances. Although the launched electric field profile has not been varied in the experiments (it undoubtably is an interesting 'knob' potentially available), the level of cavity fields has been varied, and they are the dominant fields outside of the launched rf beam.

As I've already mentioned, the cavity field levels have been found to be an important factor in heating: the presence of absorber reduces the heating rate from 1000 keV/s to around 400 keV/s, and the steady-state T_h from 450 keV to 250 keV for the parameters of Fig. 4.23. The only difference between the two cases is the cavity electric field strength: approximately 8 V/cm for the cavity case, 3 V/cm for the absorber case. The direct (first-pass) field strength is around 60 V/cm, so one sees that the small fraction of cavity field energy (around 8% for the cavity case, 1% for the absorber case, accounting for the larger volume taken up by the cavity fields) has a large effect on the evolution of the hot distribution.

There are two possible explanations for the observed enhancement of heating with higher cavity field levels: one is that the random cavity fields aid diffusion by reducing super-adiabatic effects, which was discussed earlier, and the other is that the wide cavity rf profile aids overall heating by introducing resonances in portions of velocity space that are not resonant with the direct fields. Given the other experimental evidence that super-adiabatic effects are not present, and the theoretical prediction that the randomizing effect of cavity fields is not significantly greater than collisions (Section 3.5.4), it is worthwhile to investigate the second explanation in some detail.

The first observation to make is that the direct field profile is localized well inside of the mirror peak (between $z = 0$ and $z = -20$ cm on the central field line), and therefore electrons will become detuned as their energy increases. This occurs for $E \sim 250$ keV on the central field line at $B_0 = 3.0$ kG. The effect that this has on heating can be seen in SMOKE simulations: Fig. 4.30 shows the time evolution of $\langle E \rangle$ for the cases of a 1 V/cm

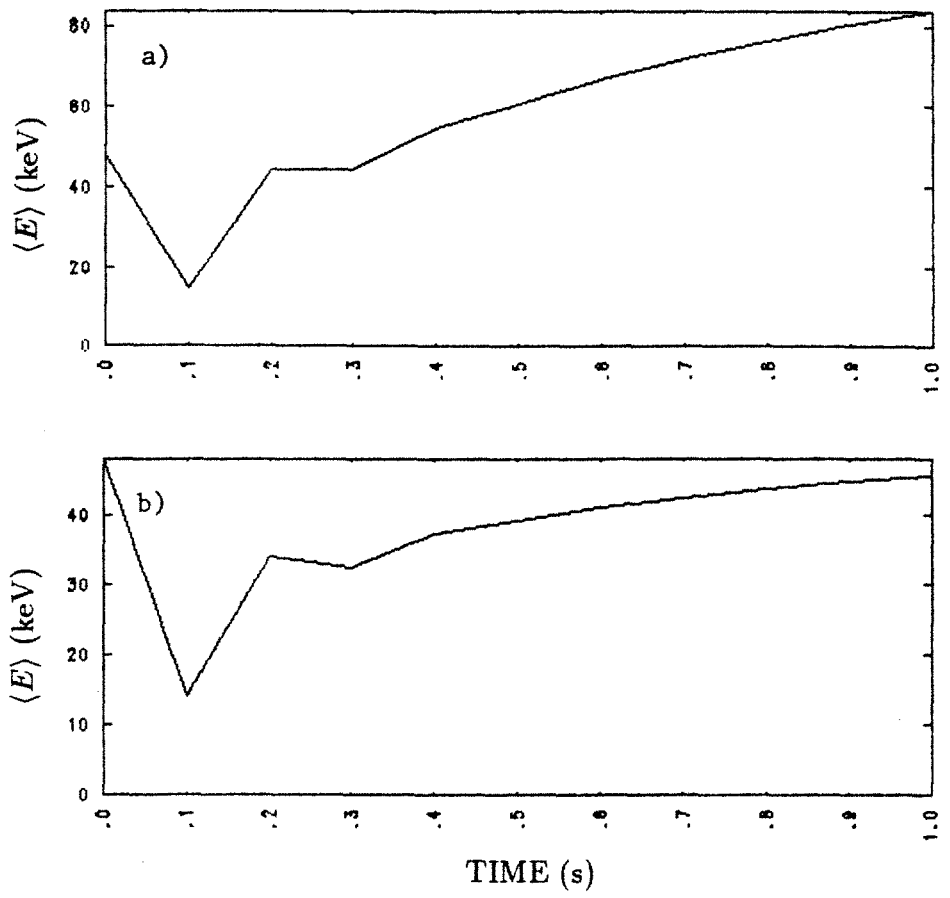

Figure 4.30: Time evolution of average electron energy from SMOKE simulations: a) 3 V/cm uniform field, b) 1 V/cm uniform field. In both cases a narrow rf profile with a peak field of 20 V/cm is included.

uniform profile and a 3 V/cm uniform profile, both having an additional Gaussian profile with a width of 14 cm and 20 V/cm peak field (simulations with a 60 V/cm peak field do not exhibit heating, apparently due to extremely rapid diffusion into the loss cone). The case with the larger uniform profile has significantly stronger heating (the density is the same in the two cases). It is clear from power balance considerations, however, that the direct field does provide the bulk of the heating in the experiment, since a small fraction of power goes into cavity fields. Nevertheless, it is easy to imagine that a broad profile of low-level cavity fields is important in diffusing the electrons through the 'gaps' that would be present in their absence, and therefore allowing electrons to reach the higher harmonic direct field resonant regions.

Another effect of cavity fields is to broaden the $k_{\|}$ spectrum. The direct rf has a narrow range of $k_{\|}$ values on any given field line, due to the narrow beam, whereas the cavity fields have **k** vectors with all orientations. This increases the portion of velocity-space that is resonant with the cavity fields, and further enhances the effect discussed above. The Fokker-Planck code is not suited to a simulation of this effect, because it assumes a single **k** vector for the wave.

In conclusion, I believe that the observed enhancement in the hot electron heating in the cavity experiments is due to the added diffusion caused by the broad cavity field *profile*, and not due to a reduction of super-adiabatic effects. Although the data is certainly not conclusive, this assertion is supported by three facts: 1) other aspects of super-adiabaticity have not been observed, 2) cavity fields are not theoretically predicted to have a strong effect on super-adiabaticity, and 3) a broad rf field profile is theoretically required for diffusion up to 400 keV temperatures.

The results presented in this section show that: 1) collisional diffusion obeys the standard theory, 2) the electric field strength is dependent on cold electron absorption, 3) breaking of μ is not significant, 4) super-adiabaticity plays no observable role, 5) the diffusion path structure results in axially limited confinement, and 6) cavity fields play an important role in the diffusion process. The remaining task is to see how all of these

factors come together in the heating and confinement of hot electrons, and this is done in the next and final section of this chapter.

4.6 Hot Electron Heating and Confinement

In the previous sections, I have discussed the the factors that enter into the velocity-space diffusion coefficient D and the hot electron source $n_c\nu_{c\to h}$. These can be varied in the experiment by means of the three 'knobs': applied power, gas pressure, and magnetic field. This section, then, presents the results on hot electron heating and confinement, and connects them with the ideas developed previously. It is divided into five parts: 4.6.1 discusses heating rates and the approach to steady-state; 4.6.2 deals with the equilibrium stored energy; 4.6.3 discusses the equilibrium hot electron temperature; 4.6.4 presents endloss results; and 4.6.5 discusses the absorbed power fraction.

4.6.1 Heating Rates

There are two ways of defining the heating rate, either $dW_\perp/dt$ or dT_h/dt, and these can be quite different in the experiment; both are well-defined, however, because both W and T_h tend to have a linear rise at early times. The reason the two differ is that $dW_\perp/dt$ includes the hot electron density buildup and is therefore sensitive to the particle source, whereas dT_h/dt is sensitive to the details of hot electron diffusion and tends to be more dependent on electric field. Figs. 4.31 and 4.32 show the two rates for power scans at fixed gas pressure; one sees that both are approximately linear functions of P_{rf}. This isn't surprising, since one generally expects a linear dependence on power since D_{rf} has a simple $\mathcal{E}^2$ dependence.

The more surprising result occurs in a gas pressure scan, where the cold electron heating varies strongly (Section 4.4). Figs. 4.33 and 4.34 show the corresponding data (there are much fewer points for dT_h/dt since up to 20 shots are required for a single point for good x-ray statistics). The two rates exhibit markedly different behavior, with dT_h/dt largest at low pressures and $dW_\perp/dt$ peaking at an intermediate pressure. The reason lies in the competition between cold absorption and diffusion strength: at

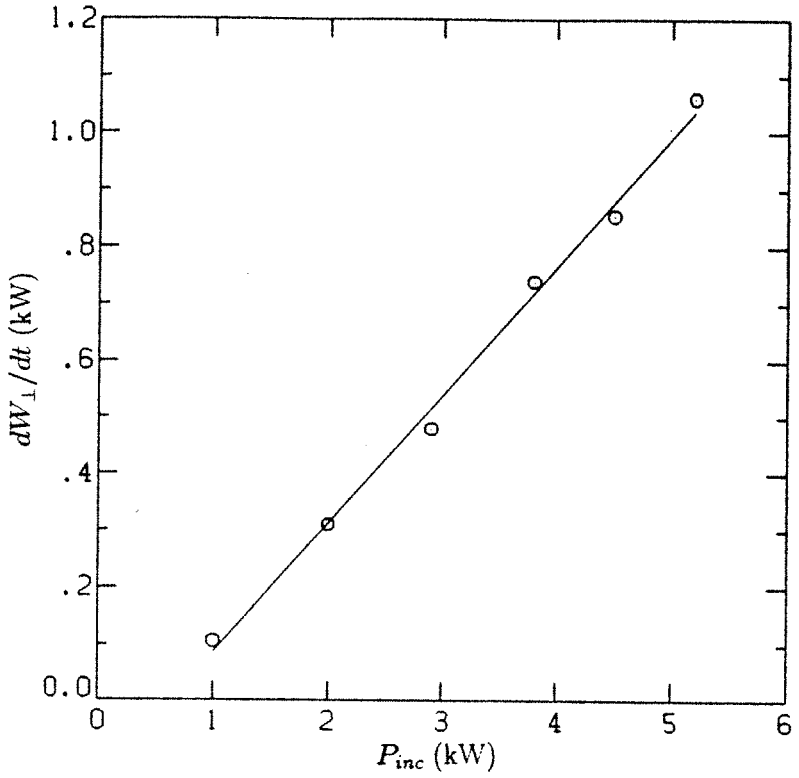

Figure 4.31: Initial heating rate $dW_\perp/dt$ in a power scan. $B_0 = 3.0$ kG, $p_{H_2} = 2 \times 10^{-6}$ Torr.

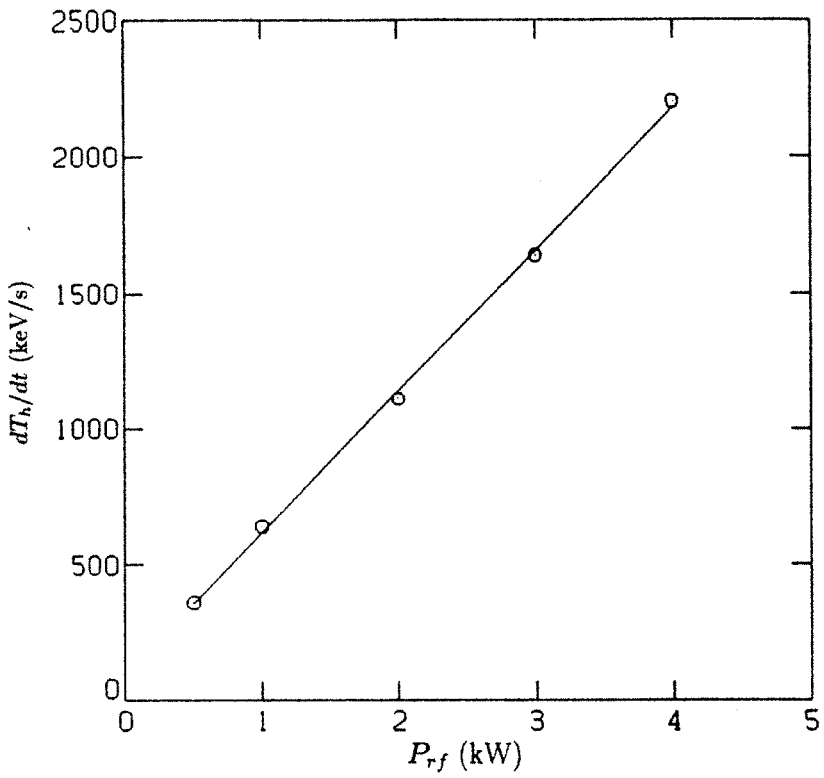

Figure 4.32: Heating rate dT_h/dt in a power scan. $B_0 = 3.0$ kG, $P_{H_2} = 5 \times 10^{-7}$ Torr.

low pressures the cold absorption is low and the electric field is correspondingly high, producing strong hot electron diffusion; at higher pressures the cold absorption is higher, providing a strong source, at lower electric fields. Thus the hot electron density buildup is much stronger at the intermediate pressure, and this results on an overall increase in $dW_\perp/dt$. Many of the experimental results can be understood in terms of this competition between electric field strength and source strength.

4.6.2 Stored Energy

One of the most notable aspects of confinement in Constance is the fact that increasing the applied rf power does *not* increase the stored energy, only the rate at which equilibrium is reached. Fig. 4.35 displays the steady-state stored energy $W_\perp$ as determined by the diamagnetic loop for the same power scan as the data shown in Fig. 4.31. This is the maximum stored energy obtained in Constance. The fact that $dW_\perp/dt$ increases with applied power indicates that rf diffusion is indeed strengthening; the fact that the

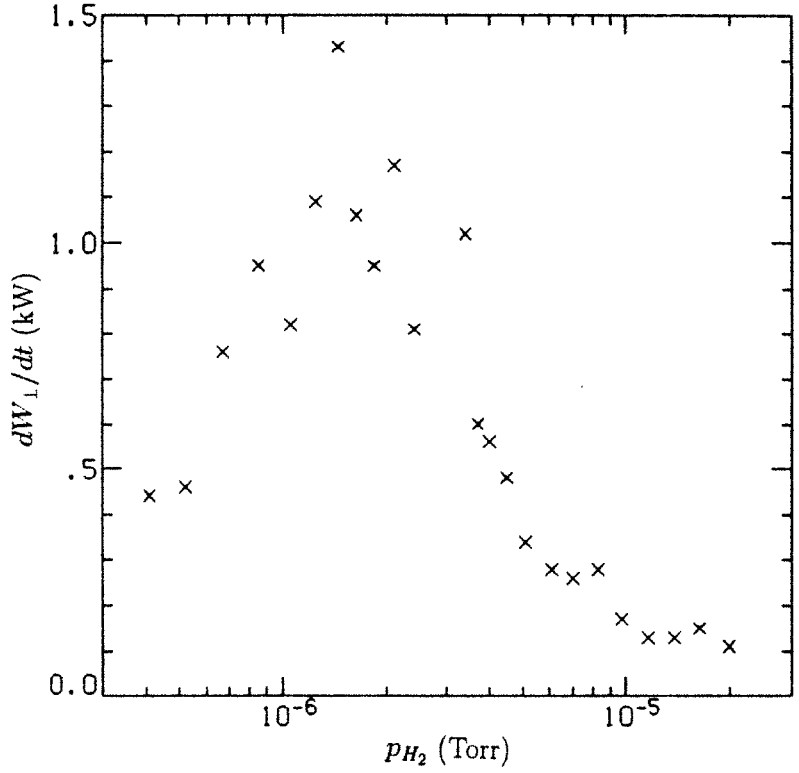

Figure 4.33: Heating rate $dW_\perp/dt$ in a gas pressure scan. $B_0 = 3.0$ kG, $P_{rf} = 5$ kW (cavity X-mode).

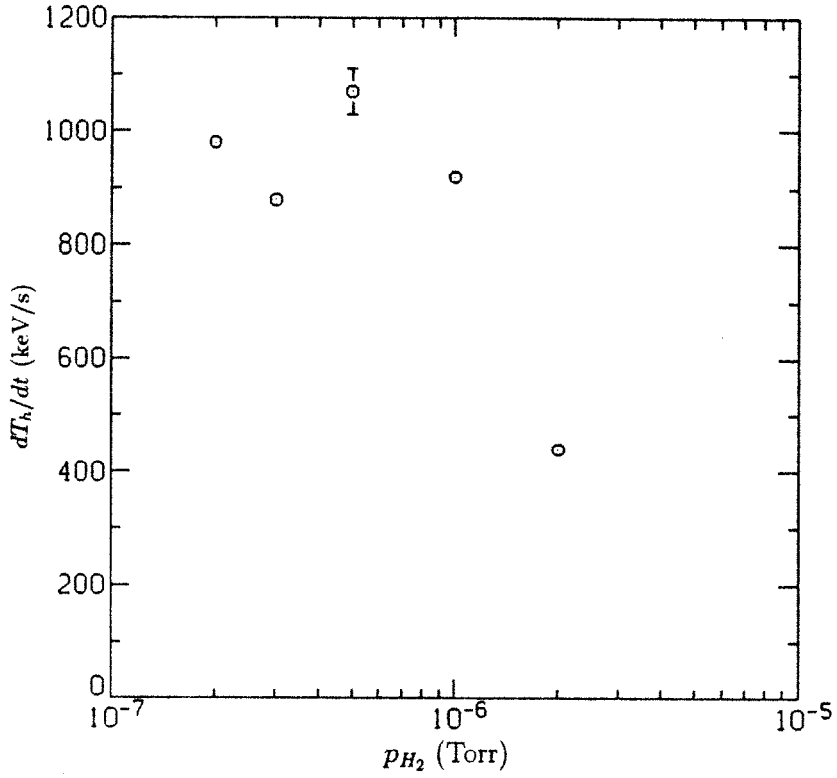

Figure 4.34: Heating rate dT_h/dt for various gas pressures. $B_0 = 3.0$ kG, $P_r f = 2$ kW (cavity O-mode).

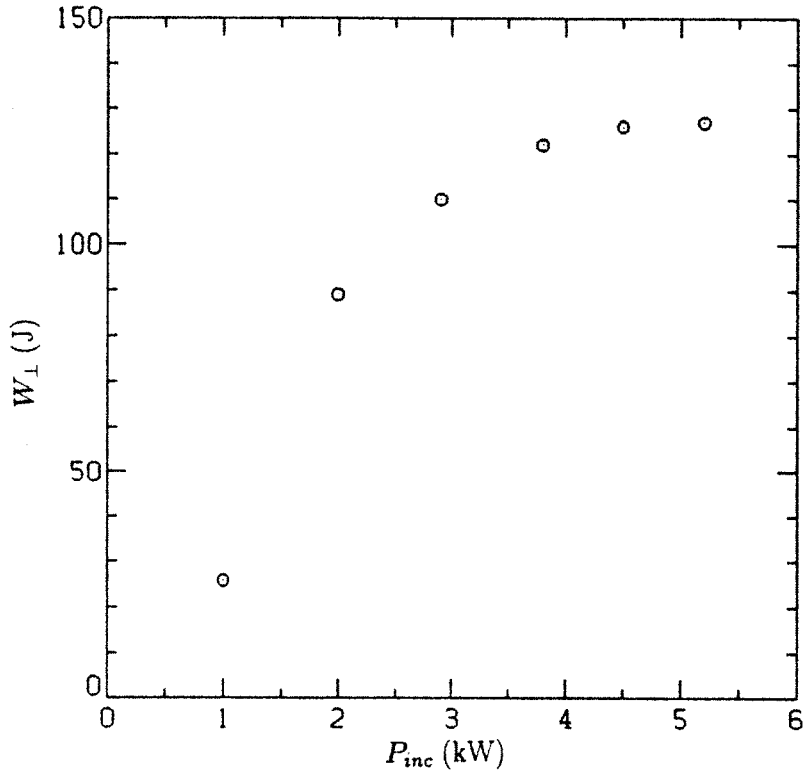

Figure 4.35: Stored energy vs. applied rf power for the optimum conditions of X-mode cavity heating and $p_{H_2} = 2 \times 10^{-6}$ Torr. $B_0 = 3.0$ kG.

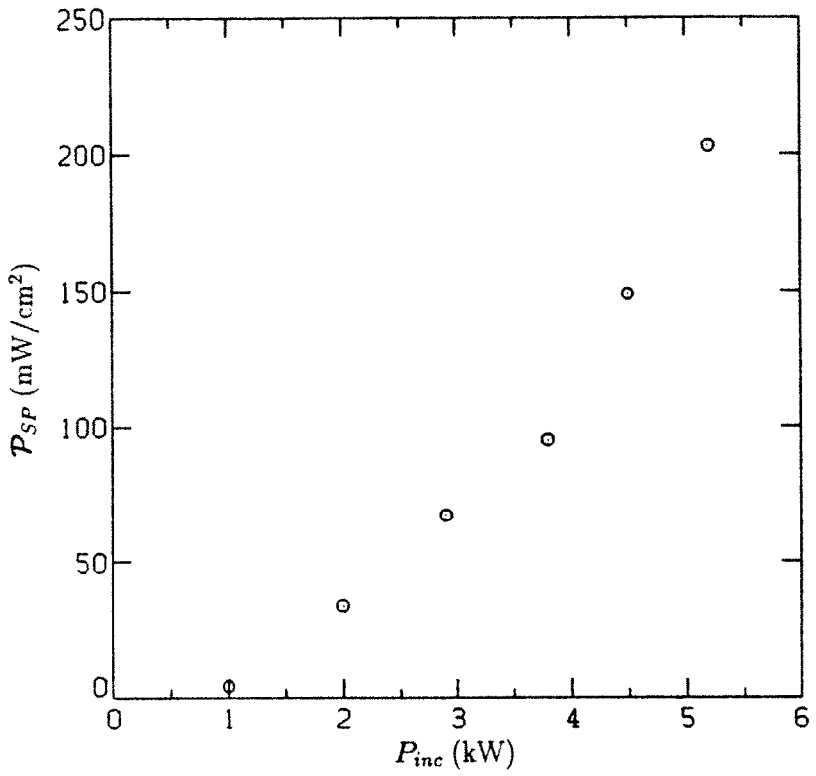

Figure 4.36: Hot electron endloss power density on the central field line vs. applied power.

stored energy remains nearly constant indicates that the global energy loss rate is proportional to power. Confirmation of this is given in Fig. 4.36, where the endloss power density measured by the scintillator probe is seen to strongly increase with rf power. This brings us to the most important result of strong rf diffusion on electron confinement in a mirror: since both heating and loss are results of the rf diffusion process, *strong loss always accompanies strong heating.* You can't win — the harder you drive electrons up in energy along diffusion paths, the harder you drive them into the loss cone along diffusion paths. In fact, this result isn't special to mirrors, but is true for any device which has an enhanced loss region in velocity space which is connected by rf diffusion paths to the confined distribution.

The level at which $W_\perp$ saturates is a function of magnetic field and gas pressure, and is governed by cold electron absorption, because the cold electrons are the fueling source for the hot electrons. Fig. 4.37 shows the steady-state diamagnetic loop signal in a pressure scan. The peak stored energy occurs at roughly the same pressure as the

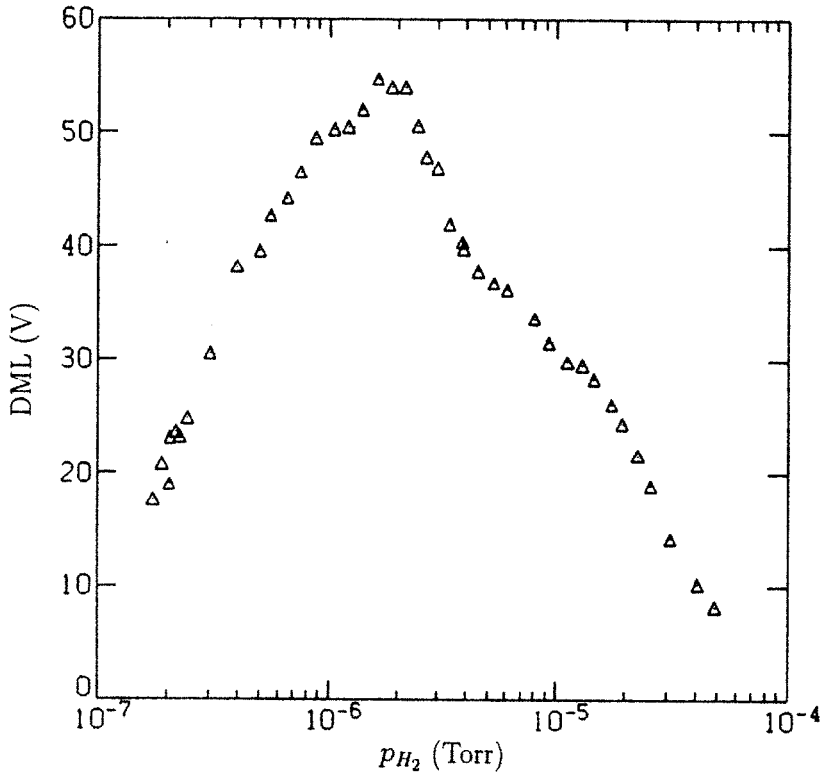

Figure 4.37: Steady-state diamagnetic loop signal in a pressure scan. $P_{rf} = 5$ kW, $B_0 = 3.0$ kG.

peak MRF emission (Fig. 4.14 shows the MRF power for the same scan). Since the microinstability is an indicator of the strength of the cold heating, this is indirect but strong evidence that the largest stored energy is obtained when the hot electron source $n_c\nu_{c\to h}$ is maximized; this is also supported by the fact that the peak in $W_\perp$ is due to hot electron *density*, not temperature. One could argue that the MRF itself is heating the hot electrons, and that is why the two peak at the same place; this seems unlikely when one looks at the plot of $dW_\perp/dt$ for the same scan shown in Fig. 4.33 — the heating rate has a much gentler dependence and does not fall rapidly at the microinstability threshold. Of course, neither does $W_\perp$ itself, but the argument concerns the *source rate*, not MRF *per se* — I believe that directly above the microinstability threshold the cold electrons still provide a strong source to the hots.

The whole story isn't in the source strength, though. One could have a weak source strength with even weaker losses resulting in a large stored energy. This doesn't happen, however — with weak cold absorption, the electric fields are large and the rf diffusion becomes stronger, resulting in stronger rf-induced losses. The data confirming this is shown in Fig. 4.38 where the endloss power density on the central field line is plotted for the same gas pressure scan. One can see that at low pressures the endloss power is much higher, corresponding to the larger electric fields implied by Fig. 4.16. Thus, their are two reasons why the stored energy is maximized when the cold electron absorption is strong: because the source strength is strong, and because the electric fields are reduced.

In summary, this section has shown that rf-induced loss places a limit on the stored energy achieved in the experiment, and that the maximum stored energy results when the cold electron absorption is maximized.

4.6.3 Hot Electron Temperature

In contrast to the stored energy, T_h does not peak in a pressure scan when the cold absorption is maximized; rather, it peaks when the electric field and therefore the rf diffusion strength is maximized. Fig. 4.39 shows the hot electron temperature for the same gas pressure scan as was shown in Fig. 4.37; the behavior is markedly different,

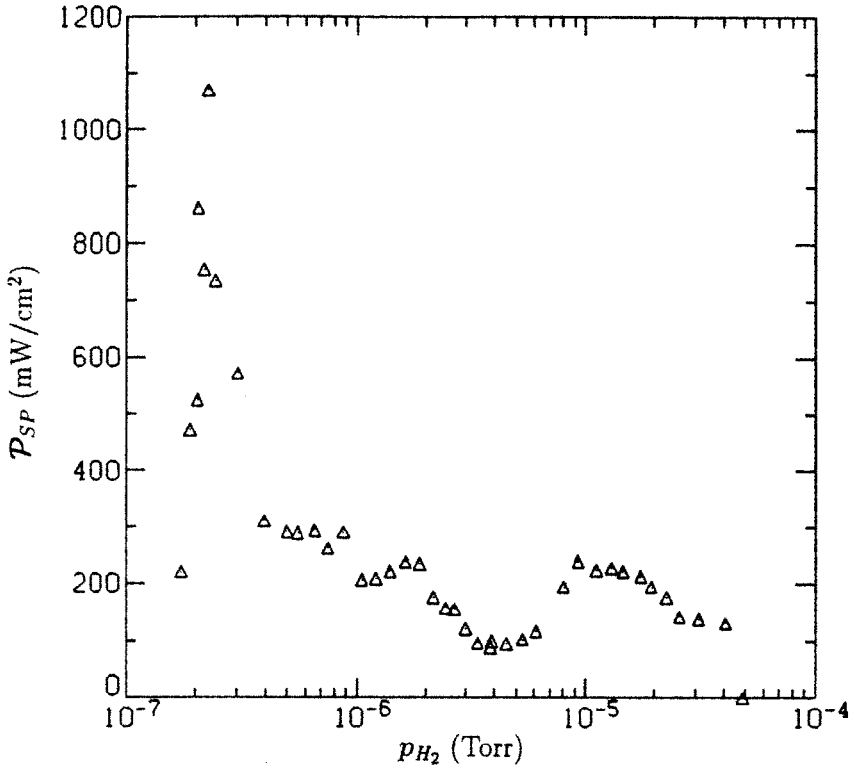

Figure 4.38: Hot electron endloss power density on the central field line in a gas pressure scan.

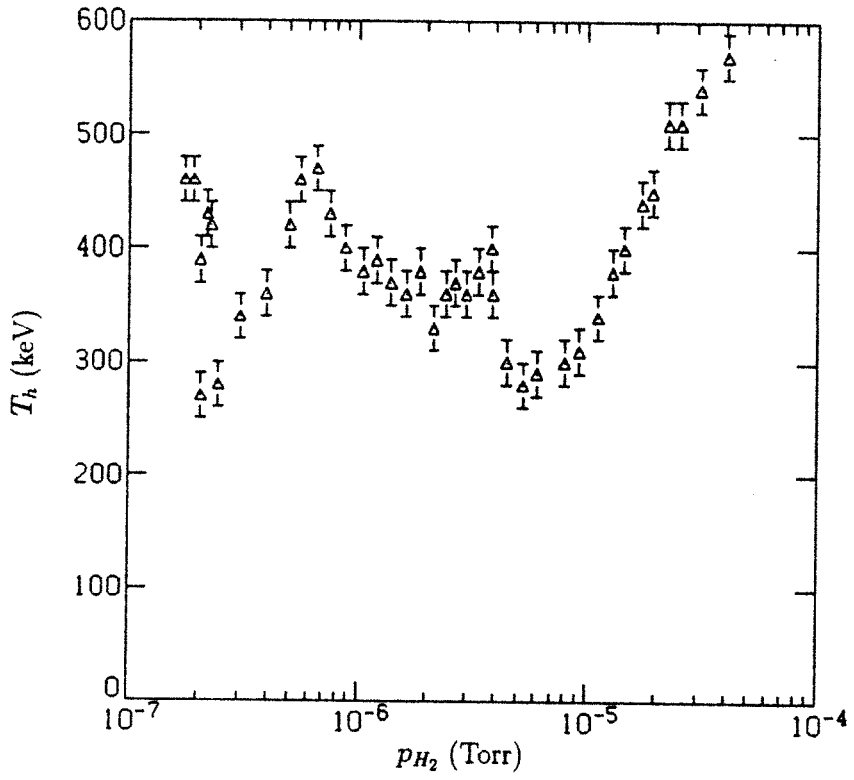

Figure 4.39: Steady-state hot electron temperature in a gas pressure scan.

with T_h smallest at intermediate pressure where $\mathcal{E}^2$ is lowest and rf-induced endloss is also lowest (Fig. 4.38).

In fact, the effects of rf diffusion on T_h can be quite surprising. Fig. 4.40 shows that the hot electron temperature can actually *decrease* with increasing applied power! The scintillator probe confirms that there is, in fact, a degradation in confinement at high energies: Fig. 4.41 shows the ratio of the signals from two channels with different foil thicknesses, for the same scan, and one sees that the loss of high energy electrons is stronger relative to the loss of lower energy electrons as P_{rf} is increased (i.e. the endloss gets hotter). The SMOKE code produces a similar effect on the hot electron temperature: the simulation shown in Fig. 4.20 shows that the rf diffusion induced by the second pulse decreases the average electron energy.

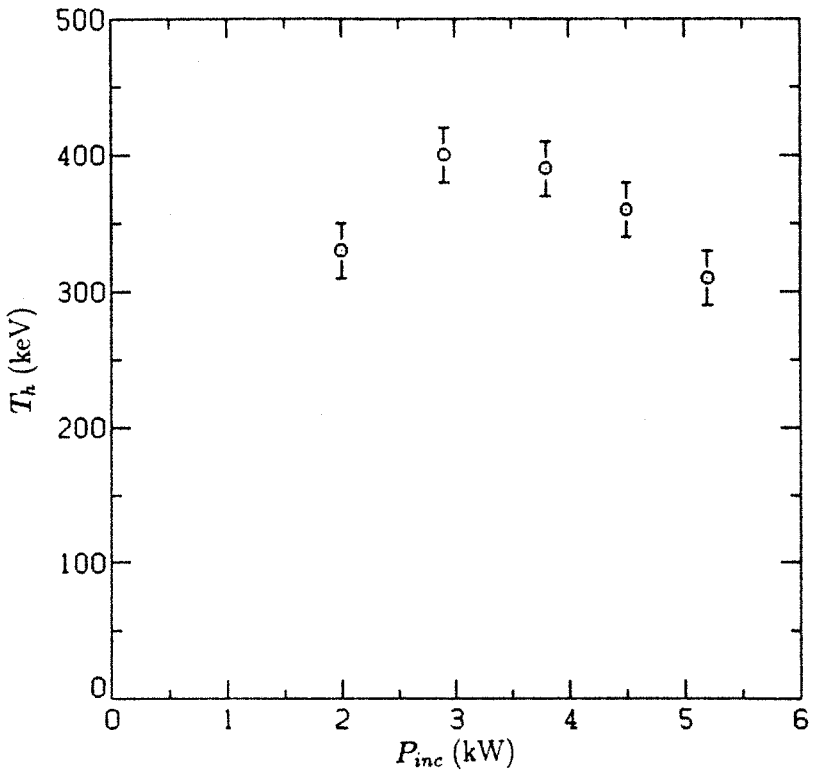

Figure 4.40: Hot electron temperature vs. applied power.

4.6.4 Hot Electron Loss

The best measure of the total power going into the hot electrons is the measure of the total endloss power, since they are equal in steady-state (neglecting the very small loss channels of synchrotron and bremsstrahlung radiation, electron impact ionization, and cold electron drag). In practice, it is extremely difficult to measure the endloss for all of the field lines in Constance, due to the complex geometry and inaccessability to portions of the machine. I have performed measurements of the endloss profile along a very limited set of field lines, those that are in the plane $y = 0$, at one end of the machine ($z = 70$ cm). An assumption is required, therefore, to apply these measurements to the rest of the plasma to obtain an estimate of the total endloss power.

My assumption in analyzing the endloss profiles is that the endloss power density is *constant on a drift surface*. Since electrons drift azimuthally on the time scale of microseconds, the distribution function must be constant on a drift surface. This doesn't

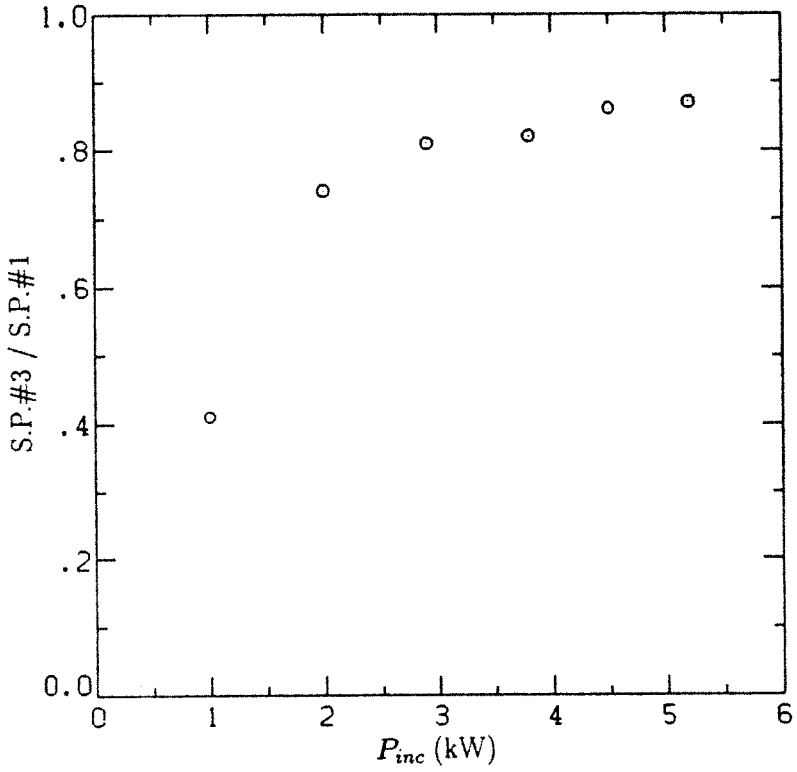

Figure 4.41: The ratio of signals from two scintillator probe channels with entrance foils that have range energies of 30 and 300 keV in an rf power scan.

mean, however, that the *endloss* is constant on a drift surface, since loss can be arbitrarily localized (an analogy is a lake of constant depth with a waterfall at one end). In fact, one expects the endloss *not* to be constant on a drift surface, since the electric field profile isn't. But there seems to be no better guiding assumption to go on. In light of all this, one should regard the results for total endloss power with some skepticism, even though, in my opinion, they are the best that can be obtained with the given data set.

The hot electron endloss is measured with the scintillator probe, which measures power density $\mathbf{j}\bar{E}$. The average energy $\bar{E}$ is independent of position on the field line, but the current density $\mathbf{j}$ varies with magnetic field to satisfy particle flux conservation:

$$\mathbf{j}(\mathbf{r}') = \frac{\mathbf{B}(\mathbf{r}')}{B(\mathbf{r})} j(\mathbf{r}). \tag{4.20}$$

The total endloss current is therefore given by

$$I_{tot} = \int \frac{j(x(\phi(\mathbf{r}')), z)}{B(x(\phi(\mathbf{r}')), z)} \mathbf{B}(\mathbf{r}') \cdot \mathbf{dA}', \tag{4.21}$$

where a drift surface is labeled by the magnetic flux ϕ that it encloses, and I have written the equation to explicitly show that the current measured at a position $(x, 0, z)$ is mapped to another position (x', y', z') according to $\phi(x, 0, z) = \phi(x', y', z')$. The reasons for mapping to a new location are twofold: 1) it is generally useful to map endloss measurements back to the midplane ($z' = 0$), since different diagnostics measure endloss at different z locations, and 2) it is much more convenient to perform the integration at the midplane, because analytic formulae for the magnetic geometry are available at that location. The integration is actually simpler than it looks: since a differential flux element $d\phi = \mathbf{B}(\mathbf{r}') \cdot \mathbf{dA}'$, the integral may be written in 1-d form as

$$I_{tot} = \int \frac{j(x(\phi), z)}{B(x(\phi), z)} \frac{d\phi}{dx'} dx', \tag{4.22}$$

and the job is reduced to a simple two-step process: 1) transforming the measured x locations to the midplane x' locations, and 2) performing a 1-d integration of the

transformed signal with the weighting function

$$w(x') = \frac{1}{B(x(\phi), z)} \frac{d\phi}{dx'}. \tag{4.23}$$

In actuality, $B(x,z) = 0.78B_0$ for all of the measured field lines, slightly simplifying the task. The function $d\phi/dx'$ was obtained by computing $\phi(x')$ for a set of points, performing a spline interpolation and using numerical derivatives; the mapping $x(\phi) \rightarrow x'(\phi)$ was obtained by running the field line code EFFI (Sackett, 1978) for 50 field lines and employing a spline interpolation. Near the axis, $\phi = B_0 \pi r'^2$, so that $w(x') = B_0 2\pi x'$ vanishes at $x' = 0$. Since the profiles actually cover positive and negative values of x, I weight each side with half of the total weighting.

The transformed, unweighted profile and the transformed, weighted profile at the midplane are shown in Figs. 4.42 and 4.43. The profile was measured at $z = 70$ cm. There are a number of important points to make about the endloss profile: 1) it is not symmetric, clearly violating the assumption that the endloss is constant on a drift surface, 2) it peaks at a midplane location of $x' \sim 12$ cm, which is inside of the outermost non-relativistically resonant drift surface at $x' = 17$ cm (called the 'tangent' surface because it is tangent to the $|B| = 3.75$ kG resonance), and 3) there are a significant amount of endloss *outside* of the tangent drift surface. This last point may be a little surprising, since one would expect the source for the hot electrons to be very weak outside of the tangent surface; however, the electric field strength is also strong on the outside since there is no shielding, so the weak source is complemented by strong diffusion. This is analogous, of course, to the previous result that the endloss is largest at lower pressures when the field strength is high, even though the density isn't at its maximum. Another way of stating it is that the energy confinement is poor on the outermost field lines. This is supported by other measurements (Smatlak *et al.*, 1987) that show that the plasma pressure is very low outside of the tangent surface.

Another issue is the amount of endloss produced by MRF. It is generally difficult to separate the MRF-induced endloss from the applied rf-induced endloss because the MRF

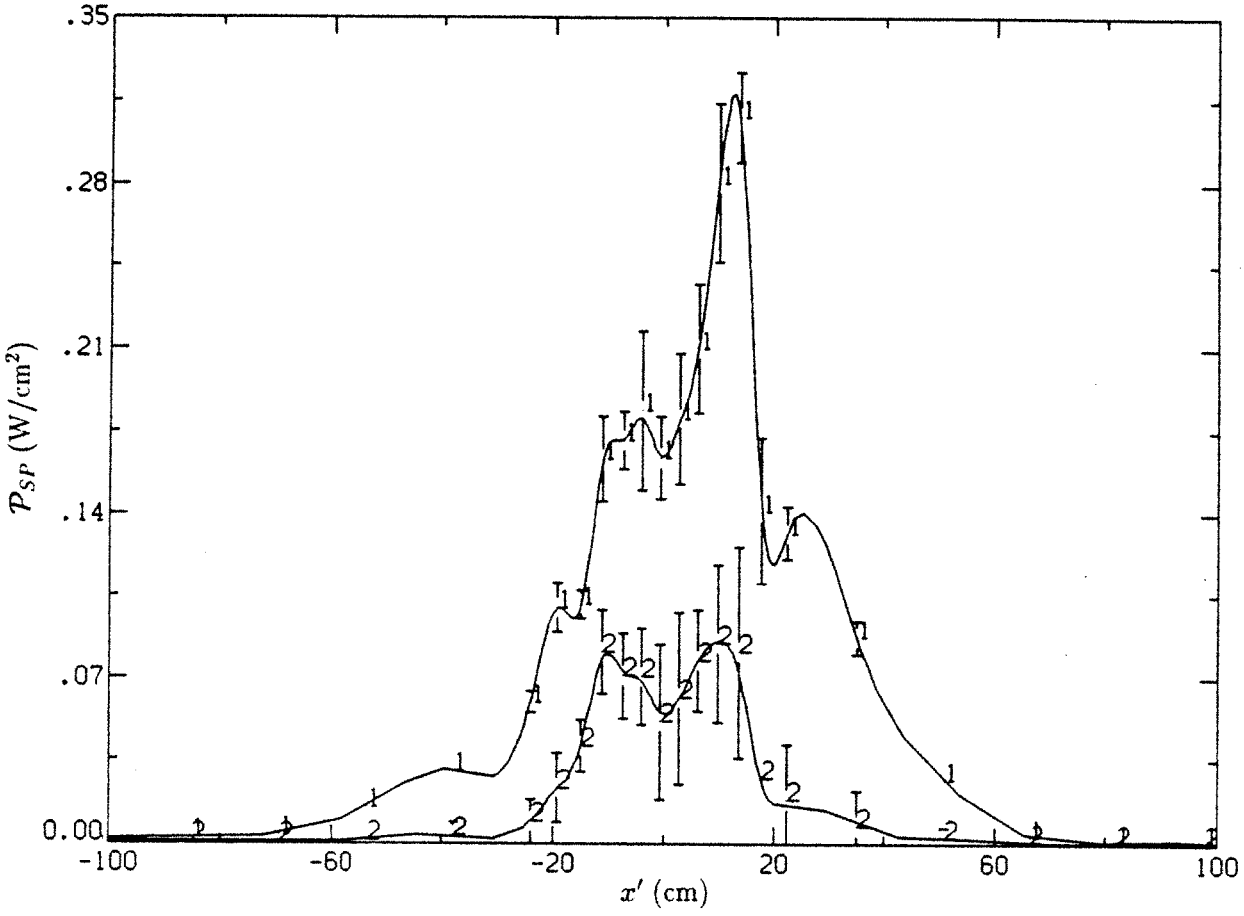

Figure 4.42: A hot electron endloss power density profile transformed to the midplane. Curve 1 is an average over 0.1 s before rf turnoff and curve 2 is an average over 0.1 s afterward. The error bars represent fluctuations due to MRF.

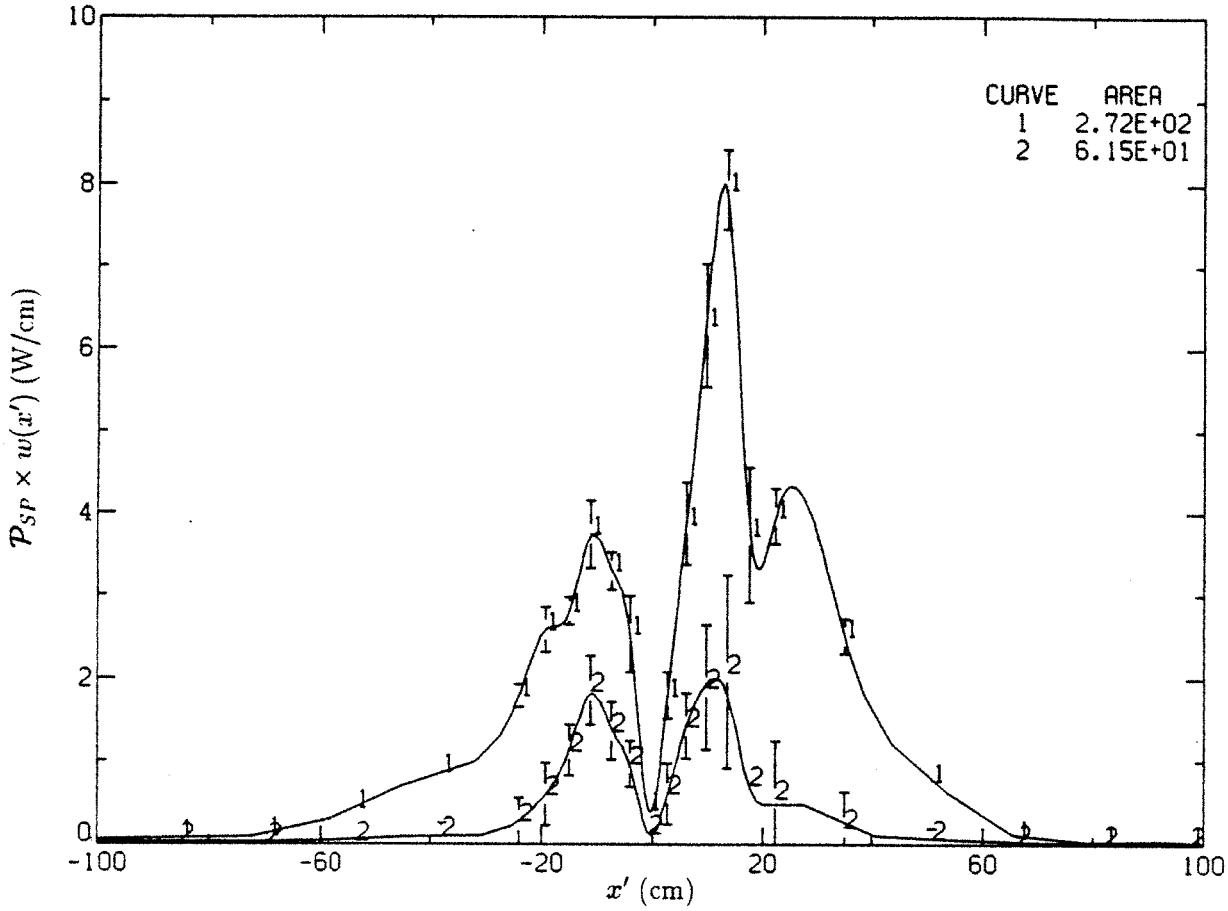

Figure 4.43: The endloss profile transformed to the midplane and weighted by $w(x')$, which has units of length.

P_{inc}	Mode	B_0	p_{H_2}	P_{SP}^{ss}	P_{SP}^{d}	$dW_\perp^d/dt$
4.5	X/Abs	3.0	2×10^{-6}	540±40%	120±40%	375±10%
4.5	X/Cav	3.0	2×10^{-6}	760	90	370
4.5	X/Abs	3.6	2×10^{-6}	110	50	-
2.0	X/Abs	3.0	5×10^{-7}	90	60	130
2.0	X/Cav	3.0	5×10^{-7}	300	55	150
2.0	O/Abs	3.0	5×10^{-7}	20	20	100

Table 4.1: Summary of hot electron power loss measurements. P_{inc} is in kW, all other powers are in Watts. Error estimates indicate instrumental error.

tends to be produced continuously. Certainly, as Fig. 4.38 shows, there is no drastic drop in endloss as the gas pressure is increased above the MRF threshold. At low gas pressures the MRF tends to come in discrete 10 μs bursts at intervals of around 1 ms. Fig. 4.44 shows the scintillator probe signal and the MRF emission digitized on a fast time scale. Analysis of low pressure shots such as this show that the MRF-induced hot endloss accounts for 10–25% of the total. Since the low pressure regime produces the strongest total endloss, this most likely represents the strongest MRF-induced endloss power in the experiment.

The integral under the weighted endloss profile gives an estimate of the total endloss power, although I must emphasize that it is an *estimate* given the assumptions made in the analysis. Nevertheless, it is worthwhile looking at the result in the context of other measurements to get an estimate of the power absorbed by the hot electrons. This is done in the next section.

4.6.5 Power Absorption

There are at present only two measurements of total electron power loss: the integrated scintillator probe endloss profile, and the diamagnetic loop decay (the calibration of the scintillator probe is described in Appendix B). The results for a number of conditions are shown in Table 4.6.5, where the powers from the scintillator probe are given for the steady-state phase (P_{SP}^{ss}) as well as the first 0.1 s of the decay (P_{SP}^{d}), and the loop decay power $dW_\perp^d/dt$ is given for the same portion of the decay. The endloss decay power is a factor of 2–5 lower than the diamagnetic loop decay power. Although there are errors

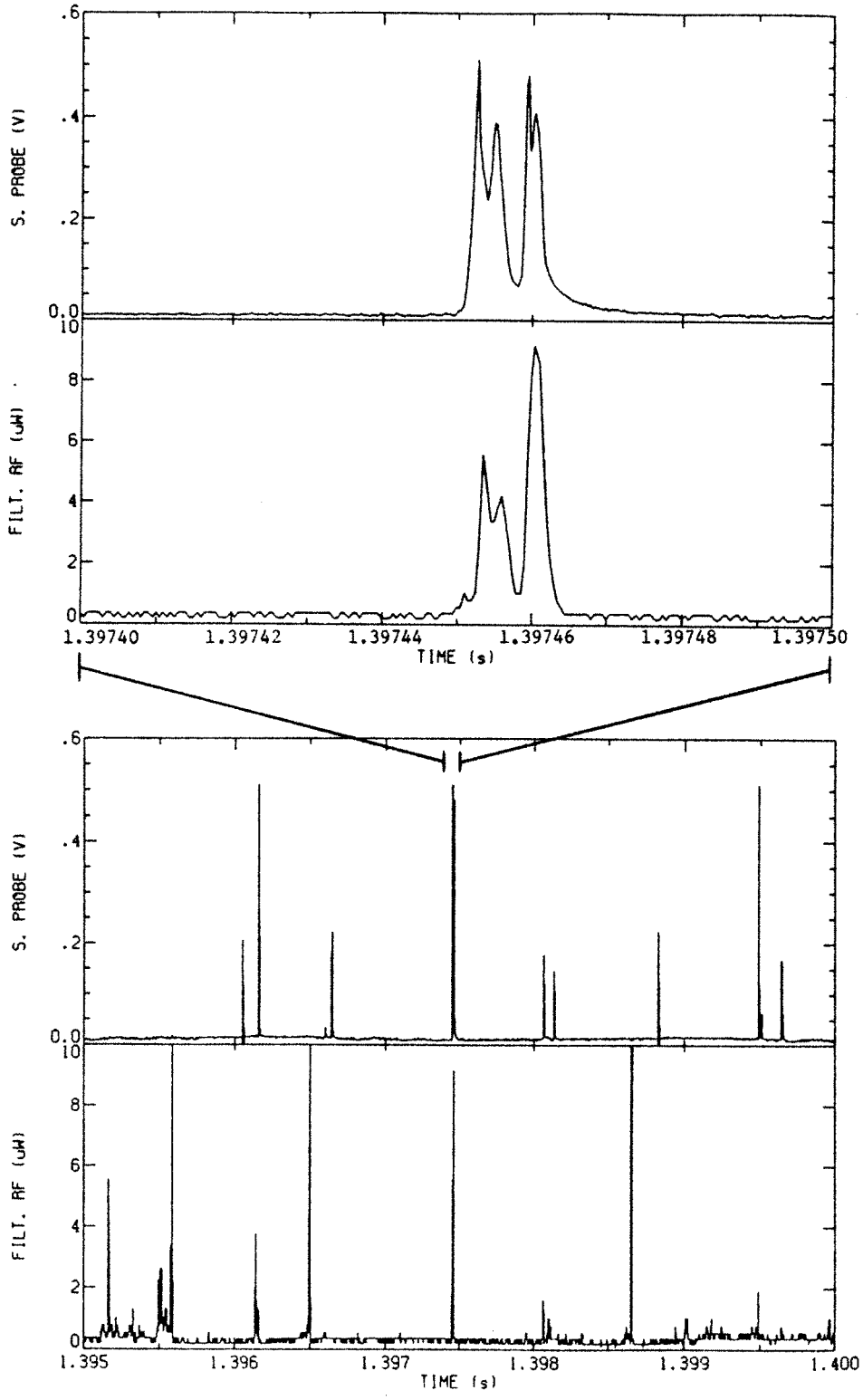

Figure 4.44: Hot electron endloss and an MRF burst for a shot at low gas pressure. The unfiltered rf diode signal is zero between bursts (a positive offset was added).

involved in the calibration of the scintillator probe, it is doubtful that they can fully account for the discrepancy; it is much more likely, and completely reasonable, that the discrepancy is due to non-uniformity of endloss on a drift surface, or asymmetry in the loss between the two ends. The fact that the discrepancy varies with plasma conditions also supports this; a systematic error would result in a fixed ratio between the two numbers. On the other hand, the diamagnetic loop decay is also sensitive to pitch-angle relaxation (decreasing $W_\perp$ with increasing $W_\parallel$) which occurs in the decay. The end result is that the true decay power is probably somewhat less than $dW_\perp^d/dt$, but not nearly as much as indicated by the endloss measurement.

If one goes with the diamagnetic loop endloss power as the true value, one can get the total endloss power in steady-state by assuming that the endloss profile has the same structure on a drift surface during the steady-state phase as during the decay phase. This is not a particularly good assumption, since the steady-state loss is determined by the rf fields which certainly vary on a drift surface. Nevertheless, there is a clear qualitative difference between the absorber and cavity experiments, with this method giving an estimate of $P_{ss} = 1.8$ kW, or $0.4P_{inc}$, in the former case and 3.1 kW, or $0.7P_{inc}$, in the latter case for the data shown in the top two rows of Table 4.6.5. The stored energy ($W_\perp = 120$ J) and decay power are the same for the two cases, indicating that the stronger diffusion produced in the cavity experiments, which is also seen in the buildup phase as discussed in Section 4.5.6, only results in stronger endloss. The energy confinement times, given by $W_\perp/P_{ss}$, are $\tau_E = 70$ ms for the absorber case and 40 ms for the cavity case.

Of course, not all of the total power comes out in endloss; another loss channel is the whistler rf emission. Since the MRF is only measured at the location of the waveguide, it is difficult to estimate the total MRF power. If one assumes that the emission is isotropic, and the results of Rich Garner (1986) indicate that it is, one can get an estimate by multiplying the waveguide power by a factor which takes into account the solid angle that it subtends; this factor is roughly 10,000. For the absorber case given in the top row of Table 4.6.5, the total emission is estimated to be 800 W, but one should keep

in mind that this could easily be off by at least a factor of two. The MRF power is approximately the same in the cavity case, in agreement with the notion that the cavity fields aid diffusion of hot electrons but have no effect on the cold electrons.

Including the whistler rf emission, then, the total absorption estimate is 60% for the absorber case and 90% for the cavity case at the optimum parameters of $P_{rf} = 5$ kW, $B_0 = 3.0$ kG, and $p_{H_2} = 2 \times 10^{-6}$ Torr.

The main results on heating and confinement presented in this chapter can be summarized in a single statement: *rf diffusion strongly limits confinement of hot electrons in a micro-unstable, ECRH mirror plasma.* This has been seen in practically all the results, and produces effects like the shortened axial pressure profile, the strong endloss at low gas pressures, the turnover of T_h with increasing rf power, and, most importantly, the fixed stored energy limit. These effects are not unique to mirror plasmas, or even to electron heating, and should be considered in any rf-heated device, whether it be a tokamak or a bumpy torus, with ECRH or ICRH. The following chapter summarizes the results of this work, discusses their application to other devices, and points to remaining questions that warrant further study.

Chapter 5

Conclusions

The results presented in this dissertation may be summarized as follows:

Endloss produced by rf diffusion is the dominant loss mechanism for hot electrons in strongly-heated plasma regimes, resulting in an energy confinement time of 40 ms in the case of cavity heating with 4.5 kW of incident power, as compared with the collisonal scattering time of 350 ms. Since both heating and rf-induced endloss are manifestations of rf diffusion, they follow one another — the stronger the heating, the stronger the loss. This results in the observed confinement limit in the device: above 2 kW, increased rf power merely results in a more rapid attainment of equilibrium at a fixed stored energy. Rf-induced loss increases relative to collisions with increasing hot electron energy; a significant portion is due to second and third harmonic resonances, just as significant heating results from higher harmonics.

The hot electron temperature is not limited by loss of adiabaticity, as has been proposed, but is actually limited to values for which velocity-space diffusion due to μ-breaking is comparable to or less than that due to collisions. The results indicate that, in fact, the dominant diffusion mechanism is rf diffusion, and it governs the equilibrium temperature in most regimes. In fact, the experiment shows that T_h can actually *decrease* with increasing rf power in strong rf regimes, due to the strong rf-induced loss of high energy electrons. In this situation, the endloss continues to increase in energy, verifying that the T_h degradation is due to poorer confinement, rather than to any anomalous degradation of diffusion to high energies.

Single-pass absorption is limited to less than 60%. In the presence of cavity fields, total absorption of up to 90% is observed, and the improved heating is attributed to the effect of the broad spatial rf profile of cavity fields, although the possibility that otherwise unseen super-adiabatic effects are playing a role cannot be ruled out. The confinement limit still remains, however: in the cavity case, the loss is correspondingly larger, and the resulting stored energy is no different from the stored energy obtained in the absorber case.

Super-adiabatic effects are not clearly evident in the experiments performed in this research. The observations leading to this conclusion are:

- There is no observed decrease in the heating rate as the electron population is heated from low temperatures (10 keV), at which super-adiabatic effects are not expected to play a role, to the high temperatures reached in steady-state (400 keV) which are well above the theoretical barrier to strong diffusion.

- No 'warm' component ($T \sim 1$ keV) of significant density is observed. Although it is known that the strongly rf-driven, magnetically-confined electrons in this energy range are whistler micro-unstable, there appears to be no strong barrier which prevents them from being rapidly heated to high energies.

- Strong endloss observed in 'second-pulse' experiments, in which the cold plasma is removed to observe the effect of rf diffusion on the hot electron component alone, can be reproduced by an rf Fokker-Planck code only when the fully stochastic rf diffusion tensor is used.

If super-adiabaticity exists, then a randomizing mechanism is acting to reduce or eliminate its effect. The leading possibility is the effect of cavity fields, although the data do not conclusively show them to be playing such a role. It can certainly be concluded, however, that super-adiabatic effects do not place a severe limit on diffusion.

Collisional loss processes are consistent with the standard theoretical model.

Whistler microinstability plays two key roles in strong rf regimes:

- It can be a large power loss channel, producing rf emission of up to 20% of the total applied power.
- It can produce a significant portion (up to 25%) of rf-induced hot electron endloss.

Furthermore, the whistler microinstability is *inherent* to regimes of strong hot electron production, because the very source for the hot electrons is the cold electrons which have been rf-diffused up in energy. The stronger the heating of the cold electrons, the stronger the source for the hot electrons, *and* the stronger the microinstability. In fact, the maximum hot electron density tends to occur at the conditions for which the microinstability is maximum.

Cold electron absorption exhibits the generic features of a simple slab model but differs in that the spatial deposition is strongly dependent on the mirror ratio at resonance, an effect which is absent in the slab model but is a natural result of cyclotron resonance in a mirror field. In fact, the cold electrons are heated most strongly near the intersection of the resonant $|B|$ surface and the surface of field-line minima; this intersection traces out a curve which reproduces the baseball-seam shape of the magnet. Since the cold electrons are the source for the hots, the hot electron density and endloss peak on field lines for which cold electron heating is strongest.

The effect that rf diffusion has on confinement is clearly very strong in a mirror plasma. Related effects occur in other devices, such as bumpy tori and tokamaks. Since these devices have closed field lines, losses are enhanced by rf diffusion through its interaction with radial transport: particles are diffused into regions of velocity space which have poor confinement, and they are then lost if spatial transport out of the plasma proceeds faster than diffusion back into more well-confined regions of velocity space.

Of the two devices mentioned, this effect is worse for bumpy tori. In the EBT experiment (Batchelor *et al.*, 1987), high energy electrons, with energies well above the ambipolar potential ϕ, have predominantly magnetic drifts and are weakly coupled to the colder bulk electrons, just as in the case of hot electrons in Constance. These electrons

are poorly confined if they are located near the trapped/passing boundary in velocity space, equivalent to the loss cone in a single mirror. Rf diffusion degrades their confinement in much the same way as it degrades confinement of hot electrons in Constance. Particle balance in EBT is dominated by the 'warm' electrons whose drifts are strongly affected by the spatial structure of ϕ. When the magnetic drift cancels the $\mathbf{B} \times \nabla\phi$ drift, the neoclassical step size can exceed the size of the plasma: the direct loss of this class of electrons accounts for 60% of the particle loss and 80% of the energy loss, and rf diffusion is the mechanism which fuels the lossy region in velocity-space.

Electron transport in tokamaks is well above neoclassical levels, and it is doubtful that rf diffusion into regions with poor neoclassical confinement has a significant effect in ECH experiments. The enhanced transport of ripple-trapped ions due to ICH has been theoretically investigated (Chen *et al.*, 1987) and may be significant at high energies, but it does not appear to be a strong effect in present-day devices. However, if strongly-heated anisotropic distributions are produced in future high power ICH experiments, rf diffusion can be expected to play a role in the enhancement of transport.

There are a number of problems related to rf velocity-space diffusion that this thesis leaves unanswered. Most outstanding is the question of whether the stronger diffusion produced in the cavity experiments is due to a broadened rf profile or due to a reduction of super-adiabatic effects. An important theoretical issue is that of cold electron heating: it has never been treated in a self-consistent fashion which incorporates the effects of microinstability rf emission and rf-induced endloss on ambipolar potential formation, and the rate $\nu_{c \to h}$ at which cold electrons fuel the hot population has never been modeled. Finally, the rf Fokker-Planck simulations presented here have not quantitatively reproduced the observed hot electron parameters — a calculation of hot electron heating that incorporates cavity rf fields, including the broad-band microinstability spectrum, and takes into account the anisotropic distribution of warm electrons is required to generate heating rates, endloss powers, and equilibrium temperatures than can be compared with the observations.

Appendix A

X-Ray Spectroscopy

In this appendix, I summarize the calculation of plasma bremsstrahlung spectra and the response of the x-ray detectors which is used to compare the experimental spectra to chosen electron distribution functions. In the first section, the calculation of the pure spectrum is described; in the second section, the method of calculating the response function for the NaI(Tl) and Ge detectors is described; and in the third section, I describe the technique which is used in making the comparison between the experimental spectra and the theoretical detector-modified spectra.

A.1 Plasma Bremsstrahlung

A hot electron in a plasma produces bremsstrahlung x-rays due to Coulomb collisions with atoms, ions, and electrons. Bremsstrahlung from electron-atom collisions is identical to that from electron-ion (e-i) collisions for x-rays which are well above the ionization potential of the atom, as is the case here, where $\hbar\omega/\phi_{ion} \geq 100$. The relativistic Born approximation cross-section for e-i bremsstrahlung is the Bethe-Heitler cross-section (Heitler, 1954):

$$\begin{aligned}\frac{d\chi}{d\omega} &= \frac{Z^2 a_0^2}{137}\frac{p}{p_0}\left\{\frac{4}{3} - 2E_0E\frac{p^2+p_0^2}{p^2p_0^2} + \mu^2\left(\frac{\epsilon E}{p_0^3} + \frac{\epsilon E_0}{p^3} - \frac{\epsilon\epsilon_0}{p_0 p}\right) + \right. \\ &+ L\left[\frac{8}{3}\frac{E_0E}{p_0p} + \frac{k^2}{p_0^3p^3}(E_0^2E^2 + p_0^2p^2) + \right. \\ &\left.\left. + \frac{\mu^2 k}{2p_0p}\left(\frac{E_0E+p_0^2}{p_0^3}\epsilon_0 - \frac{E_0E+p^2}{p^3}\epsilon + \frac{2kE_0E}{p^2p_0^2}\right)\right]\right\}, \end{aligned} \tag{A.1}$$

where natural units ($\hbar = c = 1$) are used, Z is the ion charge, a_0 is the Bohr radius, μ is the electron mass, p_0, E_0 are the initial electron momentum and energy (including μ), p, E are the final momentum and energy, $k = \omega = E_0 - E$ is the momentum and energy of the emitted photon, and L, ϵ_0, and ϵ are given by:

$$\begin{aligned} L &= \ln \frac{p_0^2 + p_0 p - E_0 k}{p_0^2 - p_0 p - E_0 k} \\ &= 2 \ln \frac{E_0 E + p_0 p - \mu^2}{\mu k}, \end{aligned} \tag{A.2}$$

$$\begin{aligned} \epsilon_0 &= \ln \frac{E_0 + p_0}{E_0 - p_0} \\ &= 2 \ln \frac{E_0 + p_0}{\mu}, \end{aligned} \tag{A.3}$$

$$\epsilon = 2 \ln \frac{E + p}{\mu}. \tag{A.4}$$

The total cross-section (integrated over emission angle) has been used because the angle dependence of the spectrum is weak for a mirror plasma (England and Haste, 1973), and the inclusion of an angular calculation would considerably increase the CPU time required for the calculation. This cross-section has much simpler forms for the non-relativistic and super-relativistic cases, but since the Constance hot electrons are in an intermediate range ($T \sim 500$ keV), the full cross-section has been used.

A correction to the Born approximation, due to Sommerfeld, may be included (Heitler, 1954). This correction is in the form of a simple function $S(E_0, E)$ which multiplies the form for $d\chi/d\omega$ shown above, and is given by

$$S(E_0, E) = \frac{\xi}{\xi_0} \frac{1 - e^{-2\pi\xi_0}}{1 - e^{-2\pi\xi}}, \tag{A.5}$$

where $\xi_0 = 1/(137 v_0)$ and $\xi = 1/(137 v)$. S deviates from unity for large ξ_0 (low energy incident electrons) or large ξ (hard photons, where most of the electron's energy is given to the photon). I have included the Sommerfeld correction in general, although it produces a noticable effect on the x-ray spectrum only for photon energies below 1 keV or so.

The power emitted by an electron in the range $d\omega$ is given by

$$n_i v_0 \frac{d\chi}{d\omega} d\omega,$$

and the spectral power per unit volume emitted by electrons with a distribution function $f(E_0)$ is given by

$$\begin{aligned} \frac{dI}{d\omega d^3r} &= \int_{\mu+\omega}^{\infty} dE_0 n_e n_i v_0 \frac{d\chi}{d\omega} 4\pi p_0 E_0 \int_0^1 d\lambda f(E_0, \lambda), \\ &= \int_{\mu}^{\infty} dE n_e n_i v_0 \frac{d\chi}{d\omega} 4\pi p_0 E_0 \int_0^1 d\lambda f(E+\omega, \lambda), \end{aligned} \tag{A.6}$$

where the integration over pitch-angle $\lambda = \cos\theta$ is shown explicitly and $f(E, \lambda)$ is normalized so that

$$\int d^3p f(\mathbf{p}) = \int_0^{\infty} dE 4\pi p E \int_0^1 d\lambda f(p, \lambda) = 1. \tag{A.7}$$

Finally, the intensity spectrum incident upon a detector is

$$\frac{dI}{d\omega} = \int d^3r \frac{\Omega(\mathbf{r})}{4\pi} \frac{dI}{d\omega d^3r}, \tag{A.8}$$

where $\Omega(\mathbf{r})$ is the solid angle spanned by the detector as seen from the point $\mathbf{r}$, and $dI/d\omega d^3r$ is a function of $\mathbf{r}$ if f is. For a Maxwellian distribution,

$$f(E+\omega) = \exp(-\omega/T)\exp(-E/T)$$

, and the spectrum has primarily an $\exp(-\omega/T)$ dependence, deviating at low energies $\omega < T/2$ (see Figure A.1). In actual fact, the x-ray pulse height spectrum corresponds to the photon *number* spectrum

$$\frac{dN}{d\omega} = \frac{1}{\omega} \frac{dI}{d\omega},$$

but it is an easy matter to convert the experimental number spectrum to an intensity spectrum.

The Born cross-section for e-e bremsstrahlung is an exceedingly complicated function, and the calculation of the spectrum is laborious (Swanson, 1967). However, the e-e spectrum differs from the e-i spectrum mostly in magnitude, but not in shape: Figure A.1

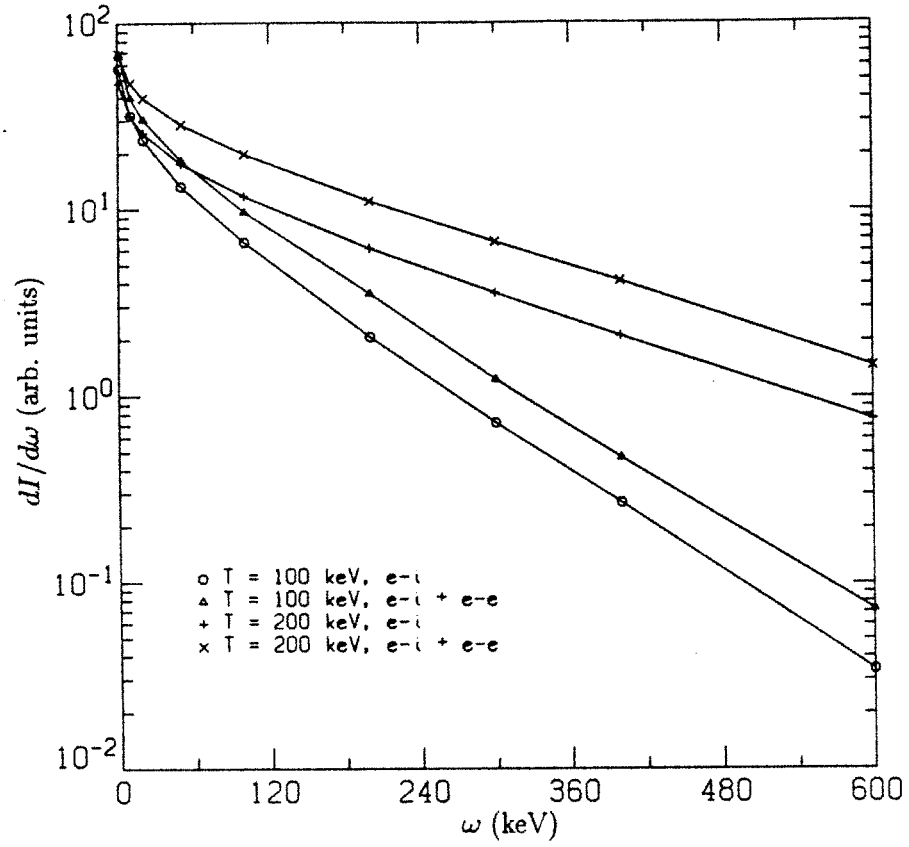

Figure A.1: Bremsstrahlung spectra for a Maxwellian electron distribution. Data from Maxon, Phys. Rev. A 5, 1630 (1972).

shows the e-i and total (e-i + e-e) bremsstrahlung spectra for a Maxwellian electron distribution and $Z = 1, n_i = n_e$. One sees that the total spectrum has roughly twice the intensity of the e-i spectrum, but a similar shape. In addition, $\sum Z_t^2 n_t > n_e$ in the experiment, where the targets n_t are neutral H atoms, protons, and Ar and Ti impurities, so that the e-i bremsstrahlung is enhanced relative to e-e. Because of these two facts, e-e bremsstrahlung is not expected to affect the shape of the spectrum, and I have neglected it in the calculation of x-ray spectra.

A.2 Detector Response

A.2.1 NaI(Tl) Detector

A thallium-doped sodium iodide, or NaI(Tl), x-ray detector is a scintillation detector: an x-ray entering a NaI(Tl) crystal scatters and slows down, giving up its energy to the crystal in the form of scintillation photons, due to the process of photo-excitation. The x-ray may also undergo Compton scattering and electron-positron pair production. The scintillation photons are collected by a photo-multiplier tube, and the pulse is recorded by a pulse-height analysis system.

The attenuation coefficients for the three processes are shown in Figure A.2. Compton scattering can lead to the recording of an energy lower than that of the photon because a photon may scatter and carry some energy out of the crystal. In addition, the probability that the photon may transverse the crystal without an interaction becomes large if the attenuation length μ^{-1} is comparable or larger than the crystal dimensions. All of this may be summarized by a detector response function

$$R(\omega, \omega'') = \eta(\omega) \int_0^\omega D(\omega, \omega') g(\omega', \omega'') d\omega', \tag{A.9}$$

for which the detector-modified spectrum is given by

$$\frac{dI}{d\omega''} = \int_0^\infty d\omega \frac{dI}{d\omega} R(\omega, \omega''). \tag{A.10}$$

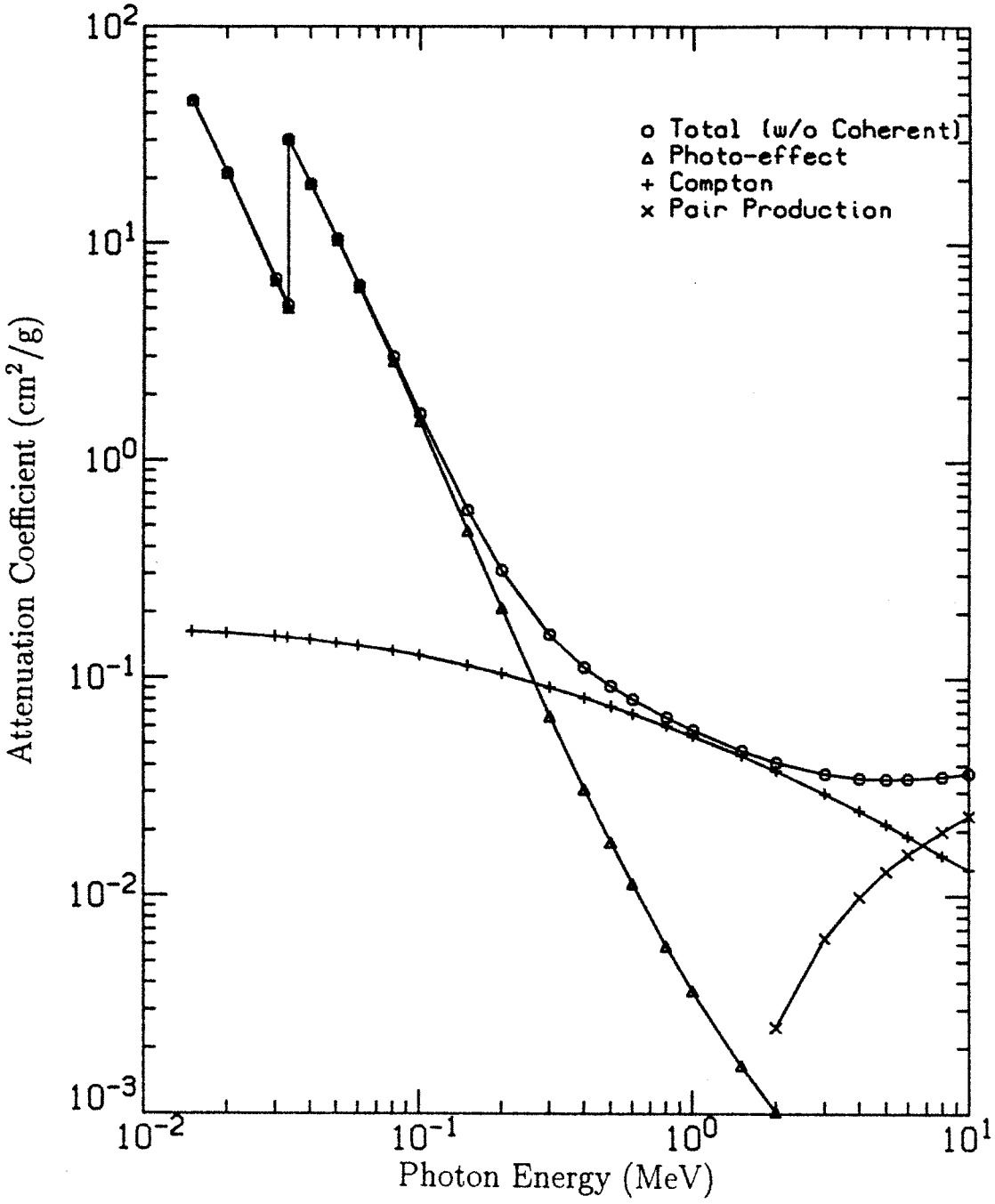

Figure A.2: X-ray attenuation coefficients for NaI(Tl). Data from Hubbell, J.H. Nat. Bur. Stds. NSRDS-NBS 29 (1969).

In Eq. A.9, $\eta(\omega)$ is the probability that the photon has at least one interaction, $D(\omega,\omega')d\omega'$ is the probability that an interaction deposits an energy between ω' and $\omega'+d\omega'$, and $g(\omega',\omega'')d\omega''$ is the probability that the deposition of energy ω' is recorded between ω'' and $\omega''+d\omega''$.

The function $g(\omega',\omega'')$ is a normal distribution arising from the imperfect resolution of the photomultiplier tube:

$$g(\omega',\omega'') = \frac{1}{\sigma\sqrt{2\pi}} \exp -\frac{(\omega'-\omega'')^2}{2\sigma^2}. \tag{A.11}$$

The resolution is $r(\omega') = W(\omega')/\omega'$, where $W = 2\sigma\sqrt{2\ln 2}$ is the full width at half maximum. The resolution is measured to be $r_{661} = 7\%$ for the standard $\omega' = 661$ keV Cs^{137} photon. A statistical argument would predict a dependence on energy $r \propto \omega'^{-1/2}$. However, experiments (Berger and Seltzer, 1972) show that r varies as $\omega'^{-1/3}$, so that σ may be written

$$\sigma(\omega') = r_{661}\left(\frac{661}{\omega'}\right)^{1/3} \frac{\omega'}{2\sqrt{2\ln 2}}. \tag{A.12}$$

Berger and Seltzer (1972) used a Monte-Carlo technique to determine $D(\omega,\omega')$, which has the form:

$$\begin{aligned} D(\omega,\omega') &= C(\omega,\omega') + P_0(\omega)\delta(\omega-\omega') + P_1(\omega)\delta(\omega-\omega'-mc^2) + \\ &\quad + P_2(\omega)\delta(\omega-\omega'-2mc^2) + P_3(\omega)\delta(\omega'-\omega_f). \end{aligned} \tag{A.13}$$

C is the partial absorption continuum, P_0 is the photopeak fraction, P_1 and P_2 are single- and double-annihilation peak fractions, and P_3 is the iodine K-shell fluorescence peak fraction, with $\omega_f = 29$ keV; these are plotted in Figure A.3 (I have included data for P_3 at low energies from Fioratti and Piermattei, 1971). I have used spline fits to the tabulations of C and P_n which were calculated for a $3'' \times 3''$ detector with a broad parallel beam of incident radiation, similar to the experimental situation. The overall response to a flat input spectrum with a value of unity is shown in Fig. A.4. The low energy excess is due to partial absorption of high energy photons.

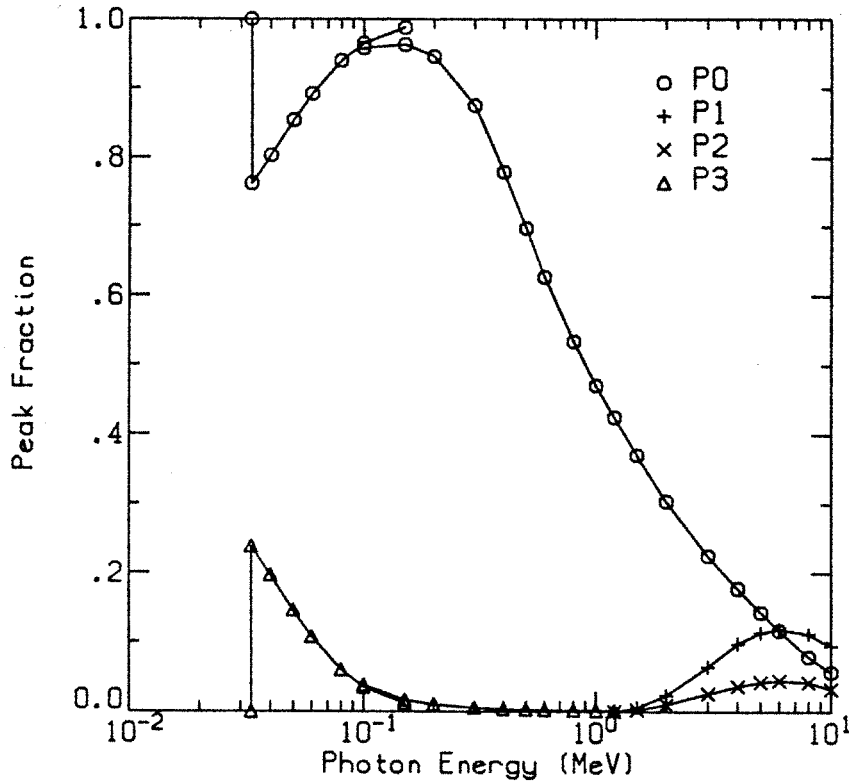

Figure A.3: The coefficients in the expression for $D(\omega, \omega')$. Data from Berger, MJ and Seltzer, SM (1972) NIM 104, 317 and Fioratti, MP and Piermattei, SR (1971) NIM 96, 605.

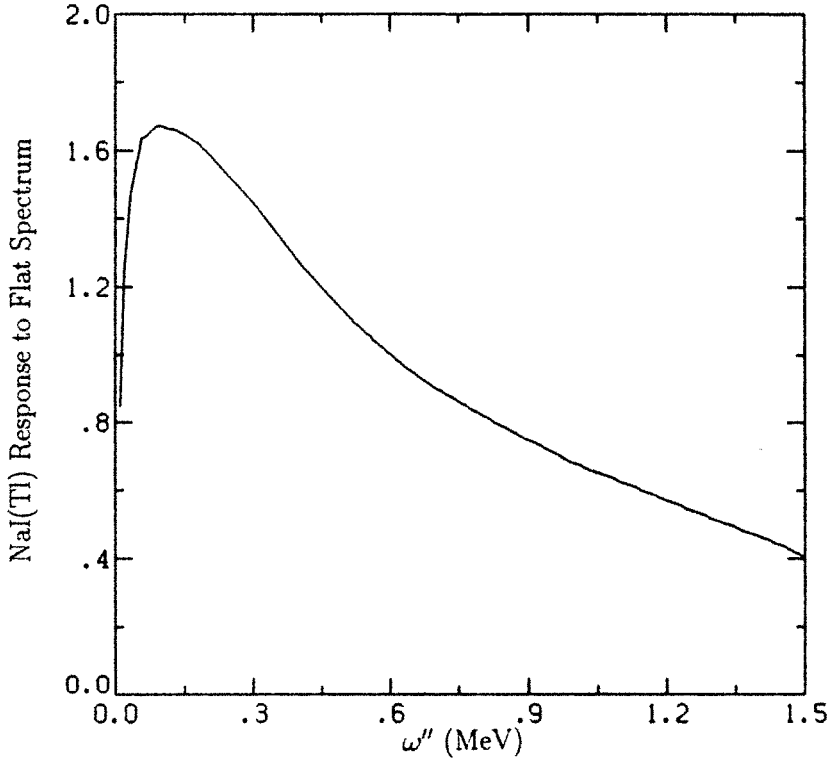

Figure A.4: The NaI(Tl) detector response to a flat input spectrum including attenuation due to 88" of air and 0.020" of aluminum between the plasma and the detector.

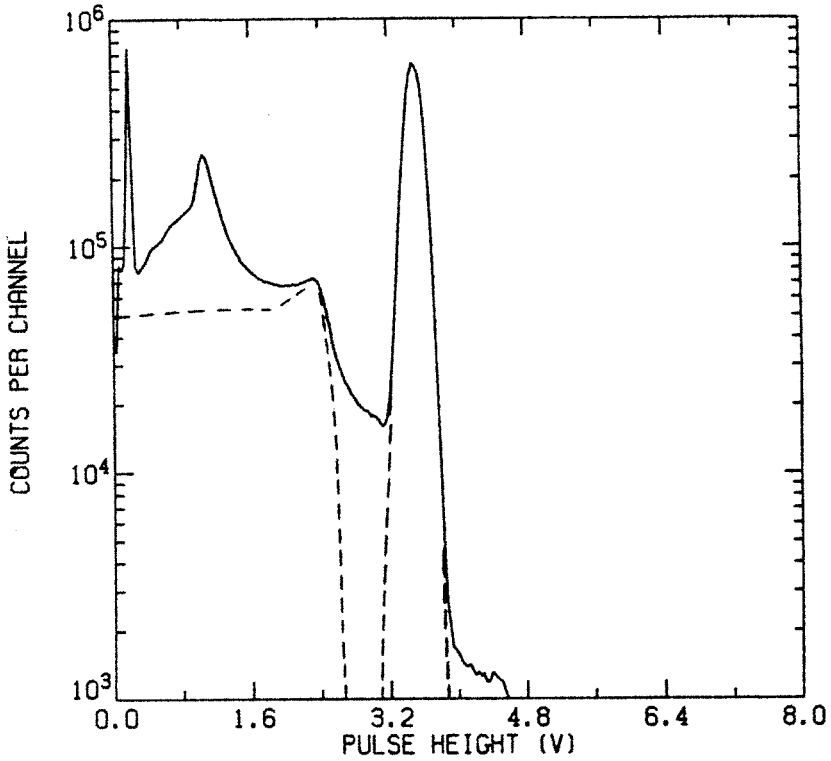

Figure A.5: Cs^{137} pulse-height distribution (solid curve) and calculated detector response (dotted curve). The source was placed directly in front of the detector.

As a means of comparison, Fig. A.5 shows a pulse-height distribution for a Cs^{137} source placed directly on the $3'' \times 3''$ NaI(Tl) detector and the corresponding calculated detector response with $\omega = 661$ keV. The experimental spectrum has a larger low-energy portion due to back-scattering. This effect is dependent upon the structure surrounding the detector and has not been included in the response function.

A.2.2 Germanium Detector

The germanium x-ray detector is a solid-state detector: a high voltage applied across a slab of high purity germanium produces a region depleted of conducting electron-hole pairs; a photon entering the depletion region liberates electron-hole pairs into the conduction band, producing current which is integrated, and the resulting pulse is sent to a pulse-height analysis system. The photo-excitation cross-section is much larger than that for Compton scattering for the lower photon energies measured with the Ge detector

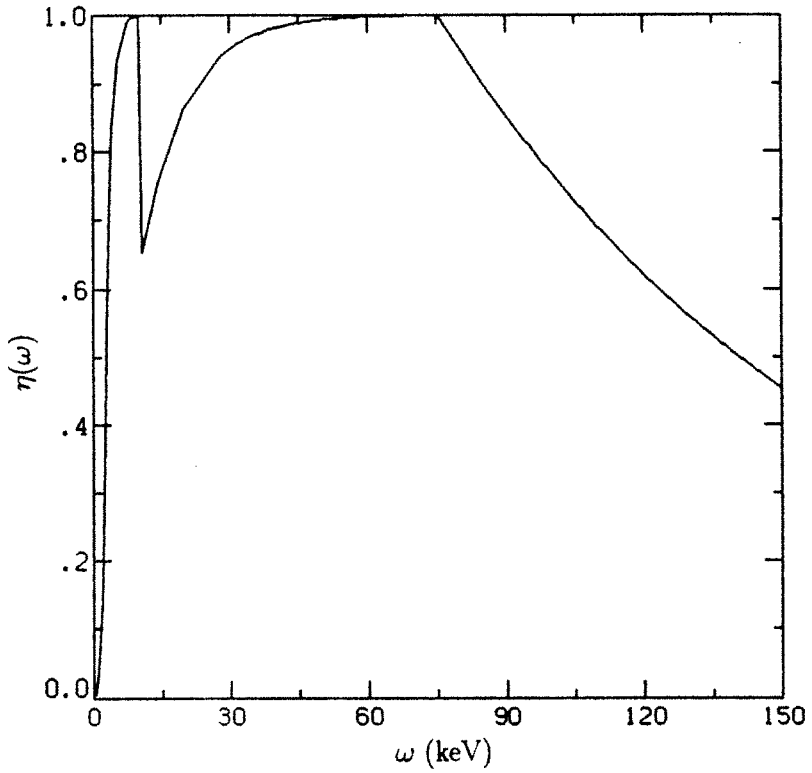

Figure A.6: Photo-peak total efficiency and Be window attenuation for the Ge detector. The depletion depth is assumed to be 10 mm and there is 0.038" of Be window (0.015" vacuum window + 0.023" detector entrance window). The feature at 10.36 keV is the Ge K_α edge.

$(1 < \omega < 150$ keV), so the detector response is simpler than that of the NaI(Tl) detector. I have used an analytic fit to the overall efficiency $\eta(\omega)$ for Ge provided by Frederick Seguin of American Science and Technology, Inc., who loaned us the detector (ω in keV):

$$\begin{aligned} \eta(\omega) &= 0.026\omega^3 && (0 < \omega < 2.5) \\ &= 1 - 4.4e^{-\omega/1.25} && (2.5 < \omega < 10.36) \\ &= 1 - e^{-\omega/10} && (10.36 < \omega < 75) \\ &= e^{-(\omega-75)/95} && (75 < \omega < 300). \end{aligned} \tag{A.14}$$

This fit is plotted in Figure A.6. Since the Ge detector is of fairly high resolution, I have not employed a photo-peak response calculation as for the NaI(Tl) detector, but have simply multiplied the pure spectra by the efficiency to obtain the detector-modified theoretical spectra.

A.2.3 Si(Li) Detector

The Si(Li) detector is a solid-state detector similar to the Ge detector. The actual device differs slightly in that an optical pulse is used to reset the semiconductor after a certain amount of charge has been liberated. These reset pulses appear as large spikes in the output, but may be discriminated against by means of a logic pulse supplied by the preamp. Having high resolution, the Si(Li) detector response is dominated by the absorption efficiency. For the range of energies studied with this detector, 1-12 keV, the response is flat and only the attenuation of the thin (90 $\mu g/cm^2$) Al window was used. It was found that the detector response had an anomolously sharp degredation in response below 1 keV; this is still not understood, but may be due to contaminants on the surface of the detector.

A.3 X-Ray Spectrum Comparison Method

The method of fitting x-ray spectra is simple: the detector-modified spectrum for a chosen distribution function is compared to the raw data using the χ^2 goodness-of-fit criterion, where the data points (N counts per channel) are weighted by the expected standard deviation $\sqrt{N}$. The count rate is usually sufficient for a statistically significant steady-state temperature to be determined for a single shot if 10 spectra are summed (usually the spectra in the afterglow). For time-resolved analysis, up to 20 identical shots are summed.

Figure A.7 summarizes this, displaying a pure theoretical spectrum and its detector-modified counterpart, and an experimental intensity distribution formed by summing 20 shots.

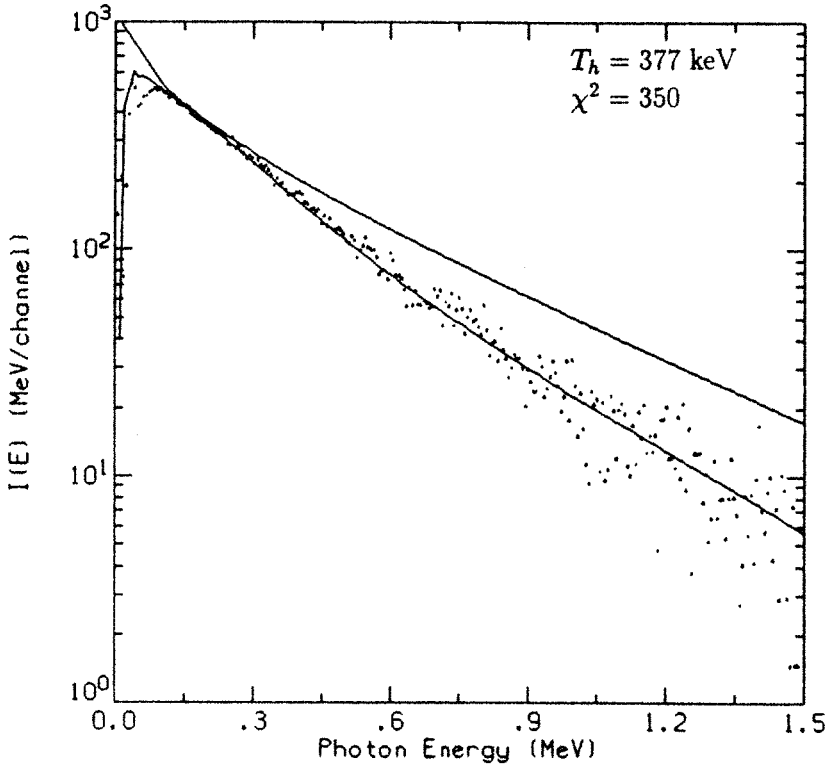

Figure A.7: An experimental intensity spectrum and theoretical spectra for a Maxwellian electron distribution with $T = 377$ keV.

Appendix B

Scintillator Probe Response

Most of the scintillator probe data reported here has been taken with a probe which has an array of five cylindrical NE102 plastic scintillators (4 mm diameter, 8 mm length) optically linked to fiber optic guides which are in turn attached to 3/8" photo-multiplier tubes (PMTs). The PMT currents are measured either with logarithmic current-to-voltage converters (Analog Devices 759P) or a linear current-to-voltage converter using an op amp (Analog Devices 50J) if fast (10 MHz) response is desired. The openings to the scintillators have entrance windows made of foils of various thicknesses and lengths. The response of the probes is a combination of: 1) the PMT gain at the wavelength of the scintillator emission (420 nm) and the given high voltage bias, 2) the electron energy-to-light conversion efficiency of the scintillator, 3) the transmission of the entrance foil, and 4) the optical coupling between the scintillator and fiber optic and between the fiber optic and PMT.

B.1 Photomultiplier Gain

The PMTs are designed for scintillation counting and have the optimum response at the scintillator wavelength; a typical current gain is 10^6 at a bias voltage of 1250 V, with a photocathode quantum efficiency of 25% (Hamamatsu tube #R1635). They are relatively calibrated *in situ* by rotating the probe away from the plasma and exposing it to the uniform background of x-rays emitted from the endwall. The resulting signals are identical in shape, and their ratio gives the relative PMT gain of each channel.

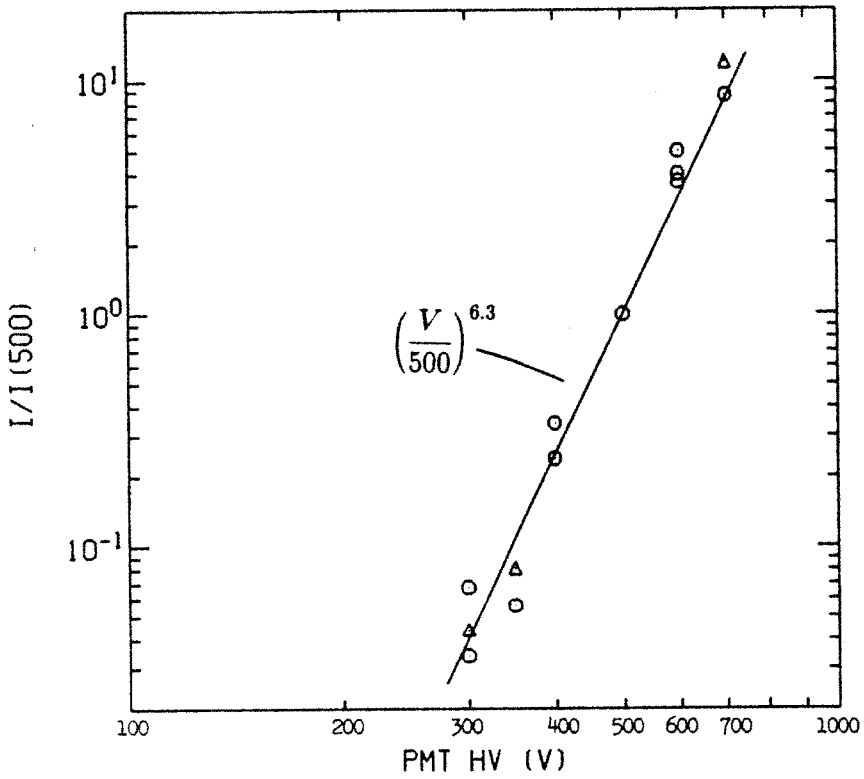

Figure B.1: Photomultiplier tube current vs. bias voltage, normalized to current at 500 V. The best fit power law curve is given by $I/I_{500} = (V/500)^{6.3}$.

The gain of the PMT is strongly dependent on bias voltage, and this is taken advantage of in the experiments: since the endloss power varies by over an order of magnitude for the range of plasma parameters studied, the PMT bias is often adjusted so that the lowest energy (largest current) channel in the array has a peak current of 10–50 μA, which allows for fast logarithmic amp response while keeping the PMT current well below the saturation level. The calibration and experimental data is always scaled back to the standard PMT bias of 500 V. Fig. B.1 displays the PMT current normalized to the current at a bias of 500 V, obtained by running identical plasma shots for different bias voltages. The data corresponds to the tube in the lowest energy channel, which is the one used for most of the data presented in this dissertation. The data is fit with a power law relation

$$\frac{I}{I_{500}} = \left(\frac{V}{500}\right)^{6.3} \pm 40\%, \tag{B.1}$$

where the error estimate corresponds to the mean deviation of the data from the curve.

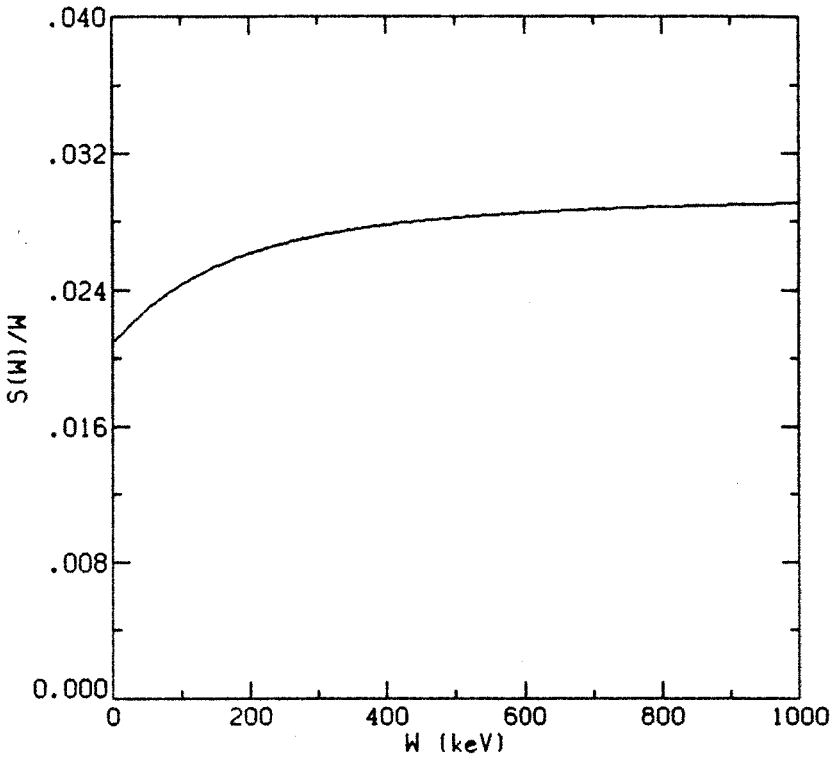

Figure B.2: NE102 scintillator light efficiency.

B.2 Scintillator Light Response

The light conversion efficiency of NE102 plastic scintillator is a constant for electron energies above 125 keV (Brannen and Olde, 1962), and has the value of 65% of the light output of anthracene (Nuclear Enterprises, 1980), or 3.0%; that is, 3% of an electron's energy is converted into light in the scintillator. Electrons with incident energies below 125 keV produce less light because they can backscatter away from the scintillator; measurements made with electron sources which are surrounded by scintillator show that the response is constant down to energies of 10 keV for that geometry. I have made a fit to the results of Brannen and Olde which gives the light response of NE102 for all electron energies:

$$S(W) = 0.03(W - 29.6 + 29.6e^{-W/97}), \tag{B.2}$$

where W is the electron energy in keV. The light efficiency $S(W)/W$ is plotted in Fig. B.2.

B.3 Foil Transmission

Kobetich and Katz (1969) have presented an empirical algorithm for calculating the energy deposited by electrons as they slow down in materials which matches experimental data very well. The algorithm is based on two empirical formulae: one for the characteristic range r in the material to which electrons can penetrate, and one for the fraction $\eta(t)$ which are transmitted beyond a thickness t, given by

$$\eta = \exp\{-(qt/r)^p\}, \tag{B.3}$$

$$r = Aw[1 - B/(1 + Cw)], \tag{B.4}$$

where

$$\begin{aligned} p &= 1.8(\log_{10} Z)^{-1} + 0.31, \\ q &= 0.0059Z^{0.98} + 1.1, \\ A &= 0.81Z^{-0.38} + 0.18 \text{ MeV g/cm}^2, \\ B &= 0.21Z^{-0.055} + 0.78, \\ C &= 1.1Z^{0.29} + 0.21 \text{ MeV}^{-1}. \end{aligned}$$

Z is the atomic number of the material (for mixed materials, Z is the average value weighted over the mass fractions), and w is the incident electron energy. (Note that foil thicknesses are given in the units of g/cm^2, which eliminates the appearance of the mass density.) The residual energy $W(r,t)$ that an electron has after penetrating the thickness t is approximated by the energy required for it to travel the residual distance $r - t$, that is, $W(r,t) = w(r - t)$. The energy remaining in a beam after traversing a thickness t is then ηW, and the stopping power $E(t)$ (energy deposited per unit length) is given by the formulae

$$t/r < 0.9: \quad E(t) = d(\eta W)/dt, \tag{B.5}$$

$$t/r > 0.9: \quad E(t) = E(0.9r)\{\eta(t)/\eta(0.9r)\}^{4/p}. \tag{B.6}$$

The second (thick-target) formula is designed to take account of the electrons which straggle beyond the range r, and provides improved agreement with experiment.

For the purpose of determining the effect of entrance foils on incoming electrons, the quantities η and W are needed; since the scintillator response depends on electron energy W, these are needed separately, rather than in the form of the total energy ηW. For $t/r < 0.9$ I have used the formula $W(t) = w(r - t)$; for $t/r > 0.9$ I have integrated Eq. B.6 in the region $0.9r < t' < t$ to get the additional loss in total energy $\Delta(\eta W)$, and then have found W using

$$W(t) = [\eta(0.9r)W(0.9r) + \Delta(\eta W)]/\eta(t).$$

In practice, the channels with very thick foils have a larger sensitivity to target x-rays, produced by the electrons impinging upon the foils, than to the small number of electrons that make it through. I have therefore focused on the three thinnest foil channels in the data analysis, which have range energies below 200 keV.

B.4 Overall Response

The overall efficiency of the entire probe has been determined with a 30 kV electron beam in a test stand. The calibration was performed by Paul Stek. Since all except the thinnest foil used in the multi-channel probe are opaque to 30 keV electrons, the test stand was only used to calibrate a probe with a single layer of aluminized mylar foil without TiO_2 reflective paint on the front surface of the scintillator, and one with only reflective paint on the front surface. The probes in the experiment all have reflective paint on the front surfaces to provide extra light shielding and ruggedness.

Fig. B.3 shows the result of the calibration, expressed in PMT current per unit incident power density as a function of beam energy (the power density is found by multiplying the beam voltage by the current density measured with a Faraday cup). In addition, calculated response curves for a $Z = 6.1$ foil, corresponding to mylar, and a $Z = 38$ foil, corresponding to TiO_2, are shown. The fit to the $Z = 6.1$ curve is excellent,

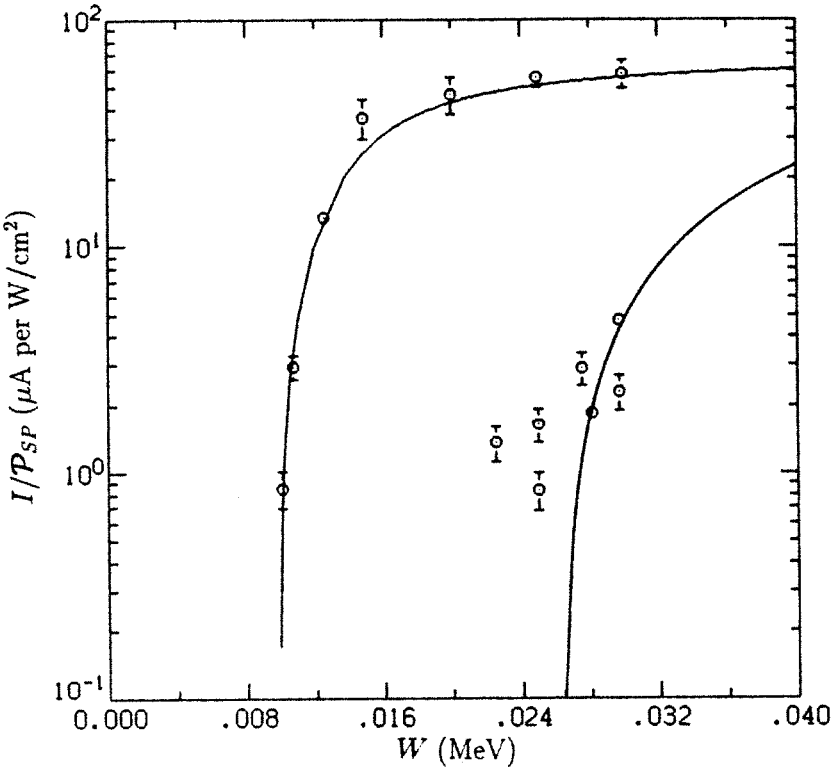

Figure B.3: Scintillator probe response as a function of electron beam energy in the calibration facility. The curves were calculated using the foil response algorithm.

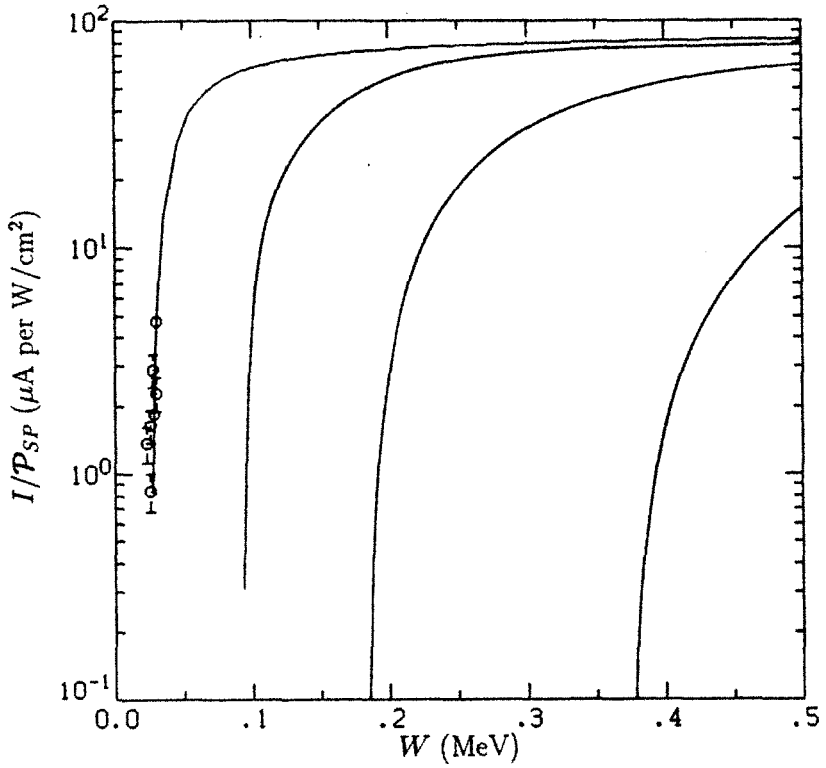

Figure B.4: The calculated response for four of the foils in the five-channel probe used in the experiment, using the calibrated response of the test probe at a 500 V bias.

and the best-fit thickness of 2.85×10^{-4} g/cm^2 is in agreement with the value for the thickness supplied by the manufacturer (Kimberly-Clarke). This indicates that the dead layer of the scintillator is quite thin (less than 5×10^{-5} g/cm^2). This data was used to determine the overall response of the probe. The fit for the reflective paint case, with a best-fit thickness of 1.35×10^{-3} g/cm^2, is poor, which probably reflects that the paint layer is not uniform. The data is bracketed by curves with thicknesses of 1.0×10^{-3} and 1.5×10^{-3} g/cm^2, and a 50% variation of paint thickness is completely reasonable. A weight measurement indicated an average thickness of approximately 1.9×10^{-3} g/cm^2, in reasonable agreement with the fitted value considering the crudeness of the weighing technique. The uncertainty in the paint thickness has no effect on the response at energies above 100 keV.

Fig. B.4 shows the calculated response of the test PMT for four of the foils used in the multi-channel probe. The lowest energy channel has only paint; the other channels

have aluminum foils. The range energies for these channels are 27, 95, 200, and 405 keV. The signal from the fifth channel, with a range energy of 660 keV, was dominated by x-ray response and was not used.

The response of the five-channel probe is found by multiplying the test probe response by the ratio of the entrance areas of the five-channel probe and the test probe and the ratio of the PMT gains. The result, the conversion from PMT current to endloss power density, ranges from 8.4 mW/cm^2 per μA at 50 keV to 5.2 mW/cm^2 per μA at 500 keV for the lowest energy channel. Since half of the decay power detected by the lowest energy channel is between 100 and 200 keV, I have chosen to use the response at 150 keV, multiplied by a factor of 1.1 to account for the additional power below the 27 keV range energy, estimated from extrapolation of the decay spectrum shown in Fig. 4.9. The resulting conversion is 7.2 ± 2.8 mW/cm^2 per μA at a PMT bias of 500 V. The estimated error of 40% is mostly due to the uncertainty in the PMT gain conversion.

Although not needed to interpret the experimental data, the optical efficiency of the probe has been computed by comparing the calibration data with the response of a 3/8" scintillator placed directly on a PMT and exposed to a Cl^{36} source, which emits 712 keV electrons. The overall optical transmission of the probe is about 2%, not unreasonable considering the 30% transmission of the fiber optic and the rather poor coupling of the scintillator to the fiber optic which was necessitated by vacuum requirements.

References

Antonsen TM and Manheimer WM (1978) Phys. Fluids **21**, 2295.

Batchelor DB, Carter MD, Chen GL, and Hedrick CL (1987) Phys. Rev. Lett. **58**, 2664.

Berger MJ and Seltzer SM (1972) Nucl. Inst. and Meth. **104**, 317.

Bernstein IB, and Baxter DC (1981) Phys. Fluids **24**, 108.

Boehmer H, Goede H, and Talmadge S (1985) Phys. Fluids **28**, 3099.

Brannen E and Olde GL (1962) Rad. Res. **16**, 1.

Chen L, Vaclavik J, and Hammett GW (1987) Princeton Plasma Physics Lab report PPPL-2441.

Chirikov BV (1979) Sov. J. Plasma Phys. **4**, 289.

Cohen RH (1979) Nucl. Fusion 19, 1579.

Cohen RH, Rowlands G, Foote JH (1978a) Phys. Fluids **21**, 627.

Cohen RH, Rensink ME, Cutler TA, Mirin AA (1978b) Nucl. Fusion **18**, 1229.

Cohen BI, Cohen RH, and Rognlien TD (1983) Phys. Fluids **26**, 808.

England A and Haste G (1973) Oak Ridge National Lab report ORNL-TM-4103.

Fioratti MP and Piermattei SR (1971) Nucl. Inst. and Meth. **96**, 605.

Fredian TW and Stillerman JA (1986) Rev. Sci. Inst. **57**, 1907.

Garner RC (1986) Ph.D. dissertation, Dept. of Physics, MIT, reprinted as MIT Plasma Fusion Center report PFC/RR-86-23.

Garner RC, Hokin SA, Mauel ME, Post RS, and Smatlak DL (1987) to be published in Phys. Rev. Lett.

Heitler W (1954) *The Quantum Theory of Radiation* (Third Edition, Oxford University Press, London).

Hubbell JH (1969) National Bureau of Standards report NSRDS-NBS 29.

Jaeger F, Lichtenberg AJ, and Lieberman MA (1972) Plasma Physics **14**, 1073.

Kobetich EJ and Katz R (1969) Nucl. Inst. and Meth. **71**, 226.

Lichtenberg AJ and Melin G (1973) Phys. Fluids **16**, 1660.

Lichtenberg AJ, Lieberman MA, Howard JE, and Cohen RH (1986) Phys. Fluids **29**, 1061.

Lieberman MA and Lichtenberg AJ (1973) Plasma Physics **15**, 125.

Lieberman MA and Lichtenberg AJ (1983) *Regular and Stochastic Motion* (Springer-Verlag, New York).

Matsuda Y and Stewart JJ (1986) J. Comp. Phys. **66**, 197.

Mauel ME (1982) Ph.D. dissertation, Dept. of Eectrical Engineering, MIT, reprinted as MIT Plasma Fusion Center report PFC/RR-82-29.

Mauel ME (1984) Phys. Fluids **27**, 2899.

Nuclear Enterprises (1980) Brochure No. 126P.

Rognlien TD (1983a) Phys. Fluids **26**, 1545.

Rognlien TD (1983b) Nucl. Fusion **23**, 163.

Sackett SJ (1978) Lawrence Livermore National Lab report UCRL-52402.

Smatlak DL, Chen X, Garner RC, Goodman DL, Hokin SA, Irby JH, Lane BG, Liu DK, Post RS, Smith DK, and Trulsen J (1986) MIT Plasma Fusion Center report PFC/RR-86-15.

Smatlak DL, Chen X, Lane BG, Hokin SA, and Post RS (1987) Phys. Rev. Lett. **58**, 1853.

Smith GR, Byers JA, and LoDestro LL (1980) Phys. Fluids **23**, 278.

Swanson SM (1967) Phys. Rev. **154**, 1601.

Turner WC, Powers EJ, and Simonen TC (1977) Phys. Rev. Lett. **39**, 1087.

Uckan NA (1982) Phys. Fluids **25**, 2381.

Wyeth NC, Lichtenberg AJ, and Lieberman MA (1975) Plasma Physics **17**, 679.